

Electronic Theses and Dissertations, 2004-2019

2010

Epitaxial Growth, Characterization And Application Of Novel Wide Bandgap Oxide Semiconductors

Jeremy Mares
University of Central Florida

 Part of the [Electromagnetics and Photonics Commons](#), and the [Optics Commons](#)
Find similar works at: <https://stars.library.ucf.edu/etd>
University of Central Florida Libraries <http://library.ucf.edu>

This Doctoral Dissertation (Open Access) is brought to you for free and open access by STARS. It has been accepted for inclusion in Electronic Theses and Dissertations, 2004-2019 by an authorized administrator of STARS. For more information, please contact STARS@ucf.edu.

STARS Citation

Mares, Jeremy, "Epitaxial Growth, Characterization And Application Of Novel Wide Bandgap Oxide Semiconductors" (2010). *Electronic Theses and Dissertations, 2004-2019*. 4218.
<https://stars.library.ucf.edu/etd/4218>

EPITAXIAL GROWTH, CHARACTERIZATION AND APPLICATION OF NOVEL WIDE
BANDGAP OXIDE SEMICONDUCTORS

by

JEREMY WEST MARES
B.S. University of Central Florida, 2003

A dissertation submitted in partial fulfillment of the requirements
for the degree of Doctor of Philosophy
in the College of Optics / CREOL&FPCE
at the University of Central Florida
Orlando, Florida

Spring Term
2010

Major Professor: Winston V. Schoenfeld

© Jeremy W. Mares

ABSTRACT

In this work, a body of knowledge is presented which pertains to the growth, characterization and exploitation of high quality, novel II-IV oxide epitaxial films and structures grown by plasma-assisted molecular beam epitaxy. The two compounds of primary interest within this research are the ternary films $\text{Ni}_x\text{Mg}_{1-x}\text{O}$ and $\text{Zn}_x\text{Mg}_{1-x}\text{O}$ and the investigation focuses predominantly on the realization, assessment and implementation of these two oxides as optoelectronic materials. The functioning hypothesis for this largely experimental effort has been that these cubic ternary oxides can be exploited - and possibly even juxtaposed - to realize novel wide band gap optoelectronic technologies. The results of the research conducted presented herein overwhelmingly support this hypothesis in that they confirm the possibility to grow these films with sufficient quality by this technique, as conjectured.

$\text{Ni}_x\text{Mg}_{1-x}\text{O}$ films with varying Nickel concentrations ranging from $x = 0$ to $x = 1$ have been grown on lattice matched MgO substrates (lattice mismatch $\varepsilon < 0.01$) and characterized structurally, morphologically, optically and electrically. Similarly, cubic $\text{Zn}_x\text{Mg}_{1-x}\text{O}$ films with Zinc concentrations ranging from $x = 0$ to $x \approx 0.53$, as limited by phase segregation, have also been grown and characterized. Photoconductive devices have been designed and fabricated from these films and characterized. Successfully engineered films in both categories exhibit the desired deep ultraviolet photoresponse and therefore verify the hypothesis.

While the culminating work of interest here focuses on the two compounds discussed above, the investigation has also involved the characterization or exploitation of related films including hexagonal phase $\text{Zn}_x\text{Mg}_{1-x}\text{O}$, ZnO, $\text{Cd}_x\text{Zn}_{1-x}\text{O}$ and hybrid structures based on these compounds used in conjunction with GaN. These works were critical precursors to the growth of

cubic oxides, however, and are closely relevant. Viewed in its entirety, this document can therefore be considered a multifaceted interrogation of several novel oxide compounds and structures, both cubic and wurtzite in structure. The conclusions of the research can be stated succinctly as a quantifiably successful effort to validate the use of these compounds and structures for wide bandgap optoelectronic technologies.

To my father, who sparked my love of science with stories about space, time and light...
To my grandfather, who impressed upon me the essential tools of science and engineering...
To my mother, who gave me insight beyond science...
And to my siblings and friends, who continually give me more than science can offer.

ACKNOWLEDGMENTS

The research accomplishments presented herein would have never been possible without the significant contributions and enduring support of several individuals. To start, Professor Winston Schoenfeld has provided guidance and support at every step in the process, and has been not only an advisor in my academic career, but also a mentor in my scientific development. Fellow students Matthew Falanga and Casey Boutwell have contributed countless hours of work – many of which were arduous and relatively thankless – alongside the author to help advance the research presented here. Sabine Freisem, while perhaps not entirely cognizant of the help she provided, has been a tremendous source of knowledge and encouragement with regards to crystal growth and the molecular beam epitaxy system. The author would also like to acknowledge his PhD committee members who have all been very helpful and whose input has been critically formative in this endeavor.

TABLE OF CONTENTS

LIST OF FIGURES	ix
LIST OF TABLES	xiv
LIST OF ABBREVIATIONS.....	xv
1. INTRODUCTION: A NOVEL METAL-II-OXIDE FAMILY	1
2. EXPERIMENTAL METHODS.....	8
Plasma Assisted Molecular Beam Epitaxy	8
System.....	8
Film Characterization Methods.....	12
In Situ.....	12
Ex Situ	14
Rutherford Backscattering.....	14
Spectrophotometry	14
Atomic Force Microscopy.....	15
X-Ray Diffraction	16
Device Design & Fabrication Techniques	17
Device Characterization Techniques.....	22
3. RESULTS	28
MgO	30
MgO Heteroepitaxy	30
MgO Homoepitaxy	34
Growth Dynamics	37
Mg Pressure Effects	37
Effect of Mg Aperture	38
Ni _x Mg _{1-x} O	40
NiO Film Growth and Characterization	41
Cation-Rich Growth	42
NiO.....	43
NiMgO	45
Oxygen-Rich Growth	48
NiO & NiMgO	49
NiO & NiMgO Device Fabrication and Testing.....	58
NiO Initial Devices.....	59
NiMgO Devices.....	63
ZnO and ZnMgO.....	73

ZnO Film Growth & Characterization.....	73
ZnMgO Film Growth and Characterization	76
ZnMgO DBR.....	90
ZnMgO Device Characterization.....	92
CdZnO.....	95
Compositional and Morphological Characterization.....	95
Optical Characterization	100
Complex Refractive Indices	103
Hybrid and Fully-Oxide Devices.....	111
Hybrid.....	112
Fully II-Oxide QW LED	118
4. CONCLUSIONS.....	123
5. REFERENCES	124

LIST OF FIGURES

Figure 1. Number of publications by year for each of the oxide binaries ZnO, MgO and NiO. Source is ISI indexing.	3
Figure 2. (Top) Diagram of the MBE system used for oxide thin film growth shown with (bottom) a photograph of the system.....	9
Figure 3. (Top) Diagram of the oxide molecular beam epitaxy chamber shown with (bottom) a photograph of the chamber.....	10
Figure 4. (a) The Oxygen plasma injector during operation and (b) a 1 cm ² MgO substrate on a Molybdenum substrate holder.	11
Figure 5. Screen shot of the software used for photomask design, L-Edit.	18
Figure 6. Two MSM devices of different geometry. That on the left is a small-area detector optimized for response speed while that on the right large area and is designed for sensitivity.....	19
Figure 7. Structural diagram of the hybrid GaN-ZnO LEDs (left) and fully-ZnO LEDs (right).	20
Figure 8. A Kulicke and Soffa 4525AD manual wire bonder.	21
Figure 9. The Signatone 1160 probe station (left) used for electronic characterization of devices shown with a Keithley 2400 source-meter (right).....	23
Figure 10. Image of a ZnMgO MSM device under electrical testing for IV characteristics.	23
Figure 11. Diagram of experimental setup for characterization of device spectral response.	25
Figure 12. (top) An early setup for detector spectral response including an aluminum mirror just prior to the device which is mounted on the table top facing up. (bottom) A more recent detector spectral response in which the device is mounted laterally on a custom stage equipped with probe positioners.	26
Figure 13. Images of a NiMgO MSM device under spectral testing, illuminated here by radiation with wavelengths 420 nm, 535 nm and 635 nm from left to right.	27
Figure 14. A RHEED image of a Si(100) surface after cleaning and degassing.	31
Figure 16. Growth rates for MgO on Si with two substrate temperatures, 200 °C and 500 °C... ..	32
Figure 15. Laser Interferometry curve for MgO on Si(111) with a substrate temperature of 200 °C. The change in oscillation frequency is due to increasing Mg K-Cell temperature	32

Figure 17. (a) Spectral Reflectance and (b) Atomic Force Microscopy of MgO thin film grown on Si. The film orientation is evidenced by the triangular-based structures and is inherited from the (111) oriented Silicon substrate.....	34
Figure 18. AFM of a MgO homoepitaxial film grown at the stoichiometric point in the Mg pressure curve. Note the (111)-like orientation resulting from fast growth rates despite the (100) substrate orientation.....	35
Figure 19. AFM (2D and 3D) of a MgO film grown in oxygen-rich conditions. The slower growth promotes the proper (100) orientation as exhibited by square-based pyramidal formations.....	36
Figure 20. RHEED images of MgO film growth (a) prior to growth, (b) after 30 minutes of growth and (c) after one hour. Also, (d) AFM showing the high quality of the MgO film surface verifying the RHEED indications. Roughness of the film is less than 7 Å.	37
Figure 21. Growth chamber pressure at a function of Mg cell temperature. The two curves shown are for two different sized apertures, 3mm and 9 mm.	39
Figure 22. (a) AFM of a NiO thin film grown on Si (100) highlighting the cubic shaped (100) NiO crystal facets and (b) Spectral reflectance for NiO heteroepitaxial film	44
Figure 23. (a) AFM and (b) Spectral transmittance for a ~1 μm thick NiO film on MgO	45
Figure 24. Typical transmittance curves for Ni _x Mg _{1-x} O thin films grown under cation-rich conditions	46
Figure 25. AFM scan of a NiO film grown in oxygen rich conditions with RMS roughness of 0.7 Å.	51
Figure 26. Six of the eight NiMgO films grown.....	52
Figure 27. RHEED and AFM for two NiMgO films (b, c) shown with those of a virgin substrate for comparison.....	53
Figure 28. XRD results for the NiMgO thin films shown for the ranges 35° < 2θ < 45° (a) and 42° < 2θ < 44°	55
Figure 29. (a) RBS, (b) Absorption plotted as Tauc curves and (c) extracted bandgap versus Nickel concentration for all eight NiMgO films.	56

Figure 30. MSM Devices fabricated on NiO (on MgO).....	60
Figure 31. NiO MSM devices under (a) 325 nm illumination and (b) 635 nm illumination. Note that the blue appearance in (a) is not the laser light color itself (which is UV) but rather an artifact of luminescence from one of the optics used to redirect the laser light.	61
Figure 32. IV curves showing the photoresponse of a NiO-on-MgO MSM device to 325 and 635 nm light as compared to the device dark IV. The difference between the dark current and that under 635 nm illumination is almost indistinguishable on this scale.	62
Figure 33. IV curves for a NiO MSM device on Si. While the differential responsivity is less substantial, these devices do exhibit strongly rectifying behavior.	63
Figure 34. MSM devices fabricated from NiMgO thin film by electron beam lithography.....	65
Figure 35. (left) Four sequentially acquired pairs of dark and light IV curves shown with the converging value of the device current at 10 V with increasing trial number (right). .	67
Figure 36. The temporal photoresponse two NiMgO films grown with identical Ni:O flux ratios. One film (top) was grown at a substrate temperature of 100 °C while the other (bottom) was grown at 500 °C.	69
Figure 37. The temporal response of a high quality NiMgO film exposed to 290 nm light for 2.5 seconds.	70
Figure 38. Spectrotemporal response of NiMgO MSM device.	71
Figure 39. Spectral response of two similar NiMgO films, grown only with different Mg fluxes. The shift in device response edge demonstrates the tunability of the films' bandgap.	72
Figure 40. a) Reflectance oscillations from a ZnO epitaxial film growth. b) Growth rates derived from the growth in a) and one other growth session.	74
Figure 41. (Left top) Spectral reflection and (left bottom) photoluminescence of ZnO on c-plane Al ₂ O ₃ . (Right) AFM scan of ZnO thin film exhibiting 3.16 nm RMS roughness.	75
Figure 42. Rutherford Backscattering spectra for the six films grown. The highest energy peak indicates the Zn concentration which increases from x = 0 to x = 0.65, from bottom to top.	78
Figure 43. X-ray diffraction spectra of the Zn _x Mg _{1-x} O thin films in the angular range 30° < 2θ < 42.5° (left pane) and 41.5° < 2θ < 44.5° (right pane).....	79

Figure 44. ZnMgO film lattice constants, as derived from the cubic (002). Values are found to be in good agreement with those reported in literature.	80
Figure 45. (a) $5 \times 5 \mu\text{m}^2$ AFM image of the $x = 0.33$ film. (b) RHEED image of the $x = 0.33$ sample (c) $5 \times 5 \mu\text{m}^2$ AFM image of the $x = 0.65$ film	82
Figure 46. RMS roughness of the six films, as measured over a $2 \times 2 \mu\text{m}^2$ region.	83
Figure 47. Transmission of the ZnMgO films, as determined by UV-VIS spectrophotometry. .	84
Figure 48. Optical absorption of the ZnMgO films, as derived from transmission measurements.	85
Figure 49. Bandgap values of the five ternary films plotted versus Zn concentration, x , shown with the accepted bandgap value of binary MgO and various published values from other works.	87
Figure 50. Electrical conductivities of the ZnMgO films and the MgO homoepitaxial one.	89
Figure 51. RBS spectra of a 5-period ZnMgO distributed Bragg reflector	90
Figure 52. Transmittance (left) and approximate reflectance (right) of the ZnMgO/MgO DBR.	91
Figure 53. X-ray diffraction measurement of a $\text{Zn}_{0.4}\text{Mg}_{0.6}\text{O}$ thin film exhibiting strictly cubic structure, as indicated by the absence of any hexagonal peaks.	93
Figure 54. Spectrotemporal response of the ZnMgO film showing deep UV spectral response with a cutoff wavelength of approximately 260 nm.	94
Figure 55. Photoresponse of the $\text{Zn}_{0.4}\text{Mg}_{0.6}\text{O}$ thin film plotted with the film's transmission measurement.	94
Figure 56. Rutherford Backscattering energy spectra of three $\text{Cd}_x\text{Zn}_{1-x}\text{O}$ samples	97
Figure 57. SIMS compositional analysis of a 36% cadmium sample.	98
Figure 58. AFM scans of GaN nucleation layer (a), and 2, 10 and 30% cadmium samples (b-d), shown with roughness versus cadmium concentration for 7 samples (e).	99
Figure 59. Photoluminescence and absorption for 2, 16 and 30% cadmium concentration samples.	102
Figure 60. Band gap energy and PL FWHM as a function of cadmium concentration.	103
Figure 61. Variable assignments for spectrophotometric measurement of thin films.	105

Figure 62. The refractive indices of $Cd_xZn_{1-x}O$ thin films for six different Cd percentages, as fit to the Sellmeier dispersion relation.	109
Figure 63. The real (left) and imaginary (right) refractive indices for six samples of $Cd_xZn_{1-x}O$ thin films.....	109
Figure 64. (Left) Hybrid ZnO-based single quantum well LED and (right) fully ZnO-based multiple quantum well LED.....	112
Figure 65. The etch depth as a function of time for the CdZnO/GaN hybrid LED. Note that the nonlinearity in the etch rate is due to saturation of the etchant volume used.....	113
Figure 66. (Top) AFM image of a mesa corner. Sidewalls observed are due to lateral etching of ZnO by HCl/H ₂ O (Bottom) AFM cross-section revealing sidewall with a slope of $\Delta z/\Delta y = 1/2$	114
Figure 67. An array of fabricated CdZnO/GaN LEDs.....	115
Figure 68. IV curves shown for a device prior to annealing, after 2 minutes of annealing at 450 °C and after 2 additional minutes of annealing at 550 °C.	116
Figure 69. Light output versus current for a typical CdZnO/GaN LED.....	117
Figure 70. A functioning CdZnO/GaN LED emitting blue light.....	118
Figure 71. AFM of a wet-etched ZnO LED mesa.	119
Figure 72. Fabricated fully ZnO MQW LEDs. The left image clearly illustrates the results of the variable-time etch rate procedure. The right image was taken of the same devices, but focused on the back surface of the substrate through the transparent contact layers which cover the mesas.....	121
Figure 73. IV characteristics of fully ZnO LEDs with and without transparent contacts.	121
Figure 74. An operating fully ZnO LED without transparent contact (left, I=65 mA) and an analogous device with a 15 nm transparent contact (right, I=35 mA).	122

LIST OF TABLES

Table 1. Growth parameters used for initial cation-rich NiMgO films growths.	46
Table 2. Coefficients for dispersion model fits for $\text{Cd}_x\text{Zn}_{1-x}\text{O}$ samples.	110

LIST OF ABBREVIATIONS

AFM	Atomic Force Microscopy
DBR	Distributed Bragg Reflector
DUV	deep ultraviolet
HeCd	Helium Cadmium, the gain medium of a UV laser used
IV	Current(I)-Voltage(V)
LED	Light Emitting Diode
LI	Optical Power (L) versus Current(I)
MOCVD	Metal-Organic Chemical Vapor Deposition
MSM	Metal-Semiconductor-Metal
NiMgO	Nickel Magnesium Oxide, Equivalent to $\text{Ni}_x\text{Mg}_{1-x}\text{O}$
PLD	Pulsed Laser Deposition
QW	Quantum Well
RBS	Rutherford Backscattering
Re-RAM	Rewritable Random Access Memory
RHEED	Reflected High-Energy Electron Diffraction
RMS	Root-mean Square
RPM	Rotations Per Minute
RUMP	RBS Universal Manipulation Program
SIMS	Secondary Ion Mass Spectroscopy
TCO	Transparent Conducting Oxide
UV	ultraviolet
VI	Virtual Instrument, a LabView software terminology
XRD	X-Ray Diffraction
ZnMgO	Zinc Magnesium Oxide, Equivalent to $\text{Zn}_x\text{Mg}_{1-x}\text{O}$

1. INTRODUCTION: A NOVEL METAL-II-OXIDE FAMILY

The materials of primary interest within the scope of this work—MgO, NiO, ZnO and two of their ternary combinations -- comprise a rather diverse family of compounds. Apart from the obvious commonality of all being oxides, it is not immediately evident how each of these semiconductors is relevant to the others. In fact, among the three binary compounds, only one is even considered a semiconductor in most discussions. MgO is normally classified solidly as an insulator ($E_g = 7.8$ eV) while NiO ($E_g \approx 4$ eV) has classically been categorized as a so-called Mott-Hubbard insulator. However, it is the author's intent to demonstrate that these compounds comprise a compatible and complimentary family of wide band gap optoelectronic materials. The functioning hypothesis for this largely experimental effort has been that, with improved growth techniques and advances in understanding of electronic properties, these oxides *can* be incorporated and juxtaposed to realize novel wide band gap optoelectronic technologies.

Each of the binary compounds has been studied extensively in various fields of pure and applied science for applications that are specific to that compound. They have been used extensively in numerous industrial processes, consumer products and scientific apparatuses. However, prior to recent decades they were of limited interest for their semiconductor properties. This is due largely to two simple factors. First, because wide band gap semiconductor technologies have lagged behind narrower gap ones in general, emphasis in the research community on such materials for devices had not yet burgeoned. It was not until successes in the GaN system became touted (and to a lesser extent ZnSe, SiC and others), that the appetite for wide band gap technologies had been whetted. Second and more decisive perhaps, is the fact

that several key technologies which have advanced oxide film growth significantly had not yet matured. Thus, pristine quality single crystal thin films and structures could not be grown.

Oxide film growth has benefitted from many of the same technologies that can be credited with advancing other materials such as GaN. Modern sophisticated film growth techniques including pulsed laser deposition (PLD), metalorganic chemical vapor deposition (MOCVD) and molecular beam epitaxy (MBE) have all been applied to the oxide films of interest with a high degree of success [1-10]. Many of the initial oxide investigations with these methods occurred in the late nineteen-eighties and early nineteen-nineties spurred, in many cases, by the success of these techniques with more popular oxide films of the time, particularly high-temperature superconductors such as $\text{YBa}_2\text{Cu}_3\text{O}_{7-\delta}$ [11, 12]. With continued refinement of the growth methods and parameters for the oxide films, they have become of greater interest as wide band gap materials.

Arguably one of the most significant advances for oxide growth has been the inclusion of oxygen-plasma as the oxidizing agent in MBE or MOCVD [13, 14, 6, 15, 9, 16-22]. Oxygen plasma, which is typically produced by inductive coupling to a radio frequency field and injected into the growth chamber, can produce highly uniform fluxes with monatomic oxygen densities as high as 10^{22} m^{-3} [23-25]. In the case of MBE growth, pure oxygen is normally used whereas in MOCVD methods there is often a carrier gas employed, though numerous variations of these techniques exist. Such high concentrations of oxygen allow for growth to be carried out at substantially lower pressures than using non-ionized oxygen (O_2) would allow and therefore offer inherent advantages in morphology. It is important to note the contributions made by PLD to the study of oxide thin films [11, 4, 5, 8, 26-34]. With advances in pulsed laser technology,

laser deposition has demonstrated films of comparable or superior quality, and so it remains a key method in the investigation of such oxides. However, the drawbacks of PLD such as difficulty in achieving large area uniformity and increased complexity in maintaining stoichiometry make it less inviting for commercial interests and, in fact, some research-motivated endeavors (such as large-area device structures).

With these technologies employed the quality of oxide films has advanced tremendously. Though these compounds were all studied in bulk form several decades ago the possibility of highly pure, highly crystalline and stoichiometrically controllable oxide thin films has opened new avenues of research. Interest in the compounds has grown steadily as progress has continued for all three of these compounds for almost 2 decades. Figure 1 shows the number of publications by year for “ZnO thin films”, “MgO thin films” and “NiO thin films”, as indexed by ISI.

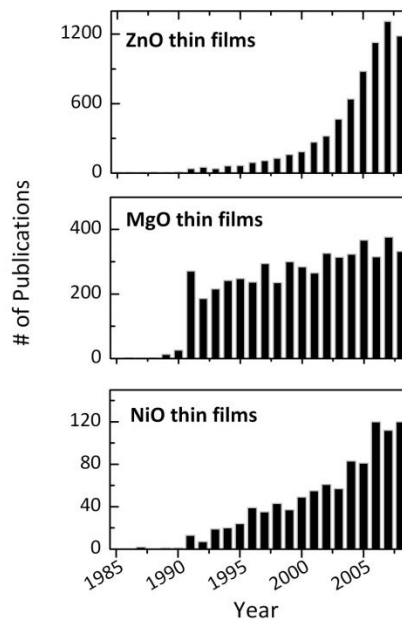


Figure 1. Number of publications by year for each of the oxide binaries ZnO, MgO and NiO. Source is ISI indexing.

However, upon surveying the literature relating to these oxides it becomes evident that the growing interest in them is not merely a result of the novelty of improved quality. Each of these materials possesses properties that researchers are seeking to exploit for specific, and in some cases far reaching, technologies.

NiO, for example, is antiferromagnetic and is exploited in spin valve devices [35-37]. It also exhibits a unique phenomenon termed “negative” resistance or resistive switching [38-44], which can be exploited for rewritable random access memory (Re-RAM). It has become the subject of extensive theoretical and experimental studies in the field of electronic structure modeling because of its persistently ill-accounted for electronic properties [45-54]. NiO, which has been considered the prototypical Mott-Hubbard (or simply Mott) insulator [55], has since been re-designated as having properties at the boundary between Mott-Hubbard and charge-transfer type insulator [56, 47], though controversially so [46]. It is reasonable to state that NiO has the most exotic and perhaps least understood properties of the three binaries. The value of the optical band gap itself is the subject of some debate, normally reported to be 3.6 – 4 eV, and possibly dependent upon growth conditions. Importantly, NiO is also intrinsically p-type due to a favored excess of oxygen in the stoichiometry, and has been used as the p-type region in heterojunction devices and as a p-type transparent conducting oxide (TCO) [57, 58, 29, 59-63, 33].

ZnO ($E_g = 3.37$ eV) is far better established as an optoelectronic material and has been the most acclaimed of the three compounds to that end, a fact punctuated by Figure 1. It is well known in the semiconductor community for its large exciton binding energy of 60 meV [64-66], which has enabled lasing at temperatures as high as 570 K [67]. ZnO is also a very useful TCO

oxide and can achieve superior conductivities on the same order as the ubiquitous indium tin oxide (ITO) [68]. ZnO has been used in various optoelectronic devices [69, 66, 70]. Notably, ZnO was of greater interest historically for its piezoelectric properties [71-73]. In contrast to NiO, ZnO is intrinsically n-type as a result of inherently oxygen-deficient stoichiometry [74, 69, 66]. ZnO itself has a wurtzite (B4) crystal structure and therefore is not compatible with the other two pertinent binaries. However, the ternary compound $\text{Zn}_x\text{Mg}_{1-x}\text{O}$ is cubic rocksalt structure (B1) for concentrations of Zn less than approximately 0.4 [75, 27, 76, 77, 32, 78].

MgO has an exceptionally wide band gap of ~ 7.8 eV and is a well studied material. It can be grown in large diameters (>7.5 cm) and is a refractory material ($T_{melt} = 2800$ °C) with a good thermal conductivity [79, 80]. For these reasons it has been used extensively as a substrate material [13, 4, 8, 81, 82]. MgO has excellent optical quality and is robust against plasma, exhibiting an “anti-sputtering” property in such ionic environments. For this reason it has been used almost exclusively as the protecting material for discharge electrodes in plasma display panels [83-86]. These same properties make it desirable as a substrate for plasma assisted growth methods. More central to this work, however, is the capacity of Mg to increase the band gap of NiO and ZnO when alloyed with them.

Because NiO and MgO both have cubic structure and the cations have similar ionic radii, these oxides readily form homogeneous ternary compounds with each other and allow for a continuous range of concentrations, $\text{Ni}_x\text{Mg}_{1-x}\text{O}$, for $x \in (0, 1)$. Over this range the lattice constant varies by less than 2% (4.215 to 4.178 Å), and is approximately linear with respect to concentration [87]. The band gap of the compound has also been shown to be an approximately direct function of Mg concentration (1-x) [48, 88, 89], shifting from the MgO value of 7.8 eV to

the NiO value, ~ 4 eV. However, while binary NiO has been grown in thin film form for decades [90, 91, 14, 92], to the author's knowledge the epitaxial growth of the ternary compound remains virtually unexplored. The existing experimental studies of the semiconductor properties of $\text{Ni}_x\text{Mg}_{1-x}\text{O}$ have been mainly on powder forms of the compound [93, 94, 48, 87] or of solids formed by calcinations of powders [95, 88]. In the exhaustive search for relevant studies, only one publication has been found which examines the use of this compound for optoelectronic applications [89]. This study employed the sol-gel method and the films were not lattice-matched to the substrates used. Further, it only characterized four concentration values (x). $\text{Ni}_x\text{Mg}_{1-x}\text{O}$ thin films for optoelectronic applications therefore represent a potentially very fruitful topic of study, particularly given the shrouded nature of the electronic properties of NiO. It is for this reason that the research goals presented herein are predominantly oriented towards this ternary film.

$\text{Zn}_x\text{Mg}_{1-x}\text{O}$ films, on the other hand, hold a very different status as semiconductor materials. This compound has been of growing interest for optoelectronic applications for several years and is being studied extensively as such [75, 27, 76, 30, 96, 97, 77, 22, 98, 32, 99, 68, 100, 62, 34]. It has been demonstrated that integration of Mg into ZnO increases the band gap energy as an approximately linear function of Mg concentration. Such integration maintains the wurtzite structure for Zn concentrations (y) as low as $y \approx 0.47$ [97, 32, 78], though phase segregation has been observed in some cases at higher Zn concentrations ($y = 0.64$) [75]. As mentioned, at higher Mg concentrations ($y < 0.4$) the crystal becomes rocksalt (B1) crystal structure. This compound has been grown in both forms with excellent optical and electronic properties and has been exploited in devices [101, 89, 99, 102, 62]. Thus, this ternary film does

not present the same opportunities for research as does $\text{Ni}_x\text{Mg}_{1-x}\text{O}$. However, the attribute of importance here is that $\text{Zn}_x\text{Mg}_{1-x}\text{O}$ has shown to maintain its n-type nature with Mg integration [68, 103, 34]. It therefore may be possible to exploit cubic $\text{Zn}_x\text{Mg}_{1-x}\text{O}$ films to produce a lattice-matched, high quality heterojunction with $\text{Ni}_x\text{Mg}_{1-x}\text{O}$. While this is not an immediate objective of this research, the research plan presented may enable such structures to be produced in future endeavors.

The value and novelty of the investigation of these oxide films is therefore evident. The research here is presented as an organized attempt to qualify the discussed compounds for optoelectronic applications. The first major section of the document will describe the experimental methods employed by the author. This section is subdivided into discussion on the method of growth, film characterization, device fabrication and device characterization. The second major segment presents all significant results in four categories of film growth, characterization and exploitation. And finally the document will be summarized in a brief conclusion.

2. EXPERIMENTAL METHODS

Plasma Assisted Molecular Beam Epitaxy

While various thin film growth techniques have been applied to oxide growth, molecular beam epitaxy (MBE) offers unsurpassed in-situ diagnostic capability and can produce excellent quality epitaxial films. Molecular beam epitaxy was developed at Bell Labs in the 1960's and has since been exploited for thin film growth of nearly every significant semiconductor material. MBE systems typically operate at pressures ranging between 10^{-9} and 10^{-6} Torr and can sustain background pressures on the order of 10^{-11} Torr when inactive. The low pressure growth environment and slow deposition rates enable excellent epitaxial growth to be achieved.

System

The system utilized for this research is an SVT Associates oxygen plasma-equipped growth chamber integrated into a Riber MBE sample transfer system. A diagrammatic representation of the full system is shown in Figure 2 along with a picture of the system itself. The growth chamber is vertically oriented and is equipped with oxidation resistant parts and materials. Figure 3 shows a diagram of the oxide growth chamber with basic elements highlighted and a photograph of it.

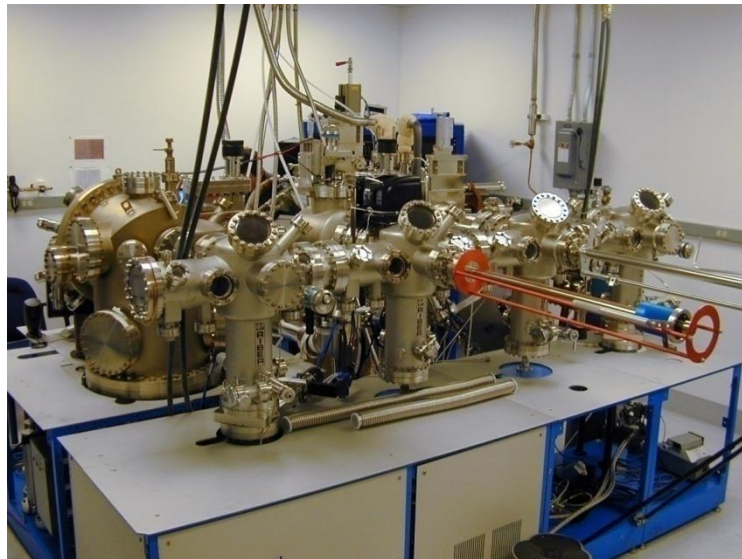
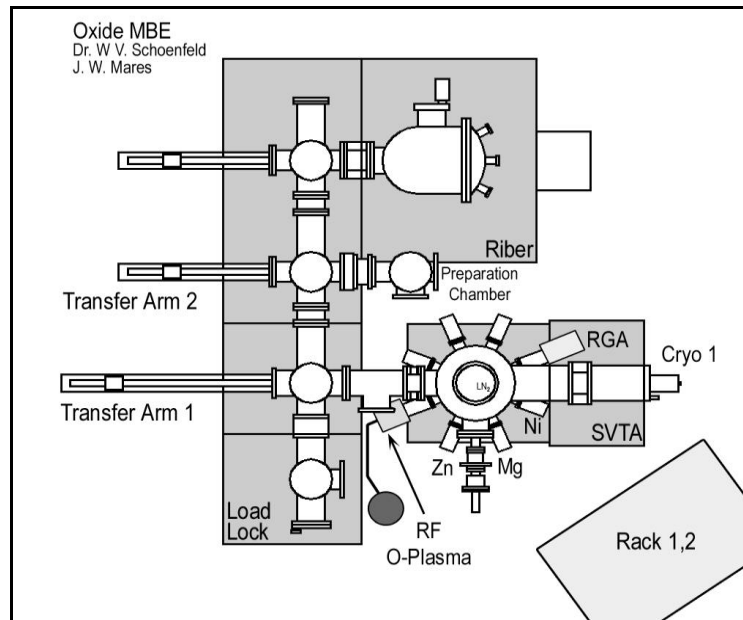


Figure 2. (Top) Diagram of the MBE system used for oxide thin film growth shown with (bottom) a photograph of the system.

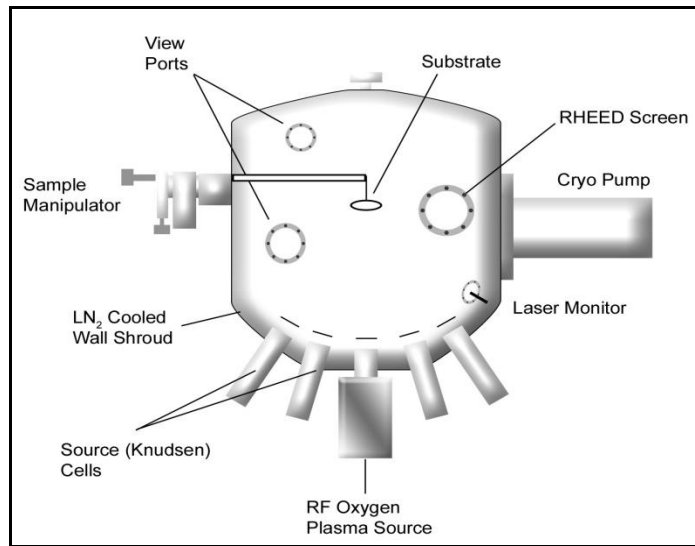


Figure 3. (Top) Diagram of the oxide molecular beam epitaxy chamber shown with (bottom) a photograph of the chamber.

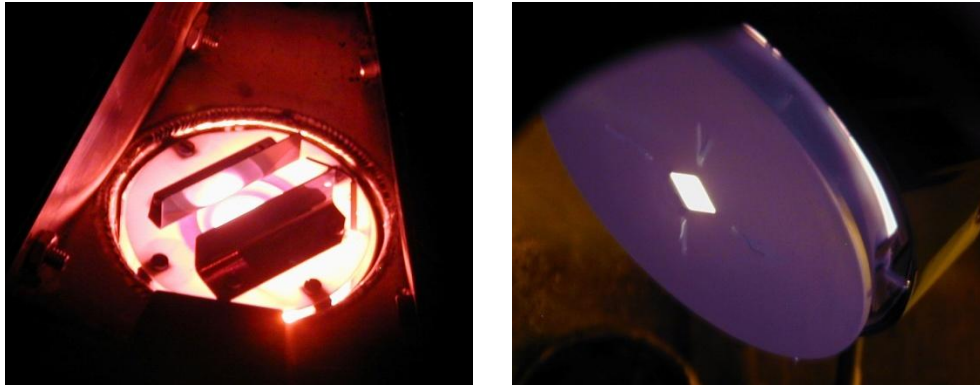


Figure 4. (a) The Oxygen plasma injector during operation and (b) a 1 cm² MgO substrate on a Molybdenum substrate holder.

Growth is carried out on substrates fastened to molybdenum sample holders which are held at elevated temperatures in the chamber center on a sample manipulator. The manipulator controls the x, y, z and θ positioning of the substrate to facilitate the various forms of in-situ measurement. The oxygen source used in this research is an SVT Associates RF 4.50 inductively coupled radio frequency oxygen plasma injector. This injector applies a radio frequency (13.56 MHz) driving current to an alumina chamber with a thru-flux of oxygen in order to generate monatomic-rich oxygen plasma. Figure 4 shows both the oxygen plasma injector and the substrate holder during growth. The oxygen used is 4.5N purity electronics grade O₂. Flux of oxygen is controllable over the range 0 – 5 sccm. Elemental sources (Zn, Mg, Ni) are thermally evaporated from crucibles held in Knudsen Cells (K-Cells) affixed to ports on the bottom flange of the growth chamber.

Film Characterization Methods

An inherently critical and central aspect of thin film growth is the characterization of the films themselves. The various means of film assessment and characterization are very specific and, in general, relatively sophisticated techniques. Particularly for films considered to be novel in their realization, it is important to ascertain that the films are in fact crystalline and have (or do not have) the desired properties.

The characterization of all the films, both ternary and binary, is essentially the same. It is reasonable to divide the film characterization into 3 categories: structural/compositional, optical and electrical. The means of characterization in each of these categories will be presented here and are broken into two general categories, *in situ* and *ex situ*. A distinct advantage of MBE is the capability to perform multiple in situ measurements. The advantage of in situ measurements is that they can be extremely formatively useful. This is to say that input from these measurements can be used to alter or steer growth parameters during film growth. Ex situ methods present no particular advantage, *per se*, but include critically imperative measurement techniques such as X-ray diffraction and atomic force microscopy.

In Situ

Two important measurement apparatuses used in this research are the reflected high energy electron diffraction (RHEED) system and the laser interferometry system. The former measurement technique is perhaps the best known and the most ubiquitously used in epitaxial growth. RHEED provides essential information about the crystal surface prior to and during

growth. The immediate value of RHEED to this research is mainly in the qualitative information it provides about surface smoothness. RHEED can also be used in several highly quantitative ways, including growth rate measurement through intensity oscillations. Such measurement, however, necessitates an atomically smooth crystal surface and monolayer growth such as those achieved in GaAs epitaxial growth, among others. In the case of this research, the novel films are not expected to be of the same morphological quality as the more mature semiconductors like GaAs. The alternative method used to monitor film growth rate is laser interferometry.

In laser interferometry, a laser/detector system is setup to monitor the time-dependent reflectance of the crystal surface. Multiple reflections occurring at the interface between the substrate and the thin film result in a reflectance which varies as the layer increases in thickness. As the film grows, the reflectance is modulated in an approximately sinusoidal manner (for a single homogeneous thin film). By analyzing the rate of oscillations, the growth rate can be extracted. Approximate error in thickness measurement by this means is less than 10 nm. Additionally, by assessing the amplitude of the oscillations the surface quality of the thin film can be monitored. This monitoring is effective even with surface roughness much greater than that which can be interrogated by RHEED. Figure 40 (provided earlier) shows a laser interferometry curve measured for a ZnO thin film grown on Sapphire. The change in growth rate illustrated is due to changes in the temperature of the Zn Knudsen cell.

Ex Situ

Rutherford Backscattering

One of the more frequently exploited analyses that will be carried out on the films is compositional characterization by Rutherford Backscattering (RBS). In RBS, high energy ions (in this case He^{+2} of approximately 2.0 MeV) are accelerated into the sample surface. By measuring the deflection angle of the reflected ions, not only can the surface composition of films be interrogated, but also the depth-dependant composition profile of a multilayer structure can be determined by fitting an energy spectrum of backscattered ions. Such a spectrum was shown in Figure 56. The RBS measurements will be carried out at the Advanced Materials Processing and Analysis Center (AMPAC). The spectra obtained will be fitted by the student using a well-known freeware program called RUMP.

Spectrophotometry

The use of spectrophotometry to characterize films is a very convenient and informative way to assess film optical quality. As presented in the section of this document on CdZnO thin film characterization, the author has done relatively extensive work with this method and the methodology is described thoroughly in that section.

It should be pointed out here that there are several approaches to spectrophotometry utilized in the research. The differentiating factor between them is largely an issue of time versus accuracy. Because the primary substrate in use will be MgO (and all of the films grown will have a lower band gap than the substrate), the author has the luxury of using transmission

measurements which is experimentally simpler in some ways. However, reflection measurements may also be made.

In the case of transmission spectrophotometry, it is often not important to know the absolute transmittance of a film. Instead, when a film is initially being characterized, it is only important to know relative transmittance. Even in the relative measurement, the spectral absorption edge (interband absorption being the mechanism in this case) can be assessed. This is an important note because substrates are, for economical reasons, usually only polished on one side. The unpolished side has a roughness on the order of micrometers and is therefore highly scattering of the light. Typical reduction in transparent regions is approximately a factor of 4, but is wavelength dependent.

In order to make a more accurate assessment (though not more precise, in general), the substrate must be optically smooth on both sides. This can be achieved either by polishing the rough side of a MgO substrate, post-growth, or by simply growing on double-side polished substrates. The latter option may be chosen at some point if film quality and repeatability merit such an accurate investigation. The former option is less ideal but is likely to be exploited over the latter in the case of more routine characterizations.

Atomic Force Microscopy

Atomic force microscopy (AFM) will be the most heavily relied upon means of initial interrogation of thin film morphology. Tapping mode AFM will be used to characterize most if not all of the films' surface structure. Initially in any growth series, AFM will serve as the qualifying technique which assesses the film quality in a general "first-look" sense. As discussed, once the films of a series achieve a certain minimum roughness, it is more likely that

they will be highly ordered single crystals. The AFM used is the Veeco Dimension atomic force microscope.

X-Ray Diffraction

In crystal structure and quality determination, no technique is more fundamental nor more informative than X-ray diffraction (XRD). XRD is a fundamentally simple experimental procedure in which X-ray radiation is diffracted from a sample and detected at some diffraction angle. Standardized methods of XRD are widely varied and well established and allow for unparalleled assessment of crystal structure and quality. Of critical importance here is the ability to assess crystal structure or phase as well as the films lattice parameter. The XRD system used for this research is a Rigaku II x-ray diffraction system which exploits the typical Cu-K α radiation line, $\lambda \approx 1.54056 \text{ \AA}$. Specific discussions about relevant lattice parameters are presented in those sections.

Device Design & Fabrication Techniques

The device fabrication techniques employed to produce the devices studied are largely standard photolithographic, metallization, etching and packaging processes. Also, device design constituted a small but notable component of the research conducted. Here a basic overview of these procedures – with mention of the specific software, equipment and chemicals used – is presented. More detailed discussions about some specific device processes are included in those appropriate sections.

The facilities used include two class 1000 cleanrooms (College of Optics and Photonics, University of Central Florida), both of which have class 100 subsections within them. Additional labs include the two device packaging and characterization labs also in the College of Optics and Photonics. The two former labs were used for photolithography processes, metals deposition, acid etching procedures and annealing. The latter two labs contained equipment used for sample scribing, device baking (with epoxy, for example) and wire bonding.

In general, device design and fabrication may consist of multiple phases. First, designing the appropriate photomask(s) using software such as L-Edit was frequently necessary since no existing masks were initially available to the author. This was followed by either fabrication of the photomasks in-house, using the Leica electron beam lithography tool, or out-sourcing them through a manufacturer such as PhotoSciences. These were only prerequisites to the fabrication of the devices themselves. Figure 5 exemplifies one type of device designed (MSM, in this case) using L-Edit.

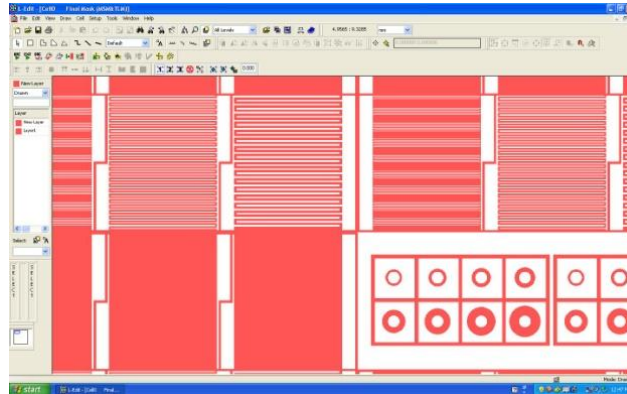


Figure 5. Screen shot of the software used for photomask design, L-Edit.

Device fabrication includes typical procedures such carrying out necessary photolithographic steps (photoresist application, baking, exposure, development etc.), metals deposition, material etching, metals lift-off and device annealing. The vast majority of photolithographic processes used – though widely varied in some respects – relied upon the positive photoresists, S1813 and S1805 (Shipley). In brief, the positive photoresist would be spun onto the samples at speed ranging from 5000 to 8000 RPM. This would result in photoresist thickness ranging from approximately 1 μm to 1.75 μm , depending on sample size, surface smoothness and other factors to a lesser degree. The samples would then be soft-baked at 115 $^{\circ}\text{C}$ for 1 minute to evaporate solvents from the resist and promote polymer cross-linking. The sample would be exposed to ultraviolet light using the appropriate masks and exposure times (typically 8 – 15 seconds on the Karl-Seus MJ-B3 mask aligner, though other UV sources have been used), and then developed in a 1:5 solution of 351 developer-to-water ratio for 60 seconds. Many subtle variations in the process were made over time and parameters are frequently

revisited for different films and substrates. Once the photolithography was complete, the proceeding step could then be taken such as metallization or acid etching.

Many devices presented here are of metal-semiconductor-metal (MSM) architecture. These represent the simplest kind of optoelectronic detectors in that they function as photoconductors. Essentially, two metal electrodes are with a small spacing between them. This is commonly accomplished by an array of interdigitated “fingers”. Light incident on the devices can, in principle, promote electrons into the conduction band and effectively reduce the resistance of the device. By applying voltage and measuring the device current under different optical excitations the photoresponse can be characterized. The mask design and implementation for these devices is very simple and requires typically only one mask and one metallization step. Figure 6 shows two MSM devices of different design: one optimized for speed and the other for sensitivity.

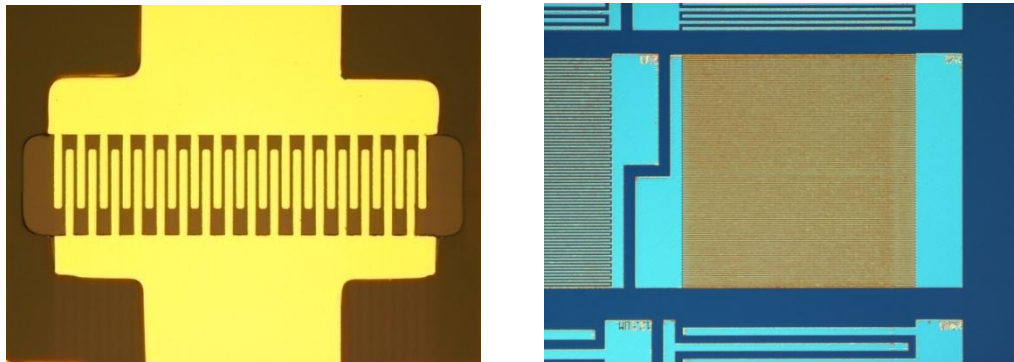


Figure 6. Two MSM devices of different geometry. That on the left is a small-area detector optimized for response speed while that on the right large area and is designed for sensitivity.

Other types of devices required more sophisticated processes. The most elaborate devices in this document are those presented in the *Hybrid and Fully-Oxide Devices* section. In brief, these structures are vertically layered p-i-n structures. Thus, to make contact to both the p- and n- regions (and because of the insulating substrates) an etching step had to be included. For these devices there were a minimum of 3 photolithography steps and therefore three mask designs as well. Typically, the etching of needed mesas was carried out first, followed by the photolithography and metallization for the p- and n- contacts.

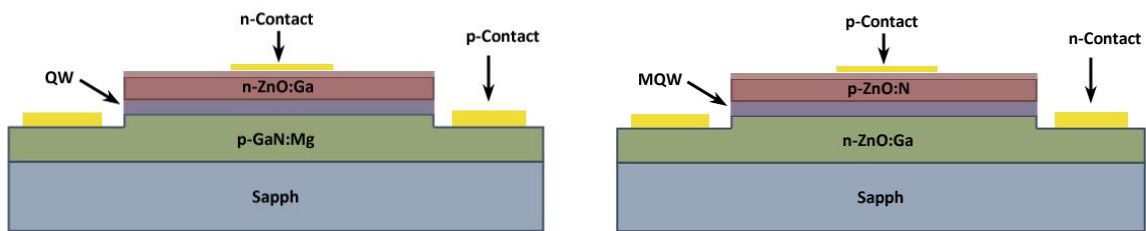


Figure 7. Structural diagram of the hybrid GaN-ZnO LEDs (left) and fully-ZnO LEDs (right).

For some of these more elaborate devices, additional post-fabrication steps are followed in order to facilitate. In specific, it was often useful to wire bond the devices in order to interface with them electrically. Such wire bonding was used in the cases of the hybrid and fully ZnO LEDs and this can be seen in Figure 70 and Figure 74. This was accomplished by scribing the devices into single LEDs, bonding them onto device headers (typically TO-46 headers) and then connecting the device contacts to the header leads using a Kulicke & Soffa 4524AD manual wire ball bonder. In all cases where wire-bonding was employed, a 1 mil (25 μm) gold wire was used. The wire bonder used is shown in Figure 8.



Figure 8. A Kulicke and Soffa 4525AD manual wire bonder.

Device Characterization Techniques

Electrical and optical characterization of devices represents the last step carried out in the cycle comprised of film growth, film characterization, device fabrication and device testing. However this portion of the research comprises, at the time of this document, a small fraction of the overall effort for any of the devices presented herein. Yet the illustration of device functionality was absolutely imperative in all of these cases. For this purpose, several important pieces of electronic and optical equipment were required.

For electrical characterization of devices, a key measurement apparatus used frequently is the Signatone 1160 probe station. The probe station facilitates electrical connection with the device through either two or four needle-like probes. The probes themselves are connected to a source meter such as the Keithley 2400 which can measure device current-voltage characteristics directly. Such probe stations are very important and standard equipment in electronic component characterization. The probe station used here is shown in Figure 9 alongside a Keithley 2400 source meter. Figure 10 shows an MSM device under test on the Signatone probe station.



Figure 9. The Signatone 1160 probe station (left) used for electronic characterization of devices shown with a Keithley 2400 source-meter (right).

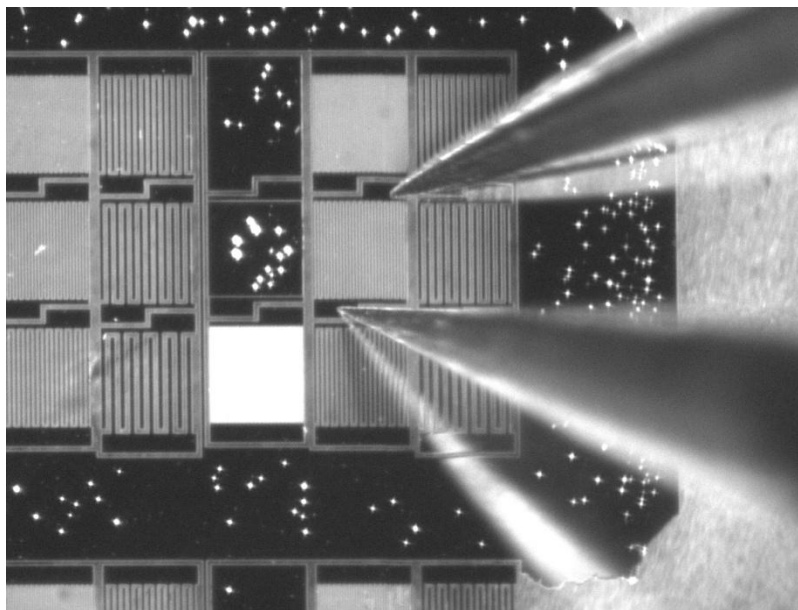


Figure 10. Image of a ZnMgO MSM device under electrical testing for IV characteristics.

More central than simply the electrical characterization of devices is the spectral characterization of them. There are two general types spectral characterization presented in this work. Either the devices are emitters and therefore their emission spectrum is of primary interest, or the devices being studied are detectors and their spectral detection characteristics are sought. In both cases, the equipment used is essentially the same and relies upon the spectrometer available to the author, a Newport/Oriel MS257 $\frac{1}{4}$ meter spectrometer/monochromator. This spectrometer is outfitted with gratings of 150, 300, 600 and 1200 grooves per mm. All gratings are aluminum and the two highest resolution gratings have a blaze wavelength of 400 nm. These gratings therefore have sufficient response in the ultraviolet to be useful in such measurements.

In the case of emission spectrum measurements, a detector is placed at the monochromator output with the device positioned at the input. More correctly, the device must be imaged onto the input slits using appropriate optics (such as UV specific ones, when necessary) and its spectrally divided, slit-apertured image appears on the output slits to be measured. In the case of spectral detection, the device is located at the output (after appropriate optics) and the lamp used for illumination is imaged upon the input slits. The detector in this case is under bias by a source-meter such as a Keithley 2400 and the current through the device is measured when illuminated by the specified wavelength, as available by the lamp used. A diagrammatic representation of the setup is shown in Figure 11.

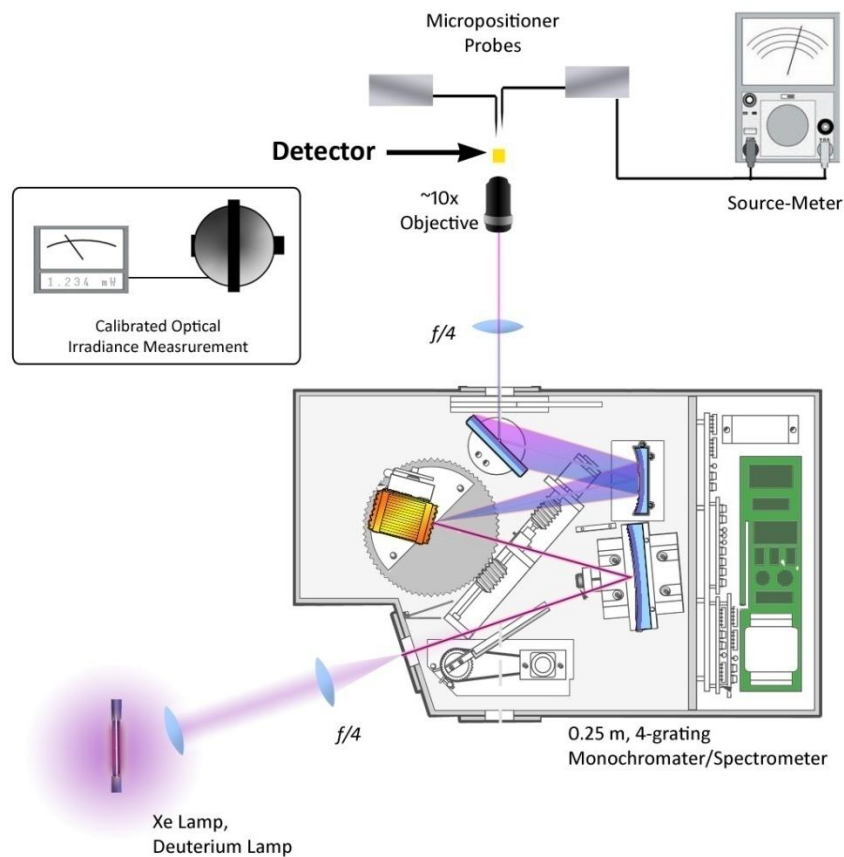


Figure 11. Diagram of experimental setup for characterization of device spectral response.

Various degrees of sophistication and effectiveness were realized for the spectral detection setup. The actual experimental setup which finally observed a detector response (in the case of MSM devices presented herein), was the result of many refinements of the setup itself as well as the author's ability to effectively use the equipment. Two variations in the detection setup are shown in Figure 12. The first (top) setup uses a mirror to redirect the light emitted from the spectrometer down onto the sample which rests on the optical table, oriented up. Probe positioners mounted on the table make electrical contact to the specific device under test and are connected to the Keithley source meter. In the later refinements of the setup (Figure 12, bottom)

a custom made device stage holds the sample at beam height and oriented facing the illumination, eliminating the need for the lossy mirror. Both setups include a microscope objective which was necessary for the user to see the devices during probe positioning, which is a challenging task. Figure 13 shows a device being tested and illuminated by blue, green and red light emitted from the Xenon lamp used in that case.

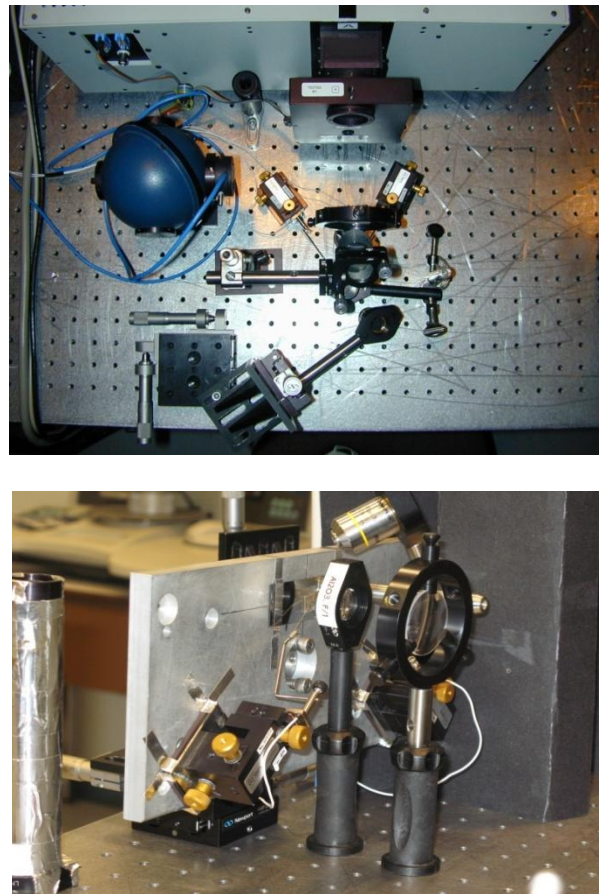


Figure 12. (top) An early setup for detector spectral response including an aluminum mirror just prior to the device which is mounted on the table top facing up. (bottom) A more recent detector spectral response in which the device is mounted laterally on a custom stage equipped with probe positioners.

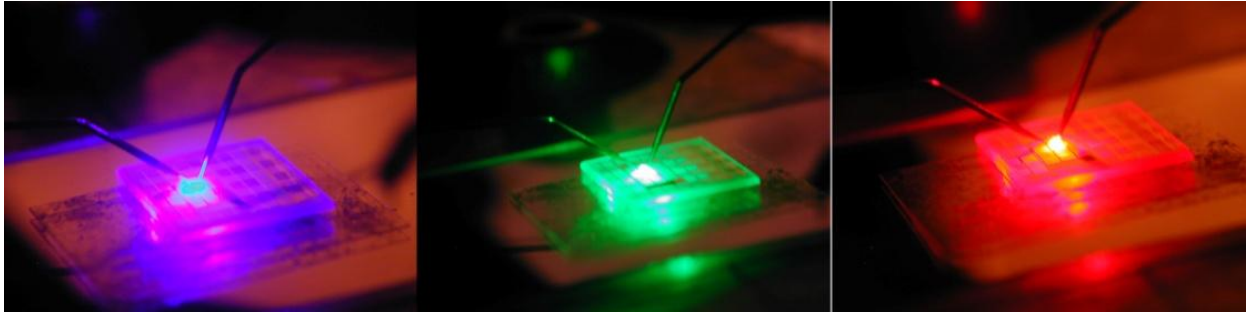


Figure 13. Images of a NiMgO MSM device under spectral testing, illuminated here by radiation with wavelengths 420 nm, 535 nm and 635 nm from left to right.

3. RESULTS

This section of the document presents the condensation of all progress made towards the growth, characterization and application of the relevant oxide thin films. Because the focus of research shifted between the distinct yet related oxide films, the results are presented in segments which roughly reflect the chronological order in which research was conducted. This order cannot be strictly abided by in all cases, however, since some topics were studied concurrently, or were left and then returned to later in the endeavor. It serves particularly well to present the research in this order with regards to the progression from binary oxides (MgO, ZnO or NiO) to the ternary. The binary films were necessarily grown first and are inherently easier to grow. The discussion proceeds from the binaries - focusing on MgO and NiO first – to the ternary compound NiMgO, which constitutes some of the most novel and complete work presented herein. The growth of binary ZnO is briefly presented and then ZnMgO growth and characterization.

After the discussion about the two ternary compounds of primary interest, an additional section is included which focuses on various aspects of characterization and exploitation of the wurtzite ternary thin film CdZnO. The films and structures used for this portion of the research were grown not by the author, but by a collaborating institute SVT Associates, the company which designed the MBE system in use by the author. This research was conducted prior to the research on growth and characterization of NiMgO or ZnMgO, but is included after these to indicate that it is less central to the thesis. However, the work was very successful and productive, yielding several new results such as the first observation of light emission from a CdZnO/ZnO/GaN hybrid structure light emitting diode. Thus, while this topic is peripheral to

the primary points of interest, it constitutes a very relevant and significant fraction of the overall research effort.

It should be noted that, while the functioning MSM detectors are of defining importance to the topic, their fabrication and testing makes up only a very small fraction of the work conducted. The majority of effort has been unambiguously focused upon the film growth and characterization. The presentation of MSM devices, therefore, serves as a capstone of the body of work presented, not a foundation. As such, the demonstration of the functionality of these devices as solar blind detectors punctuates the success of the predominantly materials growth-oriented program.

MgO

An important precursor to the growth of high quality ternary cubic films was the realization and refinement of MgO films. In particular, it was important to achieve homoepitaxial MgO films of excellent quality which could then act as a nucleation layer for the ternary films, thereby promoting better ultimate quality of the films. More importantly, it was initially conjectured that MgO would serve as the “base” compound into which Ni and Zn would later be integrated. It was thought that MgO films growth parameters would be first optimized and the transition metals would be added. This presumption will be discussed in further detail with regards to the problem of the transition metal (Ni, Zn) integration. This section presents various aspects of the MgO film growth and characterization for both hetero- and homoepitaxial cases.

MgO Heteroepitaxy

The first cubic oxide film growth carried out was MgO on (111)-oriented Si. The objective was not only to verify that MgO can be nucleated and grown on Silicon, but also to economically characterize the general growth parameters for this material. The Silicon orientation was selected only on convenience of already available high quality substrates with the appropriate dimensions.

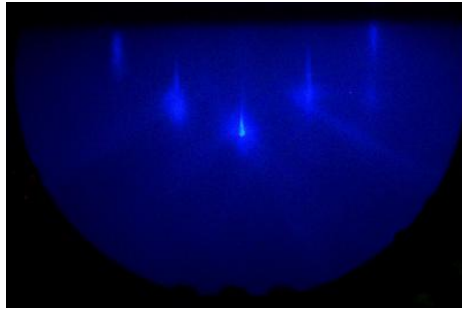


Figure 14. A RHEED image of a Si(100) surface after cleaning and degassing.

Prior to growth, Si substrates were cleaned by the (full) RCA method and initially examined with AFM and RHEED for morphology. AFM revealed surface roughness $< 2.5 \text{ \AA}$ and RHEED was streaky, indicating good crystalline quality (Figure 14). Growth was carried out at substrate temperatures in the range $200 \text{ }^\circ\text{C}$ to $500 \text{ }^\circ\text{C}$.

Figure 15 shows the laser interferometry data along with RHEED images taken during an extended growth of MgO on Si with the substrate temperature of $200 \text{ }^\circ\text{C}$. The growth shown took place over approximately 18 hours and constitutes a growth rate characterization over a broad range of Magnesium cell temperatures. Several characteristics are notable. The oscillation amplitudes remain approximately constant up to a cell temperature of $575 \text{ }^\circ\text{C}$. This implies that the growth leading up to this point (the first 700 minutes) did not have a severe degenerative effect on the surface quality. Also, the RHEED images indicate that while polycrystalline order dominated the growth initially (circular RHEED pattern), with increasing Mg cell temperature the surface quality improves somewhat with cell temperature of $555 \text{ }^\circ\text{C}$. This improvement is not only evident in the elongated, streaky RHEED spots, but also in the slight increase of reflectance at that point during the growth. Above $575 \text{ }^\circ\text{C}$ the quality degenerates and the surface roughens, also as indicated by both RHEED and interferometry.

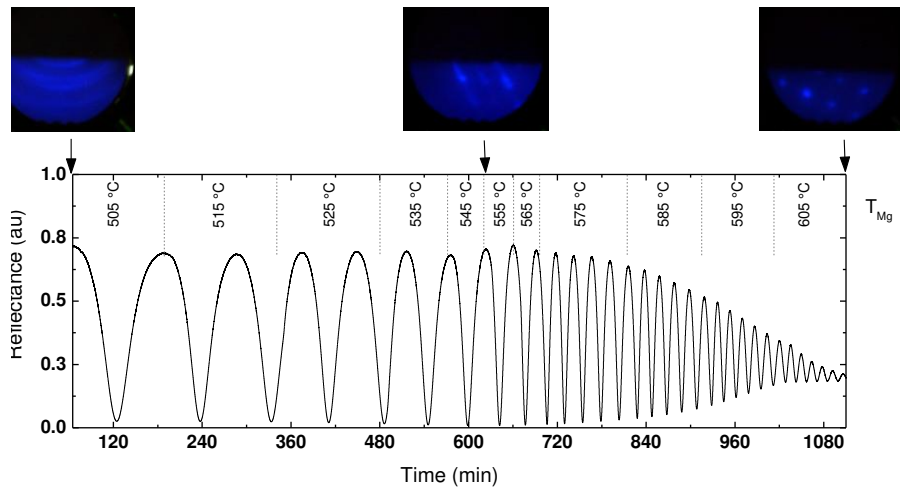


Figure 15. Laser Interferometry curve for MgO on Si(111) with a substrate temperature of 200 °C. The change in oscillation frequency is due to increasing Mg K-Cell temperature

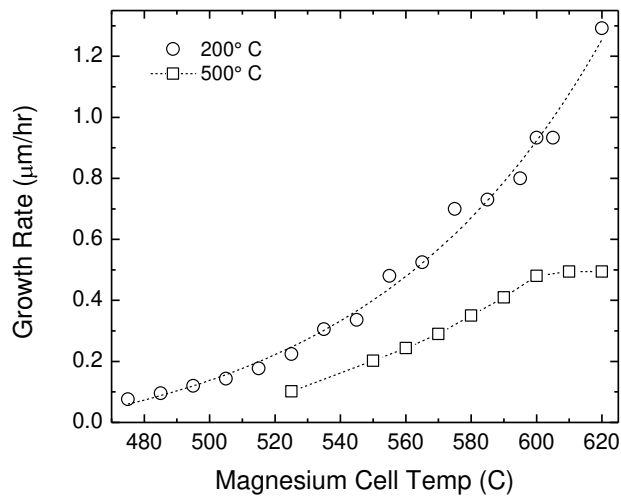


Figure 16. Growth rates for MgO on Si with two substrate temperatures, 200 °C and 500 °C

The interferometry data shown above was analyzed to produce the upper growth rate curve shown in Figure 16. Note that the rate is strictly increasing for the 200 °C substrate temperature and follows an exponential-like trend. Similar analysis was carried out for a substrate at 500 °C to produce the lower curve. Note that the growth rates for the higher temperature substrate are substantially lower than those for the 200 °C substrate. Additionally, a different behavior is exhibited by the higher temperature sample in that the growth rate saturates at a Mg cell temperature of 600 °C. The reduction of growth rate may be attributed to decreased sticking coefficient due to the higher temperature surface. The fact that there is a plateau in the growth rate of the 500 °C sample implies that MgO growth is limited to (approximately) stoichiometric crystal formation. In the case of the 200 °C substrate, it is likely that additional magnesium also adheres to the surface and does not re-sublimated as it would be for higher growth temperatures. This additional magnesium effectively degrades surface quality and worsens semiconductor properties.

Heteroepitaxial films were characterized with spectrophotometry and AFM. Figure 17 shows the spectral reflectance of a MgO film grown on Si. The large oscillation amplitude above 270 nm indicates film transparency through the visible (and near-UV), as is expected. The increasing absorption between 260 nm and 200 nm (4.77 eV – 6.2 eV) is due to interband transition and is indicative of the band gap energy. Reasonable surface morphology was also achieved even for films as thick as 2 μm. AFM of a heteroepitaxy film is also shown in Figure 17. Note that the structure is clearly cubic and maintains the (111) orientation inherited from the substrate. RMS roughness less than 20 nm was achieved in some films. Further optimization of films was not pursued as it was less critical than other objectives in the research

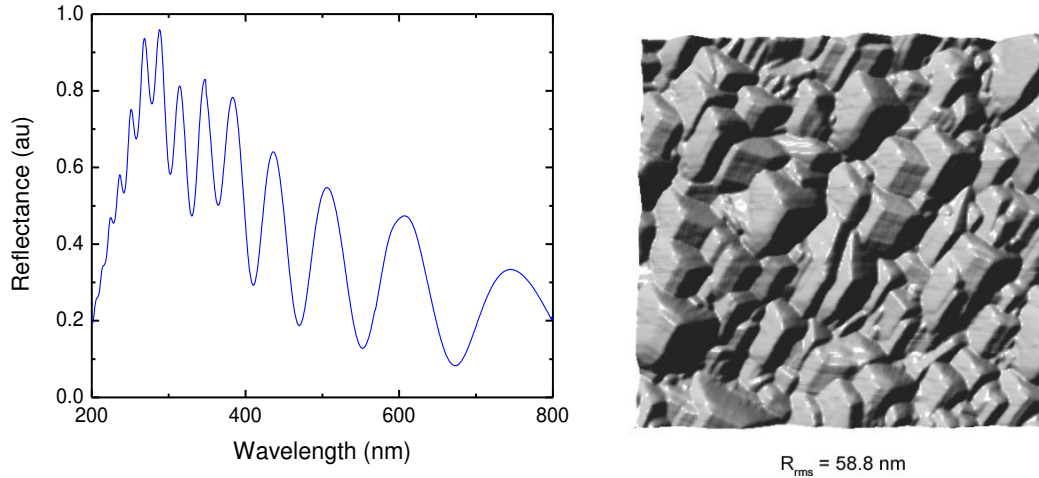


Figure 17. (a) Spectral Reflectance and (b) Atomic Force Microscopy of MgO thin film grown on Si. The film orientation is evidenced by the triangular-based structures and is inherited from the (111) oriented Silicon substrate. The vertical z-axis scale for (b) is $\pm 500 \text{ nm}$.

MgO Homoepitaxy

A very important preliminary aspect of the main research conducted was the realization and optimization of homoepitaxial growth of MgO. Early samples, grown prior to process refinement, had surface roughness on the order of 100 nm or more and were either strictly amorphous or very rough. The proper selection of substrates temperature, Mg K-Cell temperature, oxygen flux and substrate treatment were all critical factors in this optimization. The final resultant films exhibited RMS roughness less than 1 nm and were consistent in quality.

One early assumption made that was later found to be incorrect is that optimal growth quality is achieved at the stoichiometric-limited point. Efforts were therefore made to operate at this pressure/cell temperature as determined by analysis like that shown in Figure 16. For the 9

mm aperture, the stoichiometric-limited point corresponded to a Mg cell temperature of approximately 600 °C; for open-crucible evaporation point was shifted to 490 °C. Growth at this magnesium cell temperature did not result in smooth morphology however. Figure 18 shows the AFM of one such film. Interestingly, it was quite common that films grown at this condition would take on a triangular symmetry (as shown) which implies (111) crystal orientation. Roughness of such films could not be reduced below about 12 nm, RMS. Thus the condition of stoichiometric-limited growth was abandoned for growth in oxygen rich conditions.

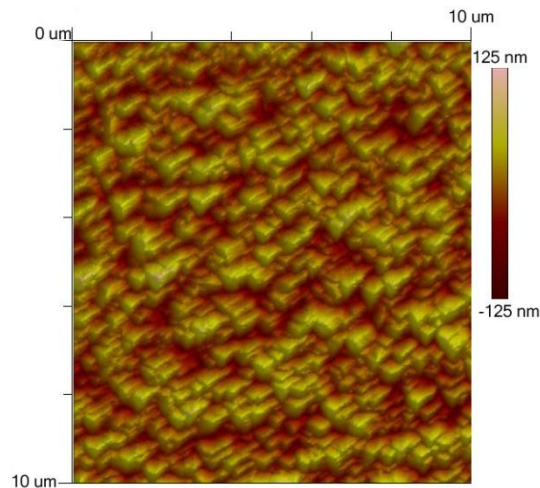


Figure 18. AFM of a MgO homoepitaxial film grown at the stoichiometric point in the Mg pressure curve. Note the (111)-like orientation resulting from fast growth rates despite the (100) substrate orientation.

By decreasing the Mg cell temperature (and therefore growing at a higher chamber pressure), better quality films were grown. The best growths achieved were grown at a pressure of 8 – 14 μ Torr with the Mg K-Cell temperature at 440 °C and a substrate temperature of 500-600 °C. Figure 19 shows the improvements in morphology, including evidence of the proper (100) orientation as inherited from the substrate.

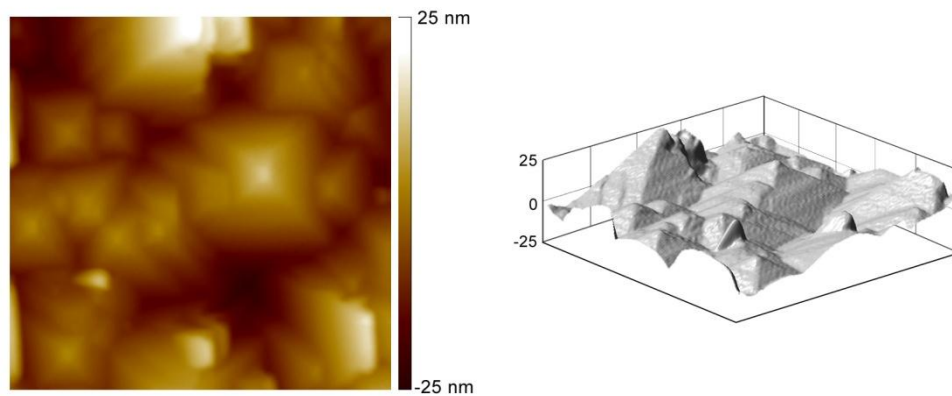


Figure 19. AFM (2D and 3D) of a MgO film grown in oxygen-rich conditions. The slower growth promotes the proper (100) orientation as exhibited by square-based pyramidal formations.

Optimal quality films, as mentioned previously, can only be obtained with proper sample pre-treatment, including degassing. Figure 20 shows AFM of a superior quality film with RMS roughness less than 7 Å. This film was grown under very similar conditions as that in Figure 19, but with the difference being that the substrate used in Figure 20 was degassed for 12 hours as compared to only 6 hours for the prior image.

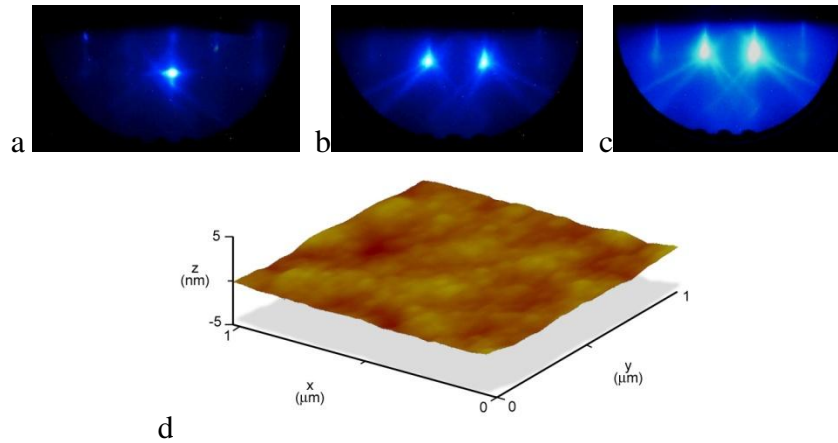


Figure 20. RHEED images of MgO film growth (a) prior to growth, (b) after 30 minutes of growth and (c) after one hour. Also, (d) AFM showing the high quality of the MgO film surface verifying the RHEED indications. Roughness of the film is less than 7 Å.

Growth Dynamics

Mg Pressure Effects

An important and interesting analysis was carried out to understand the effect of Mg K-Cell temperature on chamber pressure. The vapor pressure of magnesium is well characterized over the pertinent temperature range (as an exponential function of $1/T$) and so starting parameter ranges could be defined. The noteworthy aspect of this study is the dynamic observed when Mg is evaporated into the oxygen rich environment.

For oxide growth, literature holds that high quality films are typically grown in an oxygen-rich, and relatively high pressure (~ 10 μTorr) environment. A typical flow rate used in this series of growths was 2.5 sccm. This oxygen flow rate sets the chamber pressure maximum at a value of approximately 15 ± 2 μTorr , depending slightly on RF power. With increasing Magnesium cell temperature, and therefore increasing Mg flux, the chamber pressure actually decreases rather than increases, due to a process termed “gettering”. This reduction in pressure is attributed to the formation of MgO which has a much lower vapor pressure than elemental

Magnesium. As Mg flux into the chamber increases, increasing quantities of MgO are formed reducing the pressure to some minimum at which the $\text{Mg} + \text{O} \rightarrow \text{MgO}$ reaction is in dynamic equilibrium. Figure 21 illustrates this effect. The benefit of the phenomenon is that magnesium flux can be calibrated quite accurately from the chamber pressure without the need for additional measurements such as residual gas analysis (RGA). This is not the case for Ni, however.

Effect of Mg Aperture

In oxide growth, great care must be taken to reduce the oxidation of the metal source charge. Oxidation of metals such as Magnesium and Nickel can occur within the source crucible on the bulk metal itself and cause a reduction or unpredictability in the flux generated. One means of reducing this effect is to insert an aperture in the source crucible which purportedly reduces the in-flux of oxygen and helps preserve the source charge. This aperture also restricts the flux of the metal itself, however, and can be subject to a unique set of problems in which accumulation of source metal (and oxide) around the aperture causes erratic flux behavior. After working with various aperture sizes, the Mg aperture was finally abandoned and successful growth was achieved without the use of an aperture.

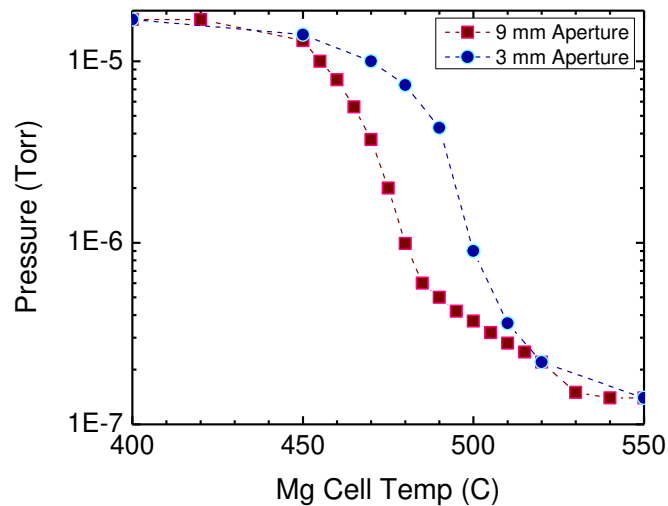


Figure 21. Growth chamber pressure at a function of Mg cell temperature. The two curves shown are for two different sized apertures, 3mm and 9 mm.

It should be noted that because the aperture restricts source flux, it greatly impacts the chamber pressure curve, as shown in Figure 21. The widening of the aperture from 3 mm to 9 mm essentially shifted the curve by approximately 20 °C, thereby reducing the cell temperature needed to maintain a specific flux. The pressure curve for open-crucible Mg evaporation is not shown but would simply constitute an additional shift to lower temperatures.

Ni_xMg_{1-x}O

Once MgO homoepitaxy had been optimized to a reasonable extent, the growth of Ni_xMg_{1-x}O films was then attempted. The ternary compound was the primary focus largely because of the tunable deep UV bandgaps that were presumed to be accessible by alloying NiO and MgO. While there was certainly evidence in literature to support the claim that the ternary bandgap is in fact tunable [48, 89], highly controlled bandgap engineering had not been demonstrated. This was perhaps related to – though separate from – the fact that no such films of very high quality and sufficiently refined concentration variations had been yet been epitaxially grown. Thus the question still remained whether such films could be grown at all and, if so, to what degree can the bandgap of the material be controlled? The overarching effort of the research presented in this section was therefore predominantly concerned with simply realizing films of varying concentration while simultaneously achieving the best epitaxial quality possible.

While this fundamental endeavor dictated the overall research direction, many challenging technical sub-tasks had to be overcome. In particular, there was very little information available to the author regarding the thermal evaporation of Nickel. Specific details about achieving and maintaining sufficient Ni flux in the particular MBE used presented many difficulties. At times, catastrophic equipment failure such as broken crucibles (the pyrolytic graphite, boron nitride or alumina crucibles held in the Knudsen cell) prompted changes in growth parameters that would not have otherwise been explored (such as lower Ni evaporation temperatures). Similarly, simply working in a monatomic-rich Oxygen plasma environment at high temperatures causes damage and degradation to the equipment and materials used and can

also force such course-altering parameter changes to be made. Therefore, examining the growth parameters of $\text{Ni}_x\text{Mg}_{1-x}\text{O}$ for optimal epitaxial quality also demands determining which growth parameters are tolerable to the system in use.

Within the aforementioned constrictions, the feasibility of certain aspects of the film growth had to be ascertained in preliminary stages of research before $\text{Ni}_x\text{Mg}_{1-x}\text{O}$ could be realized. It had to be proven, for example, that Nickel flux could be maintained at temperatures that the Knudsen cell and the crucible could tolerate. It had to be proven also that Nickel flux, if maintained, would in fact react with the Oxygen present at the film surface to nucleate a high quality Ni-containing film at all. The most direct way of addressing both of these inquiries was to attempt NiO film growth. Thus, while the initial general approach to $\text{Ni}_x\text{Mg}_{1-x}\text{O}$ growth was to introduce increasing Ni flux into the previously determined MgO growth parameters, NiO films needed to be attempted first.

NiO Film Growth and Characterization

Though growing pure binary NiO was a brief divergence from the approach of introducing Ni into MgO growth conditions, carrying out the initial NiO investigation was extremely important for several reasons, besides the simple confirmation of Ni flux. It was presumed to be important to define a lower range for the band gap energies expected and binary NiO constitutes this lower boundary. In addition, the successful growth of NiO would set an expectation of film quality that would be helpful in assessing relative quality of $\text{Ni}_x\text{Mg}_{1-x}\text{O}$ as well. But because optimization of NiO was not an initial goal of these early growth series, only a few growths of NiO films were carried out before attempting to then simply alloy Ni with MgO.

Optimization of NiO was not attempted with systematic series of growths. This is now thought to have been an erroneous approach, as will be discussed in more detail later. In brief, NiO should have been optimized and Mg then introduced, rather than the opposite. In spite of this misjudgment, these early metal-rich NiO films were realized nonetheless and yielded interesting semiconductor properties.

Cation-Rich Growth

Early NiO and $\text{Ni}_x\text{Mg}_{1-x}\text{O}$ films growths were essentially proof-of-concept endeavors. Both adequate Ni fluxes and surface nucleation remained to be demonstrated in the MBE system. Nickel itself presented challenges because of the high cell temperatures needed to achieve flux. This is attributed to the low vapor pressure characteristic of Ni which was known only qualitatively to the author. Although vapor pressure data for Ni does exist, actually calculating the flux reaching the sample surface (from a remotely located cell, with a specific amount of source material in a specific geometry, etc.) is prohibitively complex. Determining appropriate starting temperature ranges for the material was therefore only tractable experimentally.

In order to ascertain a starting point for the parameter of the Ni cell temperature, the experience gained from the growth of ZnO and MgO was applied to this new metal. Both of the other cations used, Zn and Mg, showed significant gettering, as discussed. This reduction in chamber pressure was assumed to be due to the formation of low vapor pressure compounds (ZnO, MgO) which adhere to chamber surfaces more readily than the separate reactants. It was assumed that introduction of Ni into the monatomic rich Oxygen environment would be characterized by the same reduction in pressure. Using this metric, in the early NiO growth

procedures the Ni cell temperature was increased to values above ~ 1400 °C in order to observe reduction in system pressure. After being applied to binary NiO growth, similar Ni cell temperature ranges were then used in $\text{Ni}_x\text{Mg}_{1-x}\text{O}$ films growths. Though it was not evident at the stage of initial binary growth, such Ni fluxes are relatively large and proved ultimately to be non-ideal growth conditions for promoting good optical response. These growths were nonetheless important predecessors to establishing the more successful oxygen-rich. The data on the films is presented for completeness and to emphasize the critical importance of such growth parameters and their impact on films quality.

NiO

NiO growth was carried out on both (100)-Si and (100)-MgO substrates. The evaporation temperatures initially explored were in the range 1300 – 1600 °C. While growths were executed with these parameters, the higher end of this range of cell temperatures proved to be damaging to the crucible. The primary cause of this is the melting and re-solidification of the Ni before and after growth, respectively.

Figure 22 shows AFM and spectral reflectometry for the highest quality NiO film (on Si (100)) grown. The roughness of the film is 34.8 nm and is likely polycrystalline. However, cubic artifacts of the (100) symmetry are seen in the AFM and it can be therefore concluded that the film maintained crystalline nature during the growth (and did not degenerate into amorphous phase). The spectral reflectometry curve reveals a reflectance magnitude that decreases from approximately 355 nm to 310 eV (3.5 – 4 eV). This is due to interband absorption and is in good agreement with such data found in literature.

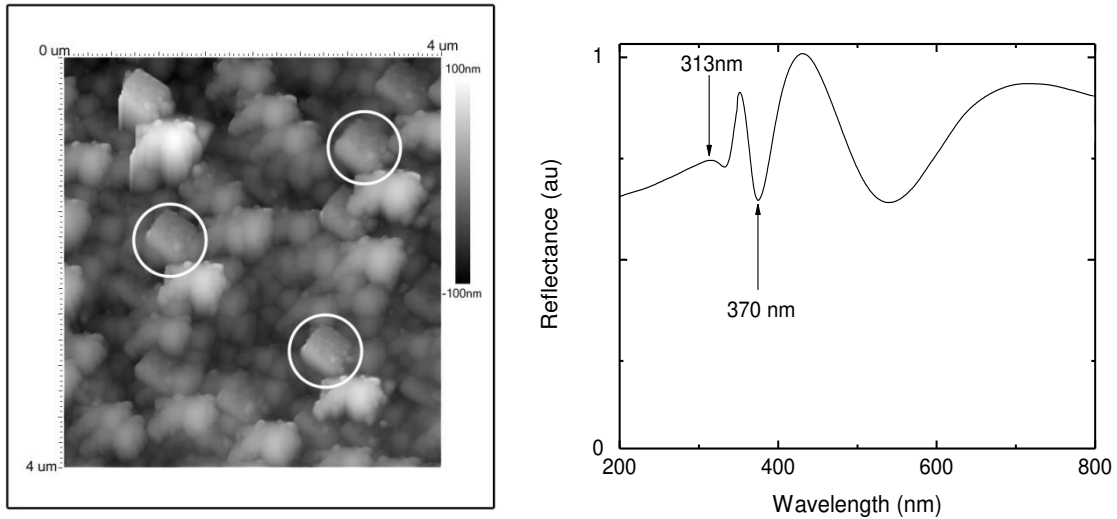


Figure 22. (a) AFM of a NiO thin film grown on Si (100) highlighting the cubic shaped (100) NiO crystal facets and (b) Spectral reflectance for NiO heteroepitaxial film

Similar data is presented in Figure 23 but for NiO on MgO. The AFM data shows indications of a cubic structure, though less well defined than in the case of NiO on Si. The roughness, however, is as low as 7.6 nm for the MgO-grown films. The transmission curve reveals a strong absorption increasing over approximately the same range as in the case of NiO on Si (about 3.65 to 4 eV).

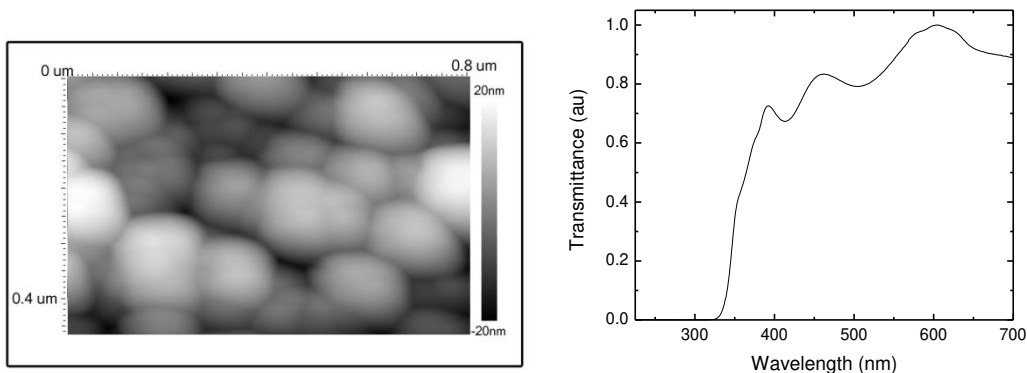


Figure 23. (a) AFM and (b) Spectral transmittance for a $\sim 1 \mu\text{m}$ thick NiO film on MgO

The NiO films thus exhibited good transparency over the visible spectrum and well-defined interband absorption. Because NiO itself was secondary to the overall goal of the research, time was not dedicated to producing highly-optimized films. However, because the films possessed such distinct optical properties, and because the band gap energy of NiO lends itself to solar-blind applications, a device investigation was conducted.

NiMgO

After NiO homoepitaxy had been demonstrated, the first attempts at Ni integration were attempted. These growths exploited basically the same parameter space used for the homoepitaxy (Mg cell temp, etc). In this way, Nickel cell temperatures ranging from 1250 – 1440 °C were explored for these growths. The maximum temperature was set, in part, as being just below the melting point of Ni which helps in prevention of the aforementioned crucible damage problem encountered. The investigation proceeded by gradually increasing Ni

temperatures, *ceteris paribus*, and observing the changes in film transmittance. Figure 24 shows typical results for these films.

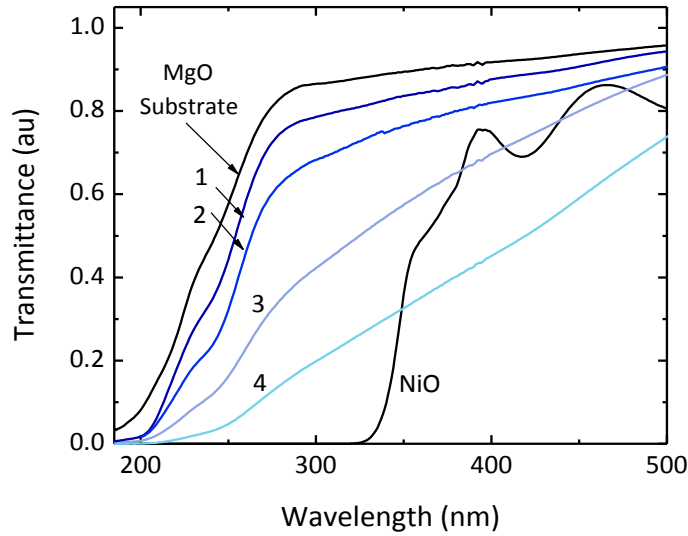


Figure 24. Typical transmittance curves for $\text{Ni}_x\text{Mg}_{1-x}\text{O}$ thin films grown under cation-rich conditions

Table 1. Growth parameters used for initial cation-rich NiMgO films growths.

Sample	O ₂ Flow (sccm)	RF Power (W)	T _{Ni} (°C)	T _{Mg} (°C)	Pressure (Torr)
1	2.65	350	1380	440	8.70E-06
2	2.5	350	1410	430	1.50E-05
3	2.5	350	1440	440	8.50E-06
4	1.6	350	1440	440	2.90E-06

At Ni cell temperatures below ~ 1350 °C (not shown), the transmission curves were not measurably altered. The initial assumption is that the Ni flux at those temperature was negligible compared to Mg flux and therefore integrated proportionately. This assumption may prove to be

faulty, as will be discussed. With increasing Ni temperature (above 1350 °C), there is a noticeable shift in the absorption edge (samples 1-4 in Figure 24). Note for this discussion that because the films presented are thin (<200 nm) that the transmitted intensity does not go to zero with the film absorption edge but is reduced by the film (thus the film is responsible for the drop in transmission seen at wavelengths longer than ~245 nm), then further reduced by the much thicker substrate. The shift in absorption edge is accompanied by significant broadening of the absorption. The broadening of absorption edge is attributed to crystal imperfections and is not desirable in device-quality films.

The probable cause of the absorption edge broadening is excess Nickel. This is illustrated in Figure 24 by samples 3 and 4. These samples were grown under identical conditions with the exception that oxygen flow was less for sample 4 (1.6 sccm as compared to 2.5 sccm). The resulting film (4) exhibits a less abrupt absorption edge which is only slightly shifted to longer wavelengths. This single comparison illustrates the importance of oxygen flow to crystal quality. Oxygen flow cannot trivially be increased beyond this value, however, as system pressure will become prohibitively high and not allow for pressure stability.

An additional factor to consider in attempting to optimize growth is the Magnesium flux. Because Mg and O have a greater difference in electronegativity than do Ni and O, it is expected that oxygen atoms will preferentially bind to Mg rather than Ni. This is further complicated by the fact that only one oxidation state of Mg exists (MgO) while there are at least 2 oxidation states for NiO (NiO and Ni₂O₃). Nickel therefore has a lower likelihood of participating in Ni-Mg-O bonding than does Mg. This will be reiterated in greater detail in the remainder of the document.

Oxygen-Rich Growth

Several factors prompted the use of lower Nickel fluxes to achieve better film quality. The most important among these was of course the apparent difficulty in shifting the bandgap of MgO to lower energies with increased Ni flux and the broadening of the films' absorption edges, as discussed. Furthermore, it was known from literature as well as limited experience, that oxygen rich growth is optimal for achieving good film morphology and general film quality in the case of ZnO. This reason alone may seem sufficient to prompt oxygen-rich investigation. However, it is well known that Ni has two oxidation states and can occur in the stable structure Ni₂O₃. There is therefore a propensity for NiO to contain excess oxygen, which is effectively a defect state in the material. Therefore, it is not a foregone conclusion that oxygen-rich conditions are inherently better for NiMgO growth.

In addition to these considerations, however, there were also significant experimental limitations associated with metal-rich conditions that made growth in that mode very challenging. In particular, the difficulties with evaporating Ni at temperatures greater than approximately 1400 °C caused serious hindrances to progress. The thermal expansion of the Nickel held in the crucible led to many breakages which in turn led to tremendous increases in the maintenance time of the MBE system. The melting point of Ni is 1453 °C and although the measured temperature of the Knudsen cell (as measured by an internal thermocouple) never reached that value after early growths, Nickel did in fact melt under the previously described conditions ($T_{Ni} < 1440$ °C). When re-solidifying, this Ni would expand at a rate apparently unequal to that of the crucible and cause catastrophic failure of the cell.

There were therefore multiple motivations for attempting to grow with a decreased Ni flux. However, as discussed, there was already insufficient shift in the NiMgO with increased Ni cell temperature. Therefore, the solution to be examined next necessitated not only a decrease in Ni flux, but also a decrease in Mg flux. Indeed, a different approach to Ni:Mg integration was needed altogether. The NiMgO film growth effort proceeded, therefore, by optimizing NiO with oxygen-rich conditions, rather than MgO.

NiO & NiMgO

The modified approach to the growth of NiO and NiMgO proved to be a superior method to achieving excellent epitaxial films, and it is based on important fundamental principles which have continued to be applicable in proceeding film growth endeavors since. In this re-visitation of NiMgO epitaxial growth, the author exploited the notion of ionicity, as applied to the two constituent binaries (NiO, MgO), to determine the parameter ranges to be examined.

The effective change in experimental approach due to the consideration of ionicity is subtle, however, the concept itself is not trivial and it has implications upon not only the growth conditions to be used, but also the structural and electronic properties of the material as well. The ionicity of a crystal is a quantification of the ionic character of the bonds between constituent atoms [104]. Classic definitions of ionicity (Linus and Pauling) are strictly functions of the electronegativities of the atoms. Modern variations of the definition are more complicated but still include these electronegativities as critical parameters. Ionicity is inherently related to reactivity as well and, in general, it can be expected that the constituent elements in compounds with greater ionicity will react more quickly dissipate more energy than those of compounds with

a lower value of ionicity. Therefore, by comparing the ionicities of the binaries, the favored reactions can be understood and the growth conditions tailored to account for them.

Among the two binaries of interest here, the ionicity of MgO is the greater and is also the greatest value among the three binaries MgO, NiO and ZnO. The details of how the values are calculated are not pertinent here, but the values themselves are presented for illustration of the need for a modified growth approach. The ionicity, f_i , of MgO is 0.841 while that of NiO is approximately 0.3. The implication in this is that Magnesium will react much more readily with Oxygen than will Nickel, *ceteris paribus*. A possible cause of the difficulties with Nickel integration that were observed is this propensity for Mg to preferentially consume monatomic Oxygen. If the growth conditions which were optimal for MgO growth were such that most (or approximately all) of the oxygen was consumed in reaction with Mg, then adding Ni flux would only decrease surface mobility for the Mg and O, while adding Nickel in a potentially non-stoichiometric proportion to oxygen. This decreased mobility is supported by the surface morphology measurements. Of course it is possible in that scenario that some Ni may integrate in intended substitutional ratio (ie the metal atoms make up 50% of the compound, by number concentration or molarity). The important, albeit simple, deduction derived from this is simply that there must be more than enough Oxygen atoms to accommodate the Mg, such that Ni has an increased opportunity to react. Additionally, with equal fluxes of Mg and Ni in the growth environment, the Mg will incorporate into the film at a greater rate than the Ni. Therefore, the modified approach taken to reach optimal oxygen rich conditions was optimize low-Ni flux NiO growth first, rather than MgO, and slowly increase Mg flux.

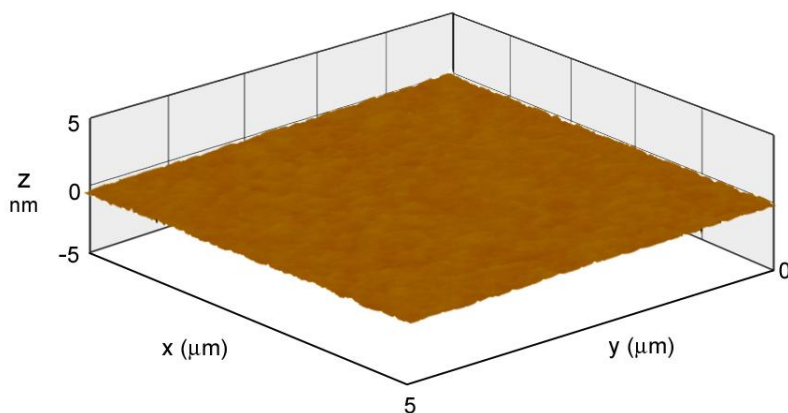


Figure 25. AFM scan of a NiO film grown in oxygen rich conditions with RMS roughness of 0.7 Å.

In this way, growth proceeded and evolved in this manner as it soon proved very successful for growth of the NiMgO films. The results are well represented by eight $\text{Ni}_x\text{Mg}_{1-x}\text{O}$ thin films ($x = 0$ to 1) which were grown after many iterations of parameter refinement. Films in this series were grown with O_2 flow rates ranging from 1 to 3 sccm, and RF power ranging from 150 W to 350 W. Growth of the films was carried out on single crystal MgO (100)-oriented 1 cm^2 substrates (MTI Crystal) at a fixed growth temperature of 300 °C. Prior to growth, substrates were cleaned in acetone, isopropanol and deionized water ultrasonic baths then dried with N_2 flow. Degassing of substrates was performed at 600 °C for three hours at pressures below $\sim 10^{-7}$ Torr in a separate, connected preparation chamber prior to growth. The growth time for all $\text{Ni}_x\text{Mg}_{1-x}\text{O}$ epilayers was fixed at 180 minutes. Six of the resulting films are shown in Figure 26.

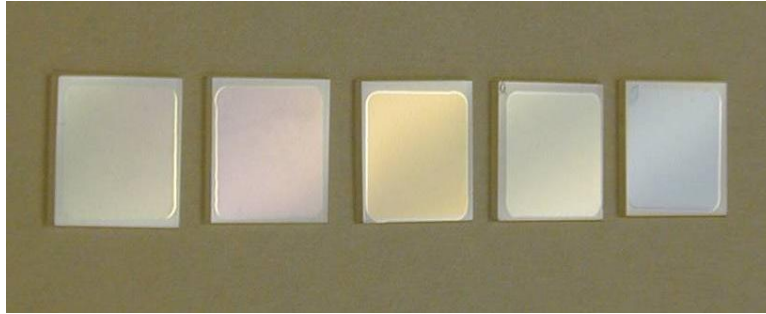


Figure 26. Five of the eight NiMgO films grown.

Morphology of all films was found to be of good quality with RMS roughness values as low as 0.7 \AA (for NiO), which generally increased with increasing Mg concentration to a maximum of approximately 120 \AA (for $x = 0.075$), as quantified by AFM. All films with $x \geq 0.25$ exhibited roughness of 2 \AA or less. RHEED patterns observed for all films were also indicative of good long range surface order and confirm the cubic structure. RHEED images ([110] azimuth) and corresponding AFM scans ($5 \times 5 \mu\text{m}^2$) are presented in Figure 27 for two representative films, $x = 1$ and $x = 0.32$, along with those of a MgO (100) substrate prior to growth. The RHEED pattern and AFM scan for the pre-growth substrate are shown in Figure 27 (a). While RHEED streaks are visible, they are neither notably well defined nor narrow. AFM showed substrate roughness to range from just below 2 to 10 \AA . In contrast, the RHEED pattern shown in Figure 27 (b) for the NiO film ($x=1$) consists of very narrow, bright streaks implying good long range surface order and a significant improvement over the initial substrate surface

quality. Figure 27 (c) exemplifies a more typical film surface quality. Films with Ni concentrations $x \leq 0.32$ also exhibited some cubic surface terracing as seen in Figure 27 (c).

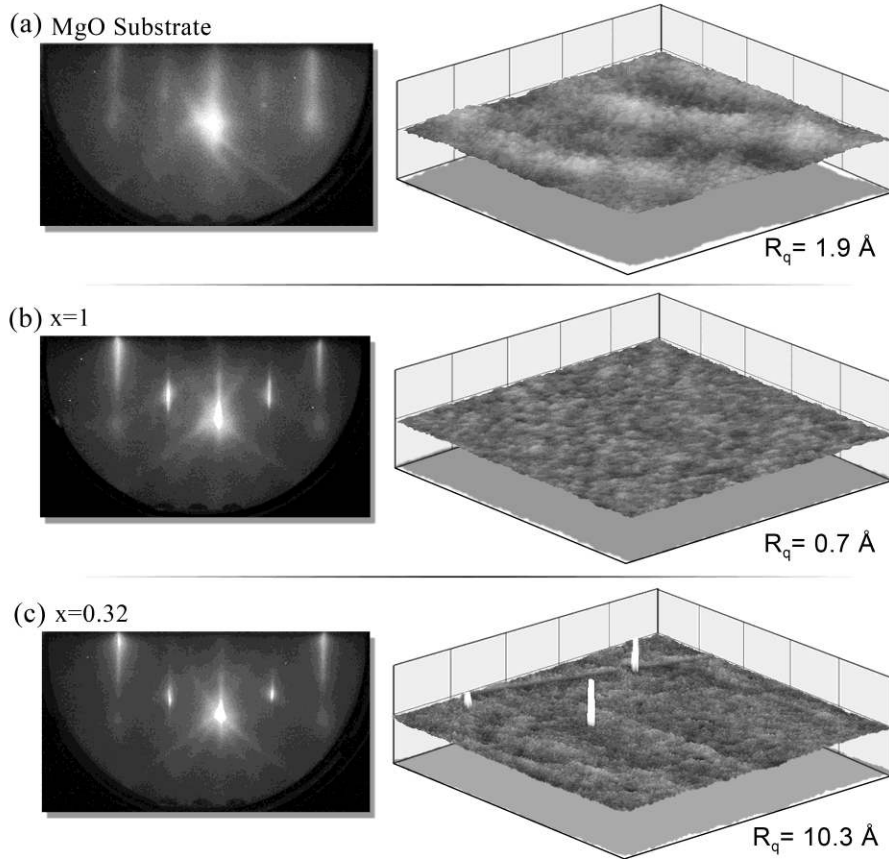


Figure 27. RHEED and AFM for two NiMgO films (b, c) shown with those of a virgin substrate for comparison.

X-ray diffraction illustrates the single-crystal cubic phase of the $\text{Ni}_x\text{Mg}_{1-x}\text{O}$ films. The only peaks observed for the films are attributed to the (002), (004) and (006) planes, among which the (002) was the strongest by approximately 2 orders of magnitude. Figure 28(a) shows XRD scans of the films over the region $35^\circ < 2\theta < 45^\circ$. The (111) diffraction peak is expected to be the second most intense peak for randomly oriented polycrystalline NiO and would be found

between $2\theta=36.939^\circ$ and 37.272° for these films. This peak is not observed in any of the spectra thereby demonstrating the highly oriented character of the films. It should be noted that a duplicate of the (002) peaks was observed in the spectra and is due to weak Cu-K_α radiation known to be emitted from the system. A closer examination of the $(002)_\alpha$ peaks shown in Figure 28 (b) reveals a broadening of the diffracted peak with increasing Nickel concentrations due to the overlap of film diffraction with sub-surface substrate diffraction. The resolution of the x-ray diffraction system does not permit differentiation of these peaks for most samples however the $x=1$ sample shows the emergence of a distinct NiO (002) peak. The overlapping (002) peaks are fitted to asymmetric double sigmoid functions to estimate the change in the films' lattice constant. Full-width half-maximum values of the films ranged from $2\theta=0.23^\circ$ to 0.33° . The results of the peak-fitting are shown in Figure 28 (c).

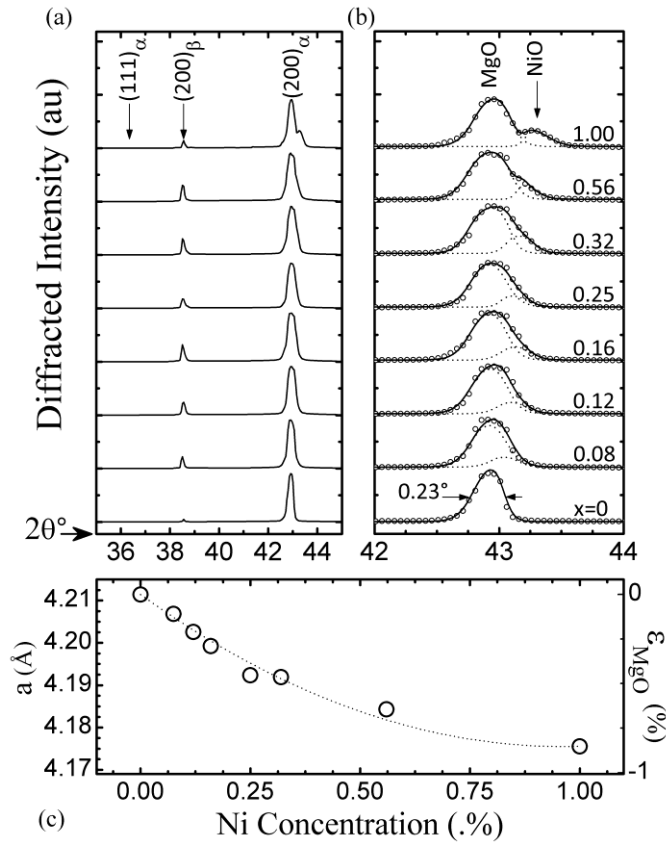


Figure 28. XRD results for the NiMgO thin films shown for the ranges $35^\circ < 2\theta < 45^\circ$ (a) and $42^\circ < 2\theta < 44^\circ$

To determine the material bandgap as a function of Ni concentration, both compositional and optical measurements were taken as described above. Figure 29(a) shows the RBS spectra of four the films for clarity. The spectral features associated with Ni, Mg, and O are indicated in the figure. Thicknesses and compositions were determined by spectra fitting with standard RBS analysis software. Films thickness ranged from 70 nm to 330 nm and Ni concentrations of the eight $\text{Ni}_x\text{Mg}_{1-x}\text{O}$ films (x) were determined to be 1, 0.56, 0.32, 0.25, 0.16, 0.12, 0.075 and 0.

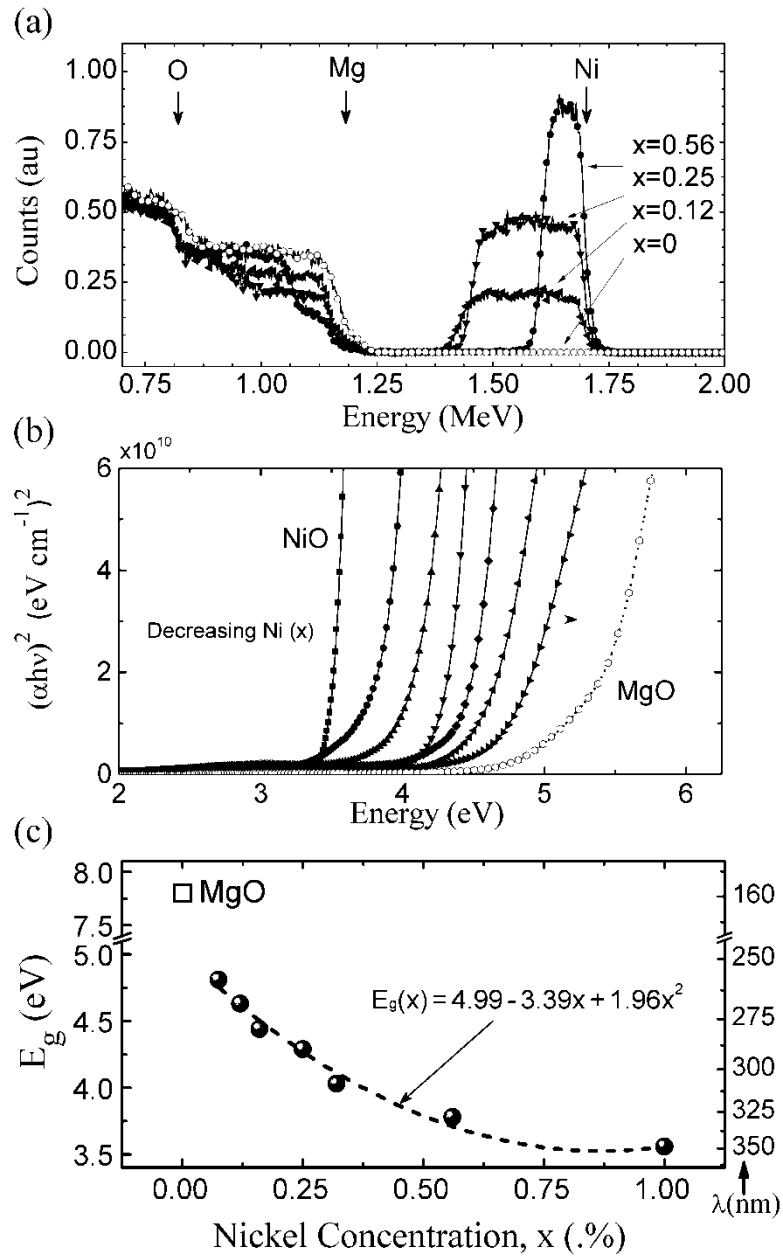


Figure 29. (a) RBS, (b) Absorption plotted as Tauc curves and (c) extracted bandgap versus Nickel concentration for all eight NiMgO films.

Film spectrophotometry measurements were used to derive film absorption and are plotted as $(\alpha h\nu)^2$ versus $h\nu$ in Figure 29 (b). The curves all exhibit a linear behavior above absorption edge, demonstrating the direct nature of the interband transition. A linear function

was fit to each $(\alpha h\nu)^2$ curve in Figure 29(b) over the range $1.5 \times 10^{10} < (\alpha h\nu)^2 < 5 \times 10^{10} \text{ (eV/cm)}^2$ and the optical bandgaps were determined by the energy-axis intercept. The values of the bandgaps (excluding $x=0$) were found to be 3.56, 3.78, 4.03, 4.29, 4.44, 4.63 and 4.81 eV, in order of decreasing Ni concentration. It is important to note that, while MgO appears to exhibit band-edge absorption around 5.0 eV, this absorption is well characterized and is attributed to the F and F^+ oxygen vacancies [105, 106], which occur closely spaced in energy. The accepted bandgap of MgO is 7.8 eV and is therefore outside the range of measurements possible with the spectrophotometer used. Though homoepitaxial MgO was grown ($x=0$), assessment of its bandgap is tenuous for this reason. Figure 29(c) plots the determined bandgaps of the $\text{Ni}_x\text{Mg}_{1-x}\text{O}$ films as a function of Ni concentration. Significant bowing is exhibited and there is an abrupt difference of approximately 3.0 eV between the bandgap of $\text{Ni}_{0.075}\text{Mg}_{0.925}\text{O}$ and the accepted bandgap of MgO. Vegard's law does not describe this relationship if MgO is included. Excluding MgO, the bandgap values are well described by $E_g = 4.99(1-x) + 3.56x - 1.96(1-x)x$ eV, as shown.

NiO & NiMgO Device Fabrication and Testing

With the encouraging degree of success experienced in the refinement of NiMgO film quality, qualifying the films for use in optoelectronic devices became central in the research effort. The films had already exhibited many essential characteristics that are sought in semiconductor thin films, such as good structural quality, good morphology and desired optical properties. However, initial assessment of the films in some functioning form was critical not only for confirmation (or refutation) of the hypothesis, but also to motivate the interest of external relevant parties.

The results presented in this section demonstrate the relevance and viability of this material as an optoelectronic material. Several distinct conclusions that are derived from the results of device testing should be emphasized. First, these devices unequivocally show deep-UV photoresponse. Second, the devices fabricated from NiMgO films are, with fair certainty, the first photoconductive devices made from lattice-matched growth of NiMgO by MBE. Thus they represent a novel and useful technological contribution. Finally, refinements in the photoconductive properties of this film, including the bandgap tunability demonstrated, have been made by examination and appropriate alteration of the growth parameters.

Several generations of devices were fabricated and tested as understanding of the device functionality grew. The first of these was simply a preliminary test of the early existing films, which were NiO, for absolutely any evidence of device photoresponse. At that juncture in the research it was not at all certain that these films eventually would show UV photoresponse, though such photodetection has been observed in NiO. For this reason, the first generation of devices from these films were fabricated using existing masks to preclude incursion of avoidable

mask production costs, if the tests were to have been unsuccessful. The MSM devices first tested were therefore not optimal, particularly in size. Also, at that time, readily available lasers (wavelength 325 nm and 635 nm) were used as the illumination sources to test photoresponse. These were also non-ideal for various reasons. Mainly, the 325 nm wavelength of the HeCd laser (3.81 eV) is only slightly greater energy than the bandgap value of NiO (~3.6 eV) and not sufficiently high power (maximum 35 mW) to excite strong photoresponse. However, these initial tests are important in that promising results *were* obtained and motivated the further investment of time and resources into the investigation. Such investments included the improved mask design and acquisition of high power, broadband UV and visible lamps.

The presentation of results focuses on a small number of the more significant successes with these devices. Discussion is also presented which specifies the significant findings on optimal growth condition for UV detection. While considerations such as type of metals used for contacts and electrode spacing are briefly discussed, these factors were of less importance whilst the predominant efforts were necessarily focused upon material growth. Also, NiO is differentiated from NiMgO for clarity of discussion and to indicate the sequence of progress; a comparison or contrast between the two is not an intention of the author. Rather, the NiO case should be considered as one that is very similar and a true subset of the ternary film. That this is not the case, however, for the counterpart ZnO/cubic-ZnMgO films.

NiO Initial Devices

The first instance of photoresponse demonstrated by the author among these cubic oxides was that of NiO. This first generation of NiO devices was fabricated from existing MSM masks, as mentioned, with the primary goal of simply determining if the photoresponse of the material

was measurable at all. This interrogation would be answered by testing with the HeCd ultraviolet laser (325 nm). A secondary goal was to determine if the photoresponse was spectrally selective, as is expected from spectrophotometry. This could be tested in part by use of the red diode laser (635 nm).

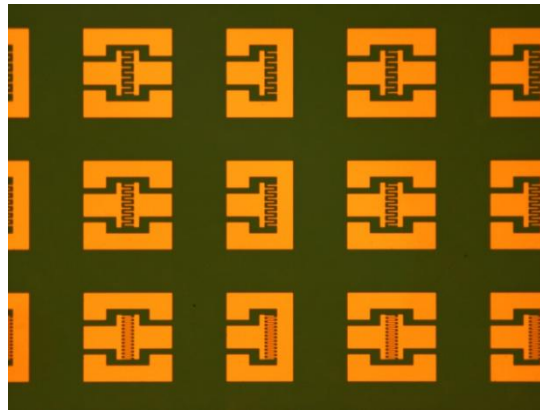


Figure 30. MSM Devices fabricated on NiO (on MgO).

MSM devices were fabricated on first-generation NiO grown on both on Si and on MgO substrates, as discussed. Electron beam evaporation was employed for the metals deposition. The contact metal used was Pt and contact thickness was 200 nm. Devices were annealed at 450 °C for 60 seconds. Fabricated devices are shown in Figure 30. The MSM design featured finger spacing that ranged from 3 – 10 μm .

The MSM devices were characterized through current-voltage (IV) measurements using a Keithley source-meter connected to a Signatone 1160 probe station. Devices were first measured without illumination to characterize dark current. Devices were then illuminated with 325 nm light from the He-Cd laser and, separately, 635 nm light from the diode laser. The optical power of both lasers was reduced to 4.8 ± 0.08 mW and was focused to a spot size approximately equal to the total device size (~ 200 μm). Figure 31 shows one such device under both 325 nm

illumination and 635 nm illumination. It should be noted that while the laser spot size is similar to the total device area, the active area of these devices is very small and occupies less than ~10% of the spot size area, as can be seen.

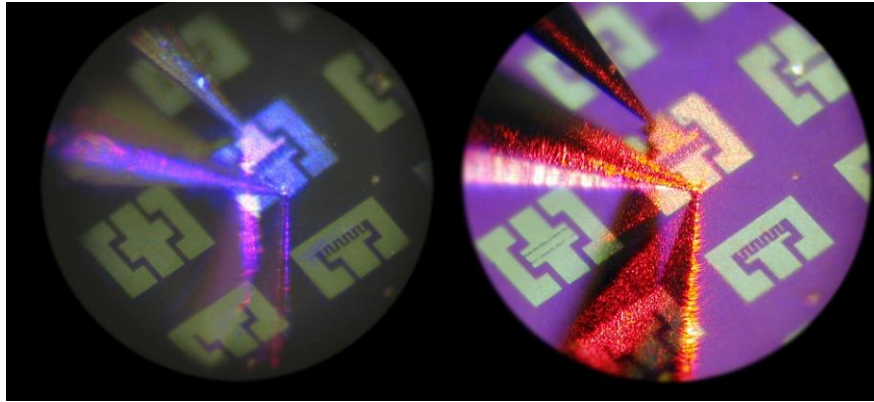


Figure 31. NiO MSM devices under (a) 325 nm illumination and (b) 635 nm illumination. Note that the blue appearance in (a) is not the laser light color itself (which is UV) but rather an artifact of luminescence from one of the optics used to redirect the laser light.

The IV characteristics and photoresponse of the MSM devices was very different for the two categories of films (Si-grown and MgO-grown). These differences are not likely due only to the substrates themselves, but also to other more critical growth parameters.

Figure 32 shows the IV characterization for a NiO MSM device on MgO. The strongly linear nature of the curve indicates that Ohmic contacts were formed by the processing. The figure shows three curves which correspond to the dark measurement (455.5 k Ω), the 635 nm illumination curve (455.0 k Ω) and the 325 nm illumination curve (211.6 k Ω).

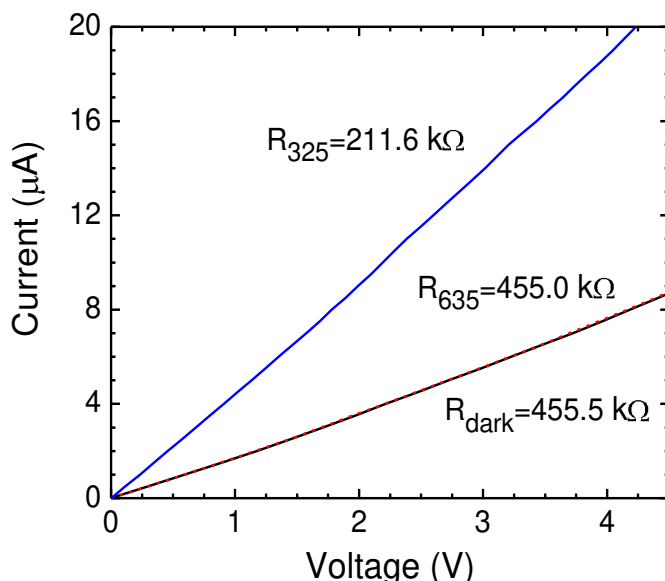


Figure 32. IV curves showing the photoresponse of a NiO-on-MgO MSM device to 325 and 635 nm light as compared to the device dark IV. The difference between the dark current and that under 635 nm illumination is almost indistinguishable on this scale.

Several factors are notable in the data shown. First, the curves show that the devices have relatively large dark current of $\sim 8 \mu\text{A}$ at 4 V bias. This low resistivity implies that there is probably a relatively high defect density which increases conductivity. Importantly however, the device exhibited a substantially stronger responsivity to 325 nm light ($\sim 1.77 \text{ mA/W}$ at 3 Volts) than to 635 nm light ($< 10 \mu\text{A/W}$ at 3 Volts). This UV:VIS rejection ratio of approximately 177:1 was the first quantified observation which strongly supported the notion that this material may be a promising candidate for visible-blind detection.

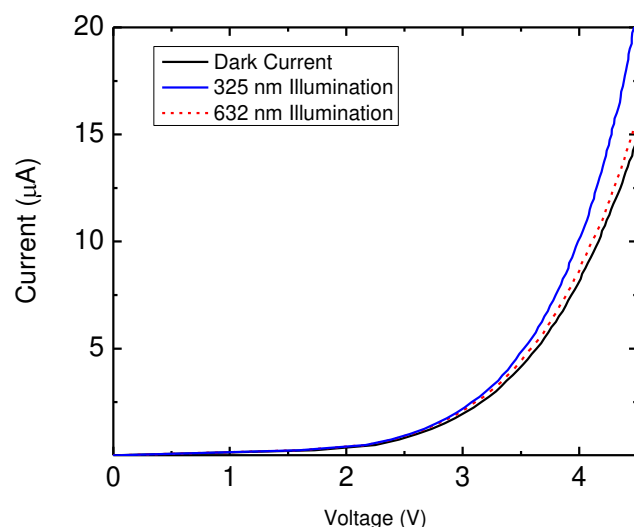


Figure 33. IV curves for a NiO MSM device on Si. While the differential responsivity is less substantial, these devices do exhibit strongly rectifying behavior.

Figure 33 shows the IV spectral characterization of a NiO MSM device on Si.

Interestingly, these devices showed strongly rectifying behavior as compared to those on MgO, despite identical fabrication and annealing procedure. The NiO on Si devices did show a stronger response to UV illumination than to 635 nm light, but not significantly so. Both of these differences can no doubt be attributed to the material growth procedure, but the exact source of the differences remains to be explored.

NiMgO Devices

Among the significant achievements in the research endeavor, that of the ternary NiMgO perhaps best punctuates the assertion that the effort has been successful. After significant refinement of the NiMgO thin films, as described, testing of the films as a photoconductive UV

optoelectronics could advance. Photoconductivity had been shown with NiO and thus it was presumed to be possible for NiMgO as well. However, it was not at all presumed that it would be observed for this material. In fact, because of the insulating nature of pure MgO, it was thought more likely that observation of photoresponse would be more challenging. Therefore, in order to better facilitate observation of such a response a more refined MSM design was necessary.

First, larger area devices would be needed if a broadband source - such as a Deuterium or Xenon lamp - were to be used as illumination. Larger area devices are helpful in this case because the minimum achievable spot size with such a lamp is significantly larger than for that of a laser. And in order to determine a true device spectral response, such a lamp would be required, as discussed. A series of MSM device patterns were therefore designed with lateral sizes of $100 \times 100 \mu\text{m}^2$ and varying electrode finger separation ranging from 1 to $15 \mu\text{m}$. The photomasks were designed with L-Edit and fabricated in house using the Leica EBPG5000+ electron beam lithography system. Though the mask met exact specifications, the smallest MSM devices patterned on the mask (spacing $< 3 \mu\text{m}$) could not be transferred into photoresist due to diffraction limitations of the exposure process. In one instance, however, the MSM devices were fabricated directly by electron beam lithography on the sample thereby achieving resolution of all feature sizes. This sample is shown in Figure 34 and therefore serves as an excellent representation of the mask pattern. Additional generations of devices were later designed and fabricated but consisted of almost identical device geometries but incorporated lateral sizes up to $300 \times 300 \mu\text{m}^2$.

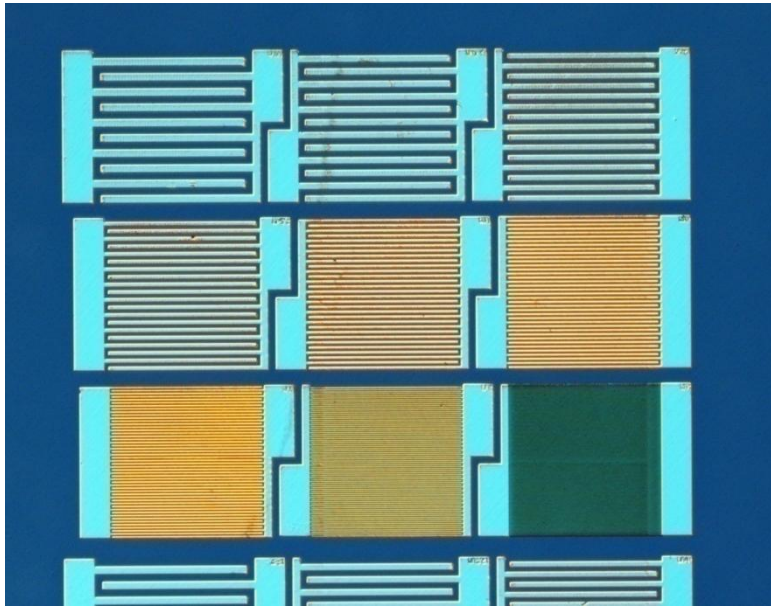


Figure 34. MSM devices fabricated from NiMgO thin film by electron beam lithography.

The earliest tests of NiMgO MSM devices yielded no results that indicated photoresponse of any kind. This was later determined to be several factors that included both experimental oversights as well as film characteristics that were not well understood. First, there was initially no existing UV response setup available to the author. Thus the experimental setup was continually modified as understanding of the films was gained. The spectral (or spectrotemporal) response setup was not initially equipped with the critical low $f/\#$ ($f/1$) sapphire UV lens at the sample position. Therefore, the spot size area was hundreds of times greater than that of the device making the photoresponse immeasurably low. Furthermore, the earliest films grown were of undesirable quality and would only exhibit the weakest, slowest UV photoresponse, if any at all.

Initial testing for photoresponse of the devices did not include any temporal element and consisted of measuring device IV curves with and without UV illumination. The first

observation of any photoresponse by NiMgO was seen in films grown by the aforementioned oxygen rich conditions. The particular film which exhibited the response was grown at the relatively low substrate temperature of 300 °C, with a Nickel cell temperature of 1325 °C, a Magnesium cell temperature of 345 °C and an oxygen flux rate of 2.5 sccm.

At that time, an interesting phenomenon was observed which was not understood or correctly interpreted by the author. It was seen that, when multiple alternating light and dark (illuminated and un-illuminated) IV curves were taken sequentially, they would initially show a measureable increase in current with UV exposure. This change in current would not be repeatedly reproducible, however, and the light and dark currents would converge towards the same value with increasing number of trials. This is exemplified in Figure 35. It was thought for some time that this was indicative of unusable device quality and represented a permanent degeneration. But with increased study of the phenomenon it eventually became clear the physical significance of this seemingly degenerate functionality and how to grow the films to reduce or eliminate this persistent photoconductivity.

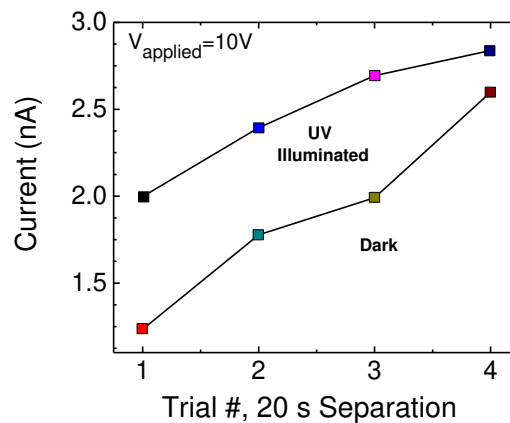
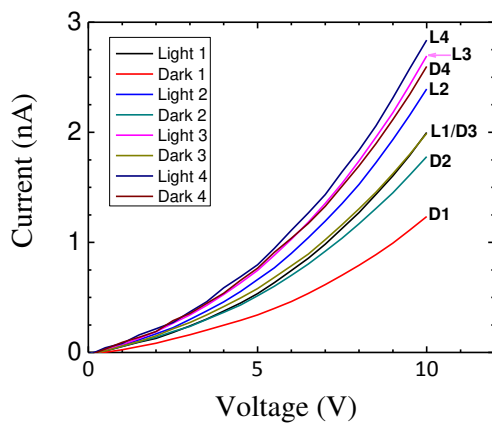


Figure 35. (left) Four sequentially acquired pairs of dark and light IV curves shown with the converging value of the device current at 10 V with increasing trial number (right).

Repeated observation of this IV behavior led to a study of the films in both the temporal and spectral domains simultaneously. This was facilitated by creating a LabView VI which incorporates continuous measurement of the device current in both dark and illuminated states (the temporal component) and spectral variation of the illumination wavelength. These are termed spectrotemporal measurements and can elucidate to some extent the conduction mechanisms and defects present in the films under study. With the implementation of spectrotemporal measurements, and with the inclusion of superior optical elements and experimental improvements, the photoresponse of the NiMgO films could be adequately assessed to show functionality as intended.

To advance the NiMgO films with parameter selection, the photoconductivity (and persistence thereof) was interpreted as an indicator of film quality. In general, the phenomenon of persistent photoconductivity in semiconductor is closely associated with shallow-level defects. There are many various mechanisms that may contribute as such and their exploration lies outside the scope of this discussion. However, one general principal which guided the changes in growth parameters was the conjecture that if the quality of the films was improved, it would promote films with not only a greater magnitude of response, but also films exhibiting faster photocurrent decay. This conjecture proved true and has continued to be a helpful hypothesis in the advancement of the films.

Earliest film growths of NiMgO were carried out at low temperatures (typically 300 °C) and with greater Nickel flux (Ni cell temperatures greater than 1400 °C), as previously described.

These films exhibited no observable photoresponse. The same parameter changes which led to the improvement of the films' morphological and optical properties also eventually led to observation of photoresponse from these same films. The key parameters which contribute strongly to the magnitude and temporal qualities of the photoresponse were found to be the metals: Oxygen ratio, as discussed, and also the substrate temperature.

The importance of substrate temperature is best illustrated by two films grown with identical Ni, Mg and O fluxes but with different substrate temperatures, 100 °C and 500 °C. These samples, shown in Figure 36, are initially in the dark state ($t < 10$ s), then illuminated with 290 nm light for 15 seconds ($10 \text{ s} < t < 25 \text{ s}$) and allowed to relax back to approximately the initial dark current. The impact on the photoresponse is obvious and noteworthy. First, the higher temperature sample exhibits a response that is more than an order of magnitude greater than that of the low temperature sample. Also immediately obvious is the difference in the temporal decay of the photocurrents between the two. The higher temperature sample apparently exhibits a very strong fast-response component (with a time constant on the order of 1 second) as well as a slower-response component (time constant ~ 20 s). The lower temperature sample (top) shows only an extremely weak fast response, and a very slow decay of photocurrent (time constant ~ 85 seconds).

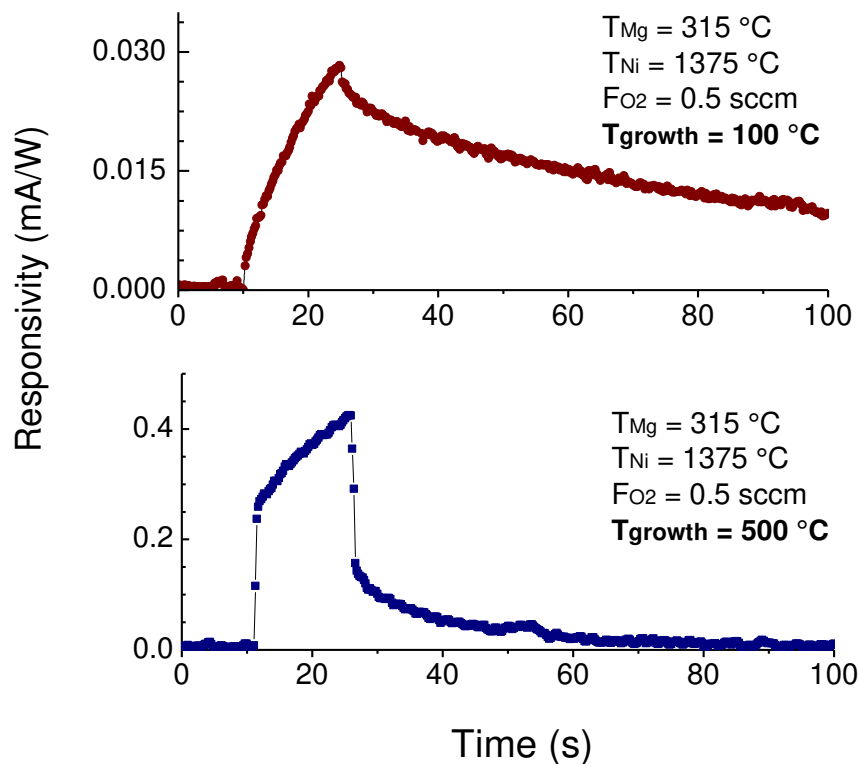


Figure 36. The temporal photoresponse two NiMgO films grown with identical Ni:O flux ratios. One film (top) was grown at a substrate temperature of 100 °C while the other (bottom) was grown at 500 °C.

As well as high-temperature growth, it also proved valuable to continue extending the notion of reducing the Ni:O ratio to improve photoresponse. One of the highest quality NiMgO films grown showed tremendous improvement over the aforementioned samples. Figure 37 illustrates the improved response of this film. For this sample, not only was the growth temperature further increased to 700 °C, but also the Ni cell temperature was reduced to 1350 °C and the oxygen flow rate increased to 0.65 sccm. The sample shows a tremendous increase in peak responsivity (~11 mA/W) over the others and exhibited a slow-response photocurrent decay time of only 8 seconds. While such a persistent photoconductivity is not desirable in general,

these improvements show that this phenomenon might be further reduced or eventually eliminated with appropriate growth parameters and techniques.

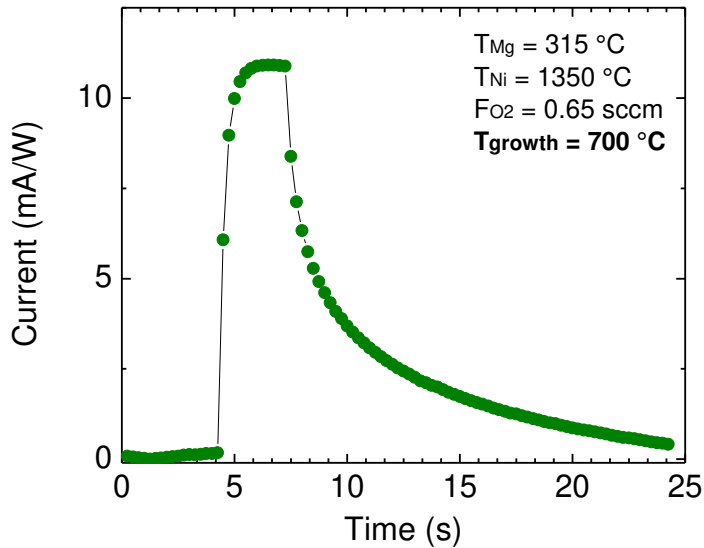


Figure 37. The temporal response of a high quality NiMgO film exposed to 290 nm light for 2.5 seconds.

Examining both the spectral response and the temporal response of these devices concurrently provides the best insight as to their functionality. Figure 38 shows a three dimensional graph of the complete spectrotemporal data set for a particular MSM sample (5 μm finger spacing, 10 V applied voltage). By analyzing such a data set, not only can the quality of device response be quantified (magnitude and temporal characteristics) but also the effective spectral response of the device. Such spectral characterization is crucial for determination of applicability of these films.

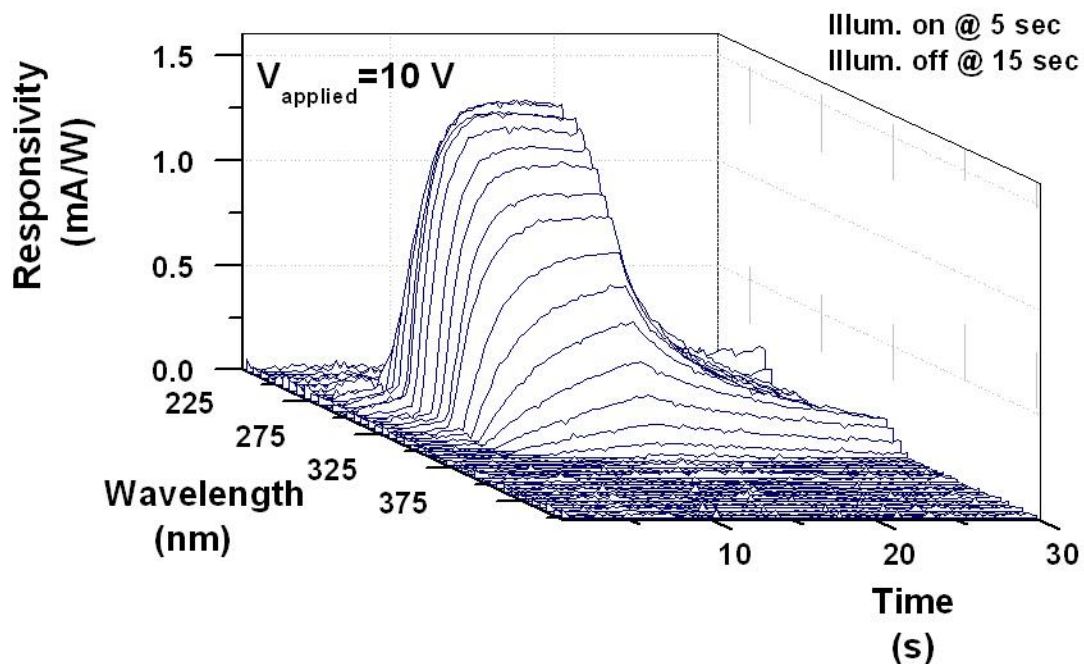


Figure 38. Spectrotemporal response of NiMgO MSM device.

By taking a spectral cross section of the full data set shown in Figure 38, the device spectral response is easily obtained. The spectral response of the MSM in Figure 38 is shown in Figure 39, along with that of a similar film grown with identical parameters, aside from a different Mg cell temperature (and therefore Mg concentration). The sample with a greater Ni concentration (estimated $x = 0.9$) shows a 1 dB cutoff wavelength of approximately 320 nm. The sample with lower Ni concentration (est. $x = 0.75$) exhibits a shorter cutoff wavelength around 295 nm. This simple graph, in some ways, best represents the entire culmination of the research efforts in NiMgO by the author thus far in that it shows not only a tremendous

advancement in the material from the time of inception, but also the usefulness of the ternary compound in its applications to deep UV technologies.

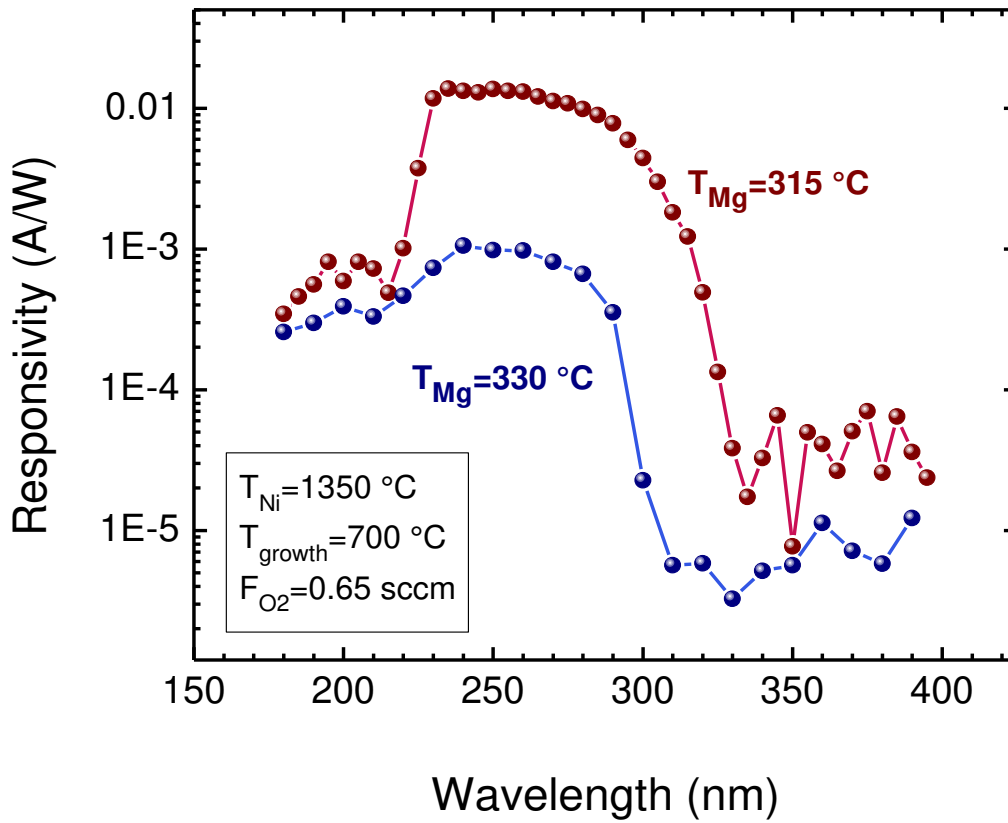


Figure 39. Spectral response of two similar NiMgO films, grown only with different Mg fluxes. The shift in device response edge demonstrates the tunability of the films' bandgap.

ZnO and ZnMgO

ZnO Film Growth & Characterization

ZnO films were actually the first oxide films grown in the research efforts. They were chosen in large part because approximate growth parameters had already been established for ZnO and were available from existing, publicized research. At that point in the endeavor, the goals were largely focused on establishing the functionality of the MBE system, which was untested at that time. Binary ZnO itself is somewhat peripheral to the broader goals of realizing cubic oxide materials and devices as it is wurtzite (B4) structure. As such, only a small number of ZnO films were grown on c-plane sapphire. Film growth was characterized in-situ with laser reflectometry only as RHEED was not yet functioning at that time. The significant progress made in this effort was not in the quality of the films so much as simply the realization of epitaxial films for the first time. However, reasonable quality films were produced with RMS roughness as low as 3.16 nm. Also, temperature parameters for ZnO were approximately established and were used for the future and more relevant work of growing the ternary compound, $Zn_xMg_{1-x}O$. Ex situ, the ZnO films were also characterized morphologically and optically.

Figure 40a shows in-situ reflectometry of a ZnO film growth session. The consistent magnitude of the reflectance oscillations indicates persistence in film quality throughout the growth session which lasted just over seven hours. The change in oscillation frequency is a result in changing the temperature of the Zinc Knudsen cell, which in turn changes the growth rate. Figure 40b shows the growth rates derived from the reflectometry in part a. The growth

rate does appear to saturate, as seen in MgO growth (Figure 16). The saturation appears less dramatic in this case because the temperature range of the K-cell here is narrower. This temperature range was initially conjectured for ideal ZnO growth by an experience colleague. It should be noted here that there was an aperture in the Zn crucible during these growths, which restricted flux as compared to the open-crucible growths.

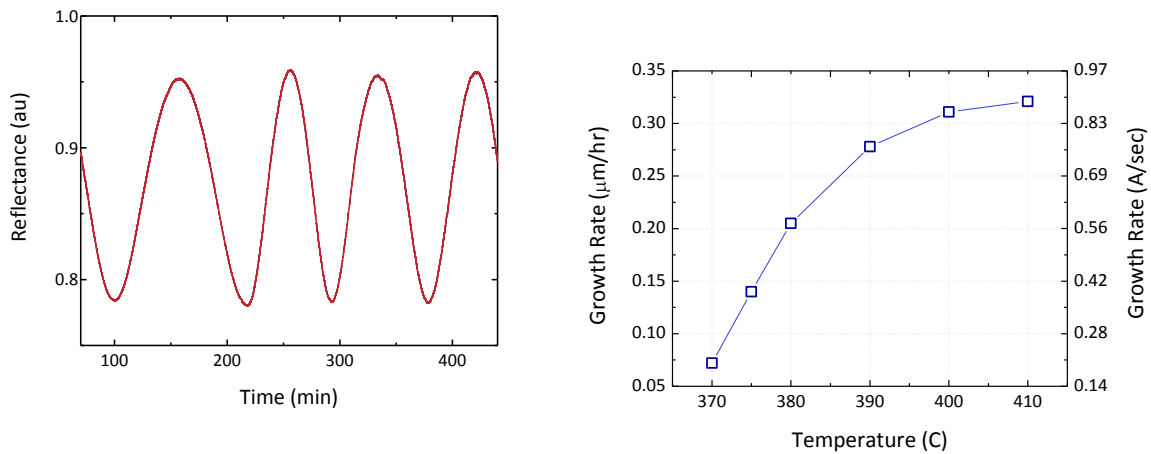


Figure 40. a) Reflectance oscillations from a ZnO epitaxial film growth. b) Growth rates derived from the growth in a) and one other growth session.

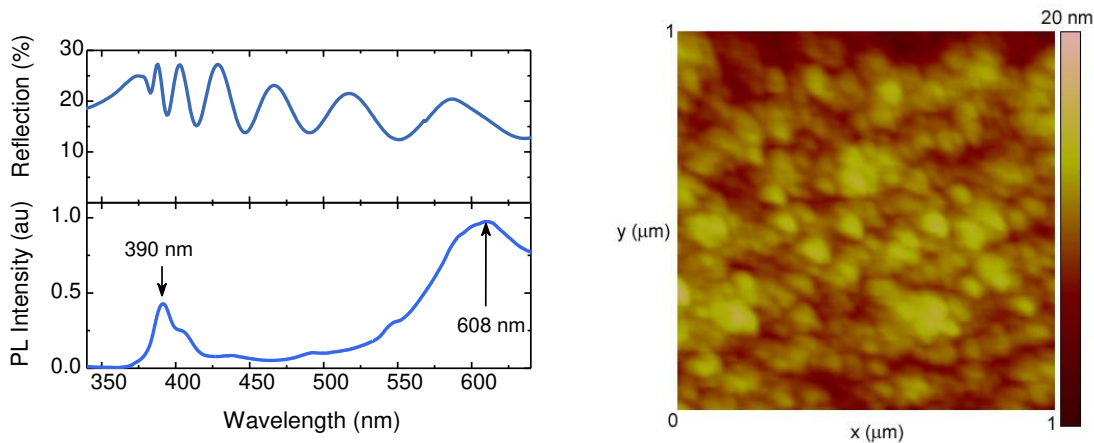


Figure 41. (Left top) Spectral reflection and (left bottom) photoluminescence of ZnO on c-plane Al₂O₃. (Right) AFM scan of ZnO thin film exhibiting 3.16 nm RMS roughness.

The ZnO films grown were also characterized optically and morphologically.

Transmission measurements, photoluminescence and AFM measurements were all carried out on the ZnO films and are shown in Figure 41. The optical measurements indicated an optical transition around 390 nm (3.18 eV), a slightly lower energy than the accepted value for the band gap of ZnO (3.37 eV). There was also a transition indicated by photoluminescence around 600 nm (2.07 eV). This was observed in the CdZnO films, as discussed, and is sometimes termed the “red band” luminescence. AFM measurements indicate relatively smooth surface and weak evidence of triangular (hexagonal) symmetry. Note that virtually no time was spent on improving the quality of ZnO since it was peripheral to the cubic oxide research of interest; it was merely a proof of capability.

ZnMgO Film Growth and Characterization

The $\text{Zn}_x\text{Mg}_{1-x}\text{O}$ films were studied sequentially after the $\text{Ni}_x\text{Mg}_{1-x}\text{O}$ and therefore benefited from experience and understanding gained earlier in the research. Additionally, a relatively narrow range of growth parameters had already been established for both of the binary films (MgO and ZnO) which gave a favorable starting parameter space for the crystal growth. The ZnMgO films have exhibited excellent morphological and optical quality and, while some improvement can no doubt be yet gained, they are ready for additional interrogations. Further, because of their quality, the ZnMgO films have already been exploited by the author in simple thin film structures, as a proof-of-capability endeavor.

The approach for the growth of the ZnMgO films was straightforward. Since existing temperature parameters had been established for both Zn and Mg evaporation, these served as a starting point. Also, an optimal range of system pressures had been established for both binary oxides. Further simplifying the circumstances is the fact that Zn and Mg both exhibit very similar gettering in the oxygen environment. An approximate system pressure of 5 -15 μTorr was observed to be largely optimal for both of the relevant binary compounds. The higher end of this range represents oxygen rich conditions, which have tended to exhibit better morphology. Both Zn and Mg cell temperature were investigated over the approximate range of 320 – 450 °C. For the first full growth series of ZnMgO, the Zn cell temperature was set at 355 °C, a temperature which set the system maximum pressure to approximately 10 μTorr , with no Mg flux. The Magnesium flux was set complementarily to further reduce the pressure to 5 μTorr ., approximately 400 °C. Successive growth sessions were carried out in which the Mg cell temperature was reduced incrementally by 10 °C. Initial growth sessions showed almost no

evidence of Zn integration. This is evidence of the preferential reaction of Mg with O over that of Zn with Oxygen, as discussed in greater depth later. As the Mg cell temperature was decreased, thereby decreasing Mg flux, a shift in the absorption edge was observed when $T_{\text{Mg}} \leq 380$ °C.

Further pursuit of this effort resulted in excellent quality cubic ZnMgO which is best exemplified by six films which demonstrate excellent quality as well as the desired bandgap tunability.

Figure 42 shows the RBS spectra for the six films in the order of increasing Zn, with the lowest Zn concentration (MgO homoepitaxial film) at the bottom. The highest energy peaks (~1.77 MeV) in the data are indicative of the film Zn content and the higher energy step (~1.17 MeV) represents Mg film content. The next step, with varying energy (~0.9 – 1.07 MeV), is the subsurface Mg step and the lowest energy step is oxygen (~0.85 MeV). Fits of the spectra showed the Zn content (x) of the thin films to be 0, 0.12, 0.33, 0.44, 0.58 and 0.65. Element profiles indicate good overall uniformity in composition throughout the films.

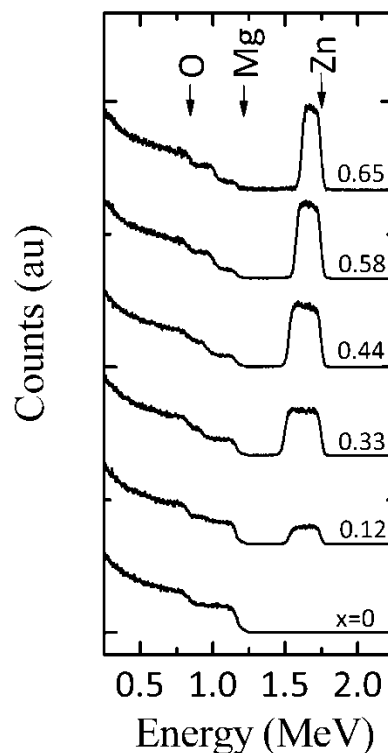


Figure 42. Rutherford Backscattering spectra for the six films grown. The highest energy peak indicates the Zn concentration which increases from $x = 0$ to $x = 0.65$, from bottom to top.

XRD measurement data are presented in Figure 43, also in the order of increasing Zn content, low to high. The domain of the graph is subdivided into two regions ($30^\circ < 2\theta < 42.5^\circ$ and $41.5^\circ < 2\theta < 44.5^\circ$) to best show relevant detail. Note that the intensity in the left pane is magnified by a factor of 400 relative to that in the right pane. The most intense peak observed in all of the films is located at $2\theta = 42.915^\circ$ and yields a lattice spacing of 4.2113 \AA (full-width half-maximum $\Delta 2\theta = 0.25^\circ$). This is the cubic MgO (002) peak which is present in all the spectra because of substrate diffraction and is not sharply distinguishable from ZnMgO film diffraction for all cases $x \leq 0.33$. For samples $x = 0.12$ and 0.33 , therefore, the peak locations due to the films themselves are subject to greater error. The cubic ZnMgO (002) peaks for $x =$

0.44, 0.58 and 0.65 are clearly distinguishable and allow for good assessment of film lattice constants.

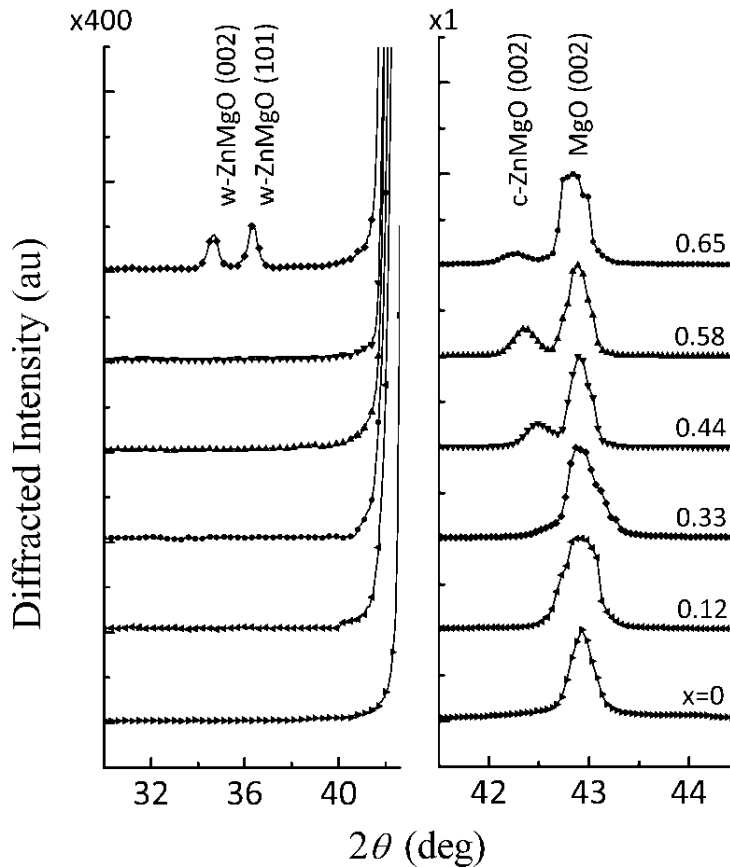


Figure 43. X-ray diffraction spectra of the $Zn_xMg_{1-x}O$ thin films in the angular range $30^\circ < 2\theta < 42.5^\circ$ (left pane) and $41.5^\circ < 2\theta < 44.5^\circ$ (right pane).

The left plane of Figure 43 spans across the angular coordinate of wurtzite structure $ZnMgO$ (002) and (101) diffraction peaks. All but one of the spectra are free of any discernable features here and these films are therefore strictly cubic phase in structure. The film with greatest Zn integration, $x = 0.65$, shows both the wurtzite (002) and (101) diffraction peaks, in addition to the cubic (002) peaks (right pane). The intensity of the cubic (002) peak is

approximately 200 times greater than that of the wurtzite (002) peak suggesting that, while phase segregation occurs for this concentration, it is still predominately cubic in structure.

Figure 44 shows the ZnMgO a-lattice constants for the films plotted against Zn concentration, as derived from the XRD spectra. To calculate the lattice constants, the asymmetric pseudo-Voigt function was fit to the peaks using standard non-linear curve fit analysis software. The lattice constants are shown to be approximately linear as a function of Zn content, ranging from 4.212 Å to 4.275 Å over the compositional range studied, suggesting reasonable lattice matching without relaxation of the films. The derived lattice constants are shown overlaid with those previously published for comparison [76, 107-111].

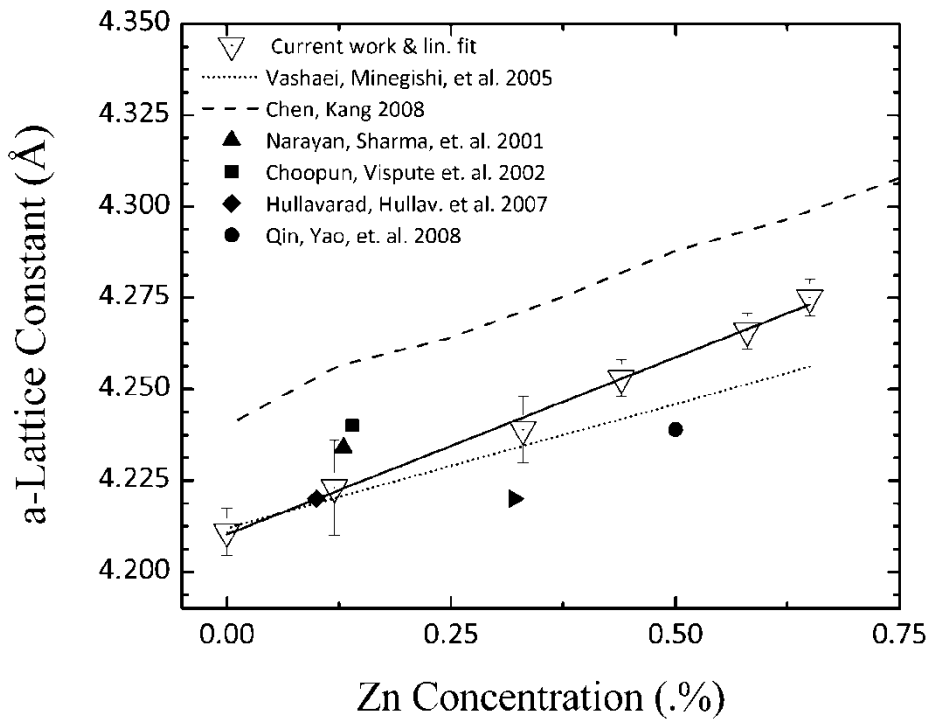


Figure 44. ZnMgO film lattice constants, as derived from the cubic (002). Values are found to be in good agreement with those reported in literature.

AFM measurements of the films revealed good overall morphology of the strictly cubic phase films with RMS roughness (R_q) ranging between 10 and 20 Å, taken over $4 \mu\text{m}^2$ scan regions. These samples also exhibited distinctly cubic morphology as evidenced by AFM. In Figure 45(a), a $5 \times 5 \mu\text{m}^2$ scan of the $x = 0.33$ films exemplifies this cubic structure. The film surface is highly ordered and suggestive of (100) orientation. The good long range order of the cubic films was also indicated by streaky, well-defined RHEED patterns, as shown in Figure 45(b). In general, the quality of RHEED patterns of all cubic films was improved over that of the substrate. Figure 45(c) is a $5 \times 5 \mu\text{m}^2$ AFM scan of the phase segregated sample, $x = 0.65$. As apparent in the image, the surface does not exhibit the same cubic symmetry as the lower Zn concentration samples, and no RHEED pattern for this film could be resolved. The roughness of the film was found to be more than an order of magnitude greater than those which are entirely cubic ($R_q = 444 \text{ Å}$ over a $4 \mu\text{m}^2$ region). For comparison, the roughness, as determined by AFM, of all films is presented graphically in Figure 46. It is evident that the higher Zn integration results not only in structural phase segregation, but also in a significant reduction in surface order.

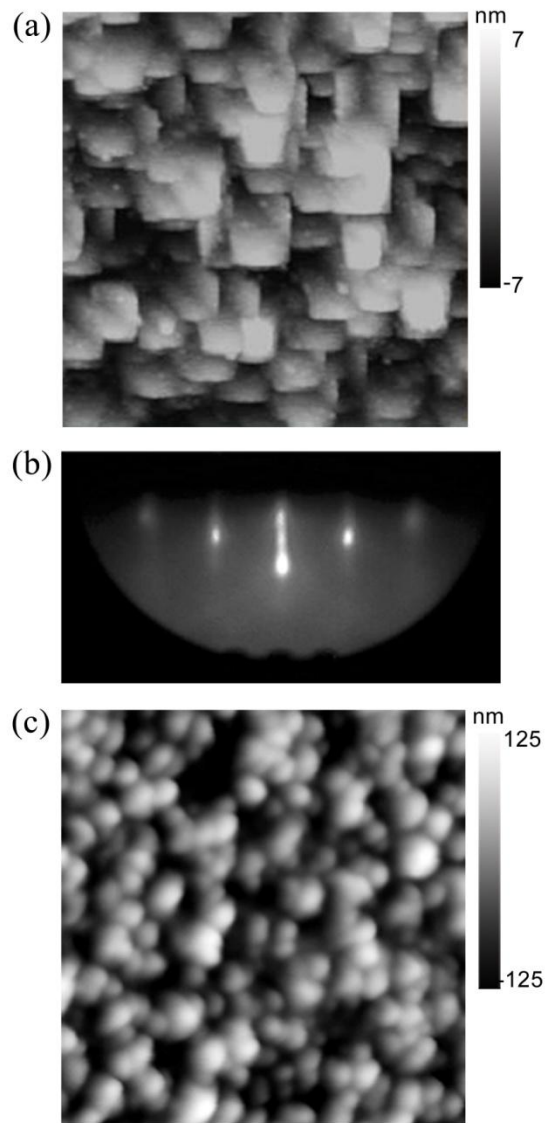


Figure 45. (a) $5 \times 5 \mu\text{m}^2$ AFM image of the $x = 0.33$ film. (b) RHEED image of the $x = 0.33$ sample (c) $5 \times 5 \mu\text{m}^2$ AFM image of the $x = 0.65$ film

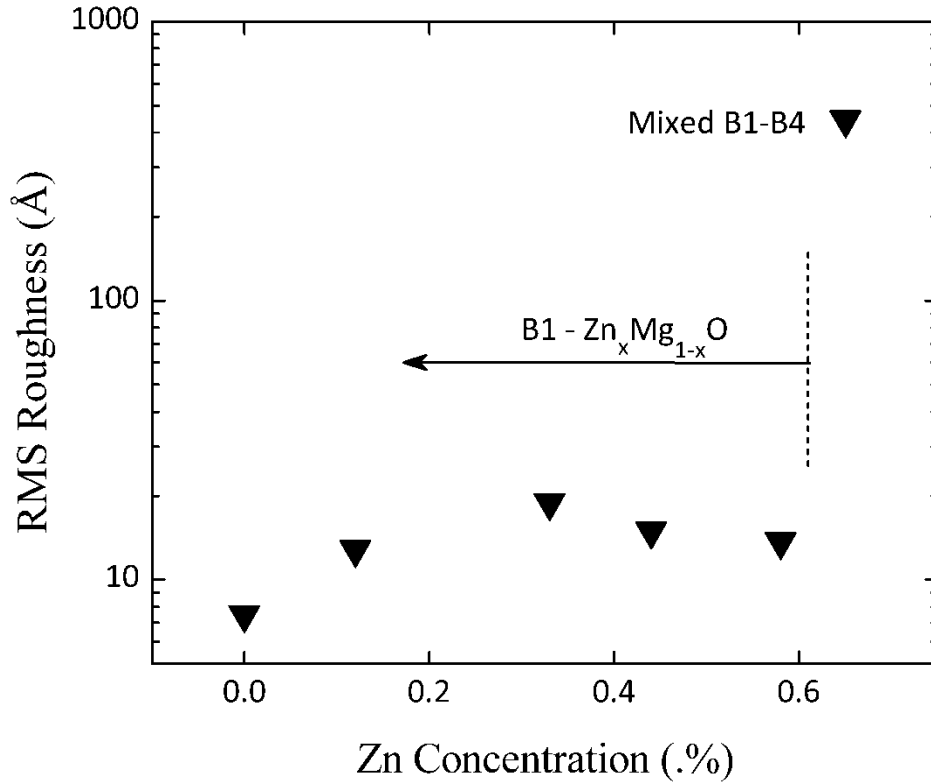


Figure 46. RMS roughness of the six films, as measured over a $2 \times 2 \mu\text{m}^2$ region.

The results of the transmission measurements are shown in Figure 47 and the associated Tauc plots derived from transmission measurements – $(\alpha h\nu)^2$ versus photon energy, $h\nu$ – are shown in Figure 48. The five cubic structure films exhibit abrupt absorption edges and good transparency throughout the visible spectrum ($T > 70\%$), including the modulating effects of interference. The linearity of the Tauc plots in Figure 48 demonstrates the direct nature of the optical transition. As expected, the absorption edge shifts to lower energies with increased Zn concentration. Interestingly, the phase segregated sample ($x = 0.65$) shows two distinct absorption features. The higher energy of these two features is expected to be due to cubic phase

regions of the sample, while the lower energy feature is attributed to the wurtzite component of the film. As is common practice, by fitting the approximately linear regions of the Tauc plots ($3.5 \cdot 10^{12} < (\alpha h\nu)^2 < 1.5 \cdot 10^{13} \text{ eV}^2/\text{cm}^2$) and finding the energy-axis intercepts, the bandgaps of the six films were determined (using the higher energy feature as the nominal bandgap value of the phase segregated sample).

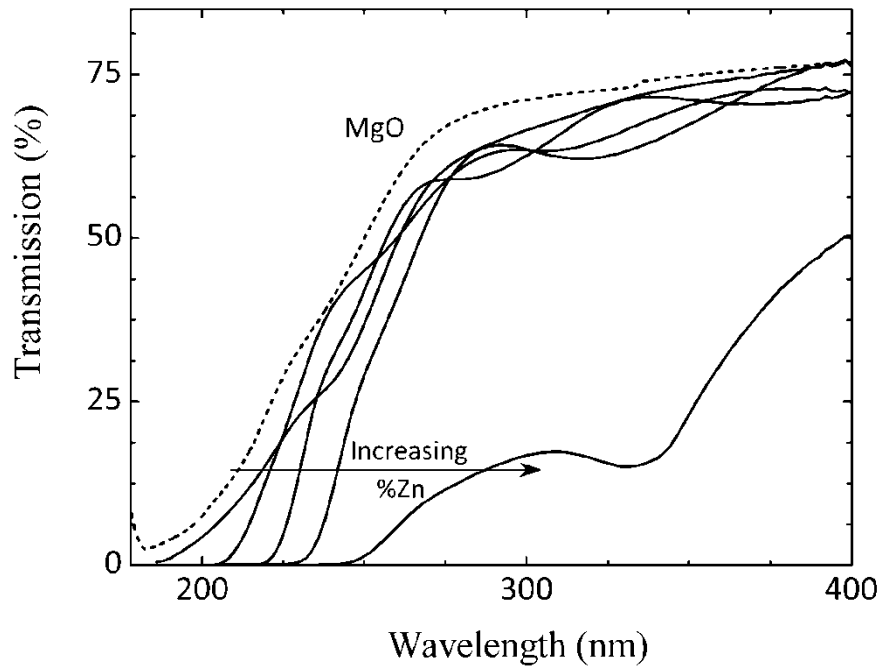


Figure 47. Transmission of the ZnMgO films, as determined by UV-VIS spectrophotometry.

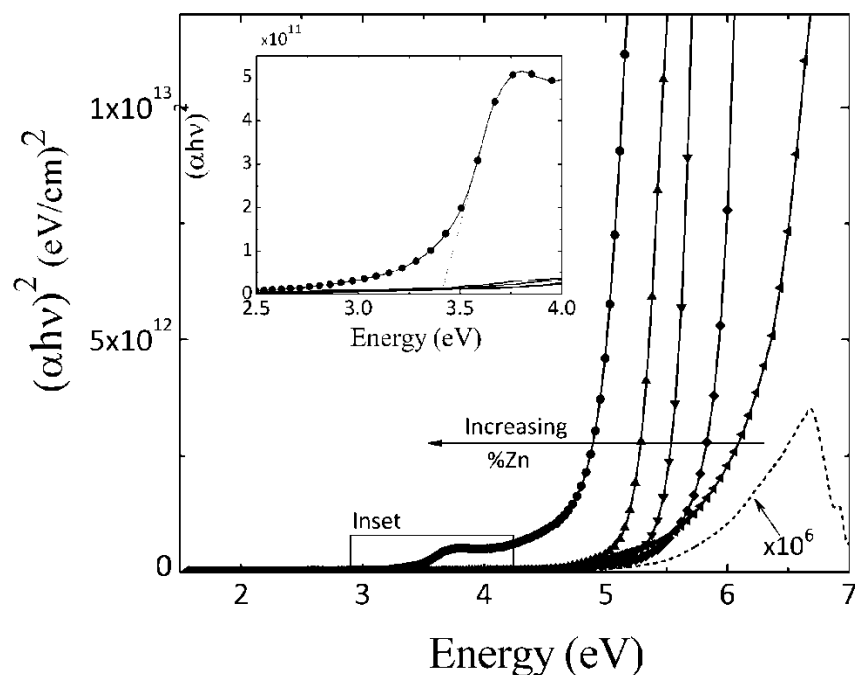


Figure 48. Optical absorption of the ZnMgO films, as derived from transmission measurements.

The bandgaps of the strictly cubic ZnMgO films were found to shift from the maximum value of 6.25 eV for $x = 0.12$ to a minimum value of 5.23 eV for the $x = 0.58$ film, with an approximately linear relationship as a function of Zn concentration. The high energy (B1) absorption feature of the $x = 0.65$ has its extrapolated energy axis intercept at 4.85 eV which also corresponds well with the linear behavior of the cubic films. The low energy absorption feature of this film is linearly extrapolated to approximately 3.40 eV, as shown in the inset of Figure 48. It is significant to note that this may be an indication that the wurtzite phase regions of the film are in fact very low in Mg content, even approaching pure ZnO. Further analysis with transmission electron microscopy (TEM) is necessary in order to better characterize the structure and its phases.

The optical absorption of the homoepitaxial MgO film is also shown in Figure 48 and it is multiplied by 10^6 to be visible on the same vertical scale. It is important to discuss the absorption feature present here. The apparatus used to carry out transmission measurements cannot measure energies greater than 7.08 eV ($\lambda < 175$ nm) and therefore cannot assess the band edge absorption at ~ 7.8 eV. However, there is clearly absorption which, if fitted linearly, has its intercept at approximately 5.75 eV. This absorption may be attributed to the F and $F+$ oxygen vacancies, and related defects, which are closely spaced in energy, located around 5 eV [106, 112, 113]. These transitions are direct and therefore contribute to a linear region in the $\alpha h\nu^2(h\nu)$ plot, as do the band edge transitions. Though these are significantly weaker (~ 100 cm⁻¹, per our measurements), the transmitted light is attenuated to a few percent of its incident intensity due to the relatively thick substrates (500 μ m) and therefore bear some semblance to band edge absorption in the transmissions curves.

Figure 49 shows the bandgap values of the films as determined by the means described above. The values determined in this work are in good overall agreement with those reported in literature [76, 107, 114, 100, 109, 111], and exhibit a linear relation described by $E_g(x) = -2.79x + 6.75$ eV. The data gathered in this work suggests a slightly smaller change in optical bandgap with respect to Zn concentration ($|\delta E_g/\delta x|$), according to its linear fit. The greater disagreement is seen in the lowest concentration sample ($x = 0.12$) where the bandgap of our film was found to be 0.25 - 0.5 eV smaller than that in existing literature. This may be attributed to measurement or experimental error, however it is expected that cubic growth on MgO incurs different strain conditions than on lattice mismatched sapphire, thereby inducing changes in material properties such as bandgap. Interestingly, all the data presented in this figure suggests a rather poor linear

extrapolation to the bandgap of binary MgO, which would be underestimated by 0.6 – 1 eV by all data shown. Yet, to the authors’ knowledge, the relationship of the cubic ternary has only been presented as a linear one, as in references [76, 114], for example. Likewise, the bandgaps of the films grown in this work are well correlated linearly, suggesting that this is an appropriate relation to ascribe to the dependence. That stated, it may be that the bandgap values for low Zn content films are underestimated due to a high density of shallow-level defects which, like the F , $F+$ centers in MgO, are misconstrued for band edge transitions. If so, this defect warrants further investigation and should be well understood as it may be an important contributor to the film conductivity.

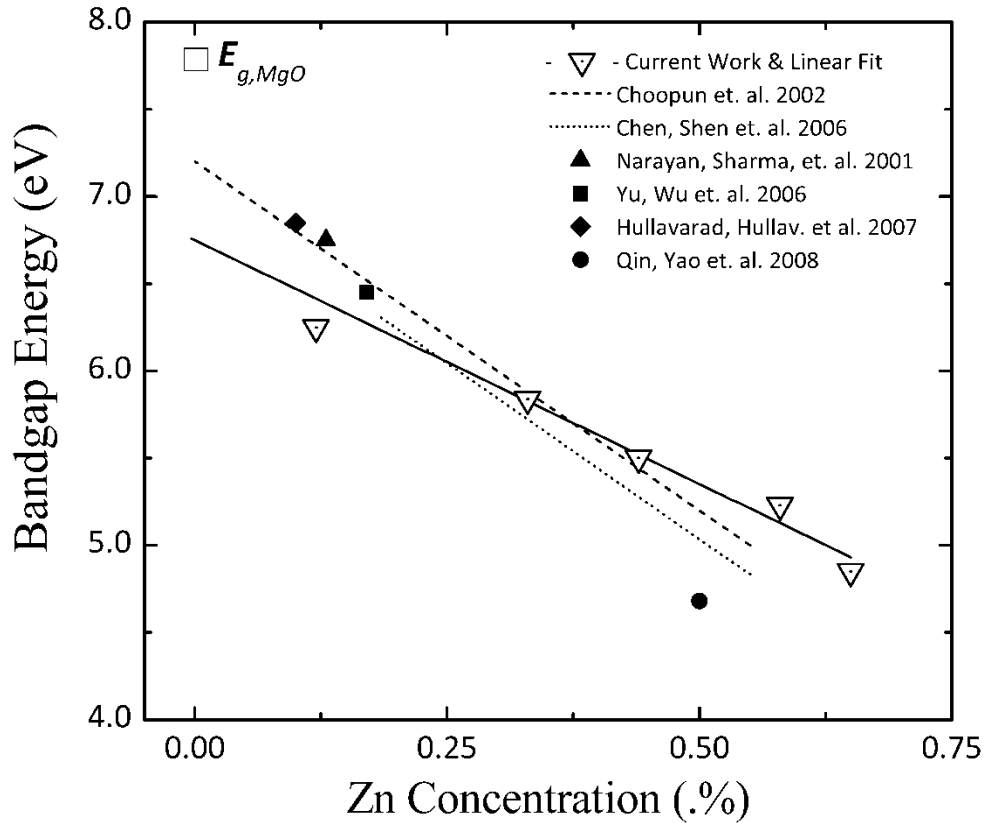


Figure 49. Bandgap values of the five ternary films plotted versus Zn concentration, x , shown with the accepted bandgap value of binary MgO and various published values from other works.

Finally, Figure 50 shows the resistivities of the films as determined by Hall measurements. There are three distinct tiers in the values measured, all of which were found to be *n*-type in carrier type. First, the four cubic heteroepitaxial films ($x = 0.12$ through 0.58) were found to have similar resistivities around $1 \times 10^6 \Omega/\text{cm}$. The phase segregated sample ($x = 0.65$) exhibited lower resistivity by a factor of approximately four while the homoepitaxial film ($x = 0$) had a resistivity almost 3 orders of magnitude greater than those of the cubic ternary ones. The lower resistivity of the phase segregated sample may be attributed to defects – possibly grain boundary states – which facilitate conduction of carriers generated within the grains. The higher resistivity of the homoepitaxial film is not as readily explicable. It is possible that the crystal quality is better for the MgO homoepitaxial film due in part to reduced total cation flux during growth, which would allow for better surface mobility of adatoms. This conjecture is supported in part by the more narrow diffraction peaks observed in XRD for this film, as well as slightly smoother surface morphology. Also, however, it is known that MgO has a high ionicity (as such it is categorically labeled as ionic) and carriers are therefore inherently less itinerant. The presence of Zn atoms within the lattice may serve not only to reduce the bandgap and (thereby increasing active carrier concentration at a given temperature), but also to improve mobility. In the measurements made, while the conductivity values were highly consistent, the carrier concentrations and mobility values vacillated somewhat and are therefore not presented here. This conductivity change in binary MgO may be related to the seemingly abrupt change in

bandgap value for MgO discussed above. It seems clear that more interrogation of low Zn concentration films would help elucidate the mechanisms of these observations.

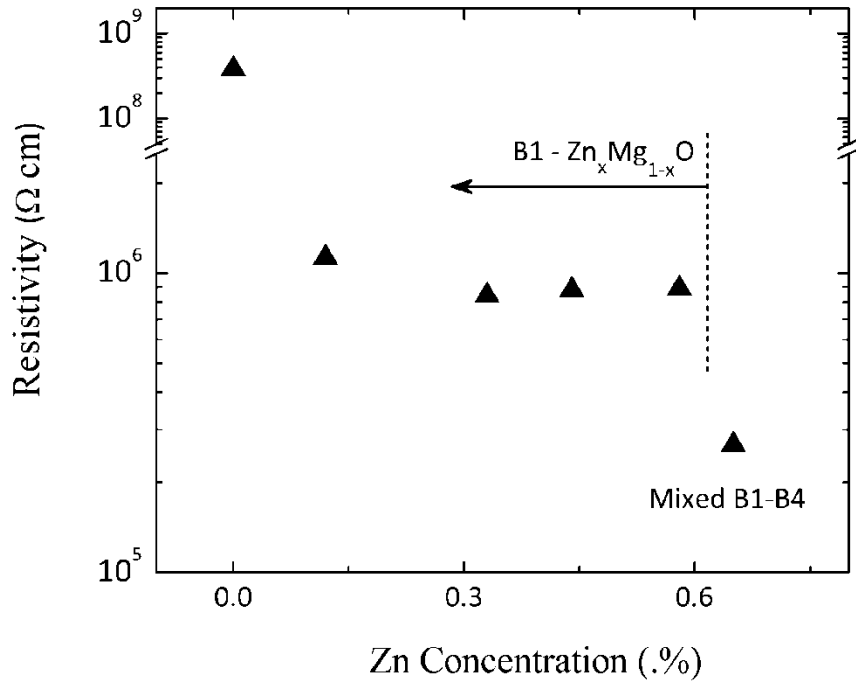


Figure 50. Electrical conductivities of the ZnMgO films and the MgO homoepitaxial one.

In summary, the ZnMgO films were found to have good overall surface morphology indicative of high quality. X-ray diffraction measurements corroborated this assessment and also indicated a linear relation of the lattice constant to Zn concentration. Transmission measurements were used to determine material bandgap variation with Zn mole fraction, demonstrating a linear shift from 6.25 to 4.85 eV as Zn mole fraction was increased from 0 to

0.58. ZnMgO with $x=0.65$ exhibited a mixed phase of B1 and B4 crystal structure, consistent with other studies in the literature. Interestingly, as observed by other groups, the linear behavior of the bandgap energy fails to extrapolate well to the accepted bandgap value of MgO, 7.8 eV. Finally, Hall measurements of the films quantified their high resistivity thereby demonstrating their suitability for future extrinsic doping.

ZnMgO DBR

One of the minor, yet noteworthy proof-of-concept growth efforts pursued briefly was the attempt to grow a deliberately designed, wavelength specific reflective structure. Such a reflective structure, termed a distributed Bragg reflector (DBR), would demonstrate the ability to accurately control layer thicknesses and concentrations while maintaining optical smoothness. Thus, once sufficient quality had been achieved with ZnMgO, the DBR growth was attempted.

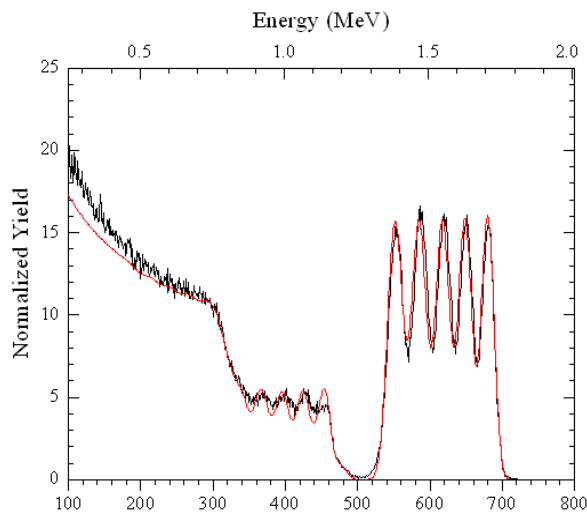


Figure 51. RBS spectra of a 5-period ZnMgO distributed Bragg reflector

The thickness of the layers needed to realize a DBR were estimated by analyzing the laser reflectometry (using a red laser diode, as previously described) and making corrections for the intended wavelength. In the case presented here, the structure was designed for a peak reflection at $\lambda = 350$ nm. The thicknesses of the ZnMgO and MgO layers were estimated to be 48.1 nm and 50.7 nm, respectively. The results of RBS taken on the sample are shown in Figure 51. The measured backscattered spectrum was well modeled using the intended design thicknesses. The optical measurements of the DBR are shown in Figure 52. The structure shows desired optical properties and exhibits a peak reflectance at 341 nm. The peak reflectivity is approximately 91% at this wavelength. Such a deliberately designed DBR shows the potential of this growth technique in multilayer structures.

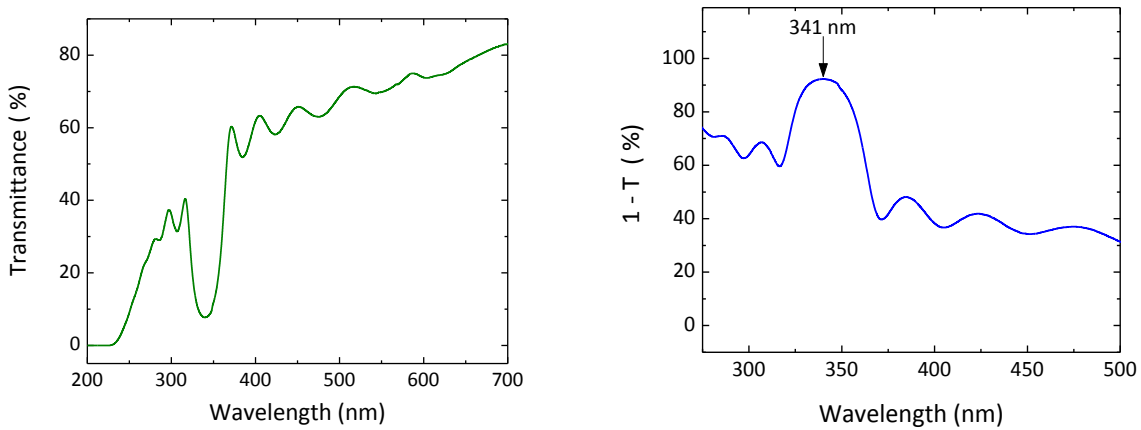


Figure 52. Transmittance (left) and approximate reflectance (right) of the ZnMgO/MgO DBR.

ZnMgO Device Characterization

Observation of photoresponse from cubic ZnMgO was one of the latest significant findings in the investigation. This was due in large part to the difficulty associated with maintaining cubic crystal structure with a sufficiently high Zn concentration to observe a photocurrent. Early ZnMgO films did not exhibit measureable photoconductivity, but this may ultimately be attributed to the fact that the MSM device patterns used at that time were very small area and had relatively large electrode finger separation. Additional complications with ZnMgO growth arose after MBE system underwent major maintenance and the previously described film qualities and band edge characteristics were challenging to reproduce. Finally, after numerous growths attempts, a ZnMgO was grown which showed a very encouraging photoresponse.

In the case of this particular sample, a lower growth temperature was employed to promote integration of significant Zn into the film while maintaining a strictly cubic structure, which was the primary challenge in the final series of growths. The successful film was grown at a substrate temperature of 200 °C, with a Mg cell temperature of 350 °C, a Zn cell temperature of 340 °C and an oxygen flux of 2.5 sccm. Based on previous data, the approximate percent of Zn present in the film (x) is estimated to be 0.4. The results of XRD measurements are shown in Figure 53 which confirm the strictly cubic structure of the film. The peaks present are attributed to the cubic phase ZnMgO (001) and (002) spacings.

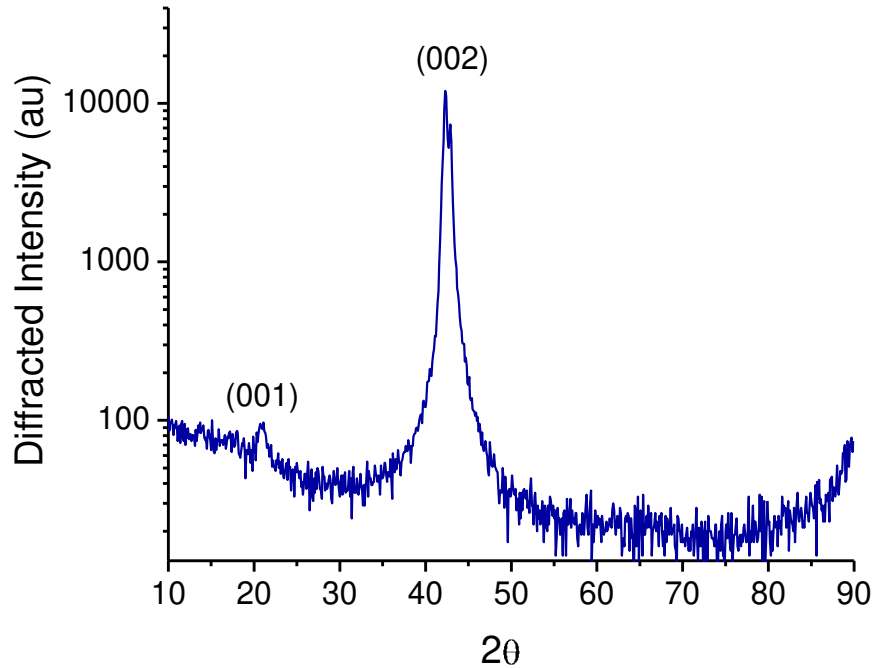


Figure 53. X-ray diffraction measurement of a $\text{Zn}_{0.4}\text{Mg}_{0.6}\text{O}$ thin film exhibiting strictly cubic structure, as indicated by the absence of any hexagonal peaks.

Figure 54 shows the spectrotemporal data set of a MSM device fabricated from the $\text{Zn}_{0.4}\text{Mg}_{0.6}\text{O}$ film. The particular MSM under test featured an electrode finger spacing of $5\ \mu\text{m}$ and utilized Pt: Au contacts. Note that the MSM device here does not exhibit an observable persistent photoconductivity as do the NiMgO films and this is an obvious advantage of these films over the NiMgO ones in their application to MSM detectors. Figure 55 shows the spectral cross section of the spectrotemporal response plotted with the transmission of the film. The cutoff wavelength is approximately 260 nm and demonstrates unambiguously the deep-UV applicability of this ternary compound.

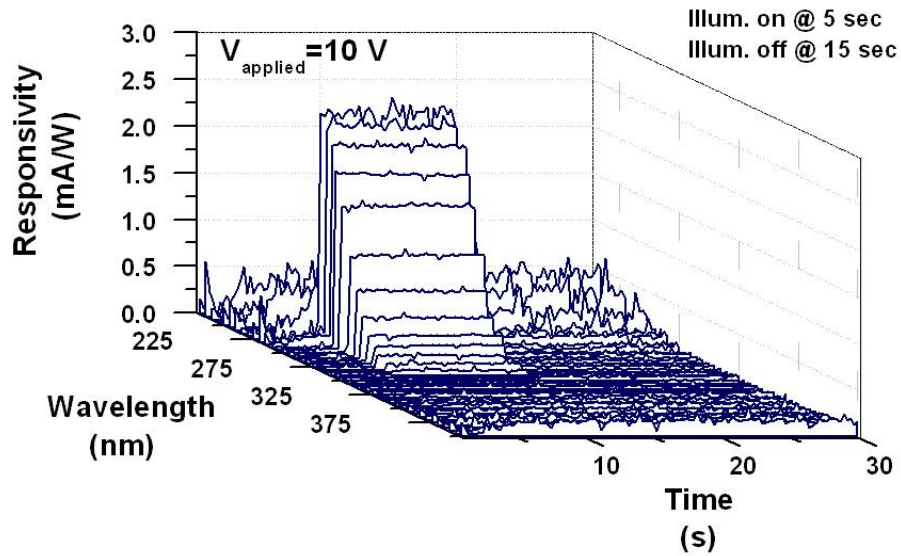


Figure 54. Spectrotemporal response of the ZnMgO film showing deep UV spectral response with a cutoff wavelength of approximately 260 nm.

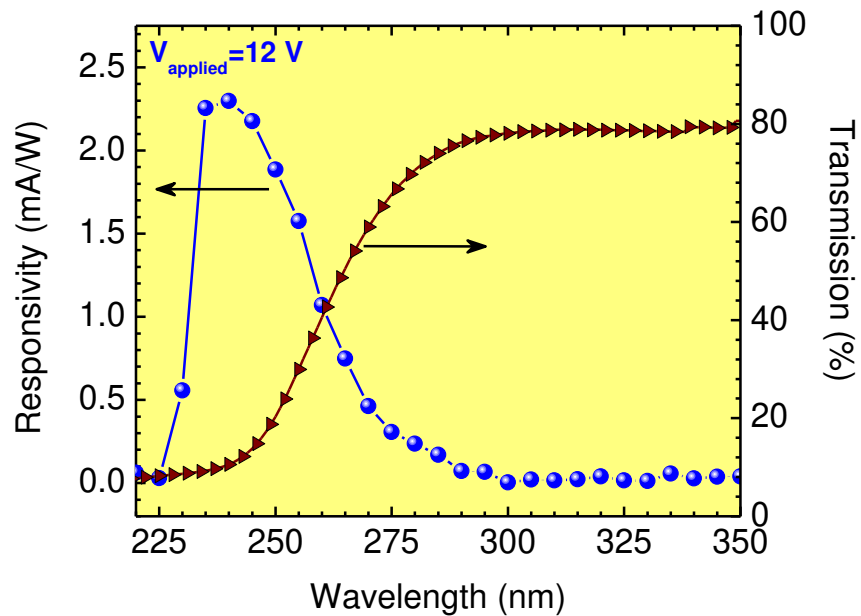


Figure 55. Photoresponse of the $Zn_{0.4}Mg_{0.6}O$ thin film plotted with the film's transmission measurement.

CdZnO

One of the initial pertinent investigations conducted by the author was a study of the optical and morphological properties of the ternary compound, $\text{Cd}_x\text{Zn}_{1-x}\text{O}$. This research was conducted in cooperation with SVT Associates Inc. (Eden Prairie, MN), an epitaxial equipment manufacturer who is credited with the growth of the films studied.

Incorporation of Cd into ZnO decreases the band gap of the semiconductor and, much like $\text{Zn}_x\text{Mg}_{1-x}\text{O}$, $\text{Cd}_x\text{Zn}_{1-x}\text{O}$ has been investigated for this reason as an optoelectronic material [115-121], driven greatly by the potential for visible wavelength devices. The research conducted by the author was not initially on film growth nor was it related to device fabrication. Rather, the investigation was one of materials characterization. This research later matured into device fabrication and subsequently film growth. The characterization research was conducted at two levels of scrutiny. The first work was a more cursory optical and morphological investigation. This was followed later by a more detailed investigation of the refractive indices of the $\text{Cd}_x\text{Zn}_{1-x}\text{O}$ films. In this section both works are presented for completeness but also because this section serves as an introduction to methods that will be used in continuing research.

Compositional and Morphological Characterization

The compositional and morphological properties of a semiconductor crystal are of obvious and intrinsic importance. Morphological quality is inherently indicative of, and related to, good crystal quality. Because the $\text{Cd}_x\text{Zn}_{1-x}\text{O}$ films were novel at the time, an assessment of the crystal quality had to be made. Once reasonably good semiconductor properties had been established, further research could be conducted. In order to examine these properties of the

$\text{Cd}_x\text{Zn}_{1-x}\text{O}$ thin films, various techniques were employed. Rutherford backscattering spectroscopy (RBS) correlated with secondary-ion mass spectroscopy (SIMS) were used to interrogate the films' compositional properties while the morphology was examined with atomic force microscopy (AFM).

RBS is an analytical technique used to determine material composition by measuring the energy of deflected, or backscattered, particles from a sample surface. The particles used in this case are He^{+2} ions with approximately 2 MeV energies. The experimental aspect of the RBS was carried out at a local material analysis center AMPAC and the data was analyzed and fitted by the author. Analysis of the data involves iterative conjecturing of layer thicknesses and compositions, generating mathematically modeled backscattered spectra and comparison of modeled and experimental data. This analysis exploits the use of a well-known RBS-specific program called RUMP.

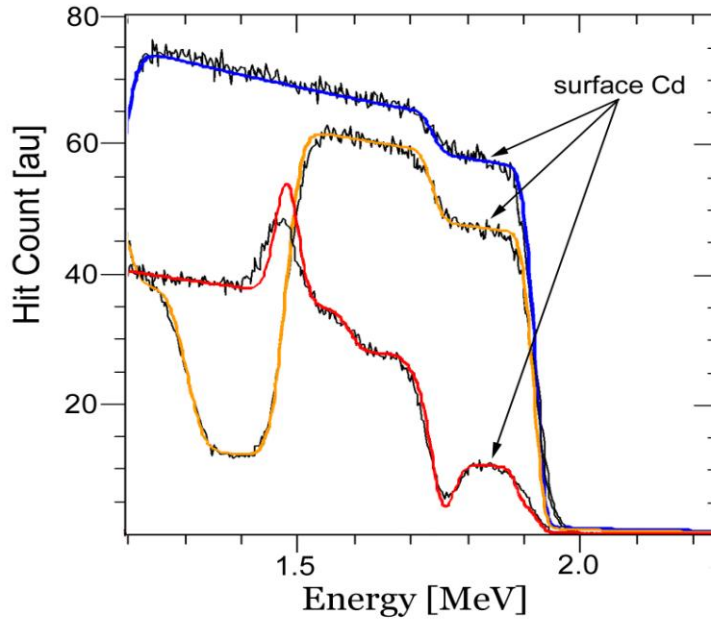


Figure 56. Rutherford Backscattering energy spectra of three $\text{Cd}_x\text{Zn}_{1-x}\text{O}$ samples

Figure 56 shows an example of RBS data collected from four samples of varying amounts of cadmium. The feature with the highest energy is that resulting from Cd component of the film. The figure indicates the percentages of cadmium concentrations which range from 9 – 77%. The steep slopes in the transition regions show abrupt interfaces between the layers. Also, the relatively consistent slopes seen on the top of most features are an indication of consistent composition throughout the individual layers. The sharp peak seen for one sample is the summed result of two elements which spectrally overlap (Zn and Cd, in this case).

As a secondary means of verifying the layer compositions, secondary ion mass spectrometry (SIMS) was used. SIMS is a compositional measurement technique that exploits a similar principle as RBS. In SIMS, ions are bombarded into a material surface and the secondary ions produced are analyzed with mass spectrometry. SIMS is more sensitive to material

concentrations than RBS but is also more experimentally difficult to realize and it is destructive. SIMS which is used for depth profiling is termed *dynamic* SIMS in contrast to *static* SIMS (also referred to as shallow SIMS) which is used to analyze only the top monatomic layers of a sample. The SIMS measurements in this case were not carried out by the author, but by a collaborator as a means to help verify and correlate the RBS results. Figure 57 shows SIMS the results for one such sample.

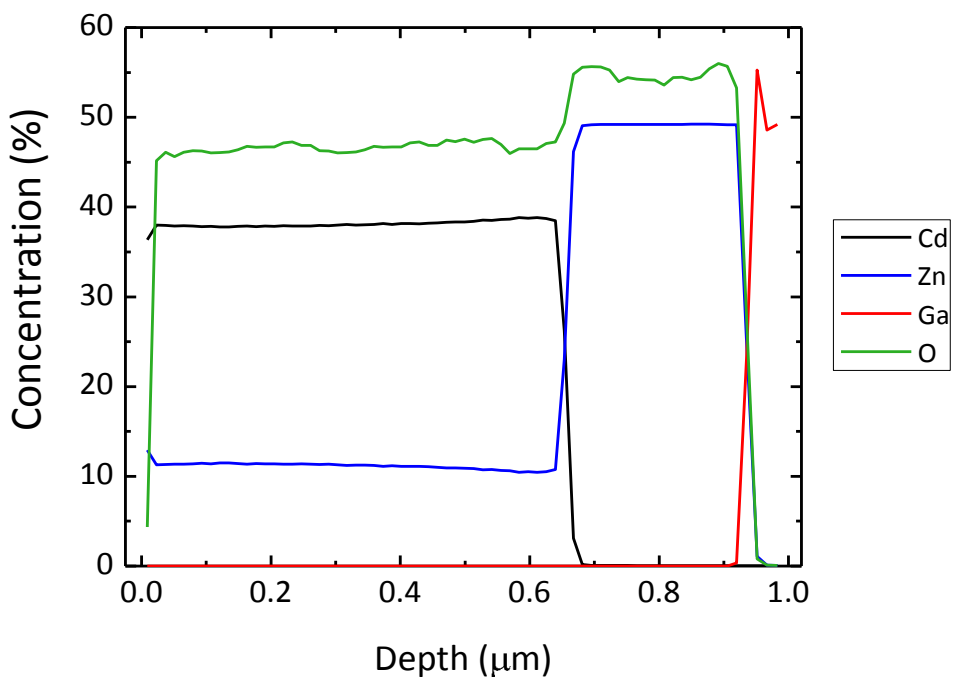


Figure 57. SIMS compositional analysis of a 36% cadmium sample

To characterize the morphology of the $\text{Cd}_x\text{Zn}_{1-x}\text{O}$ samples, atomic force microscopy (AFM) was carried out. AFM is a surface analysis technique in which an extremely fine cantilever tip (usually electron-beam etched) traces the surface of a material and is repulsed by

the material's close range forces (typically Van der Waals forces). In this case, a tapping mode AFM (TMAFM) was used to measure and image the sample surfaces. Figure 58a shows the TMAFM image from a GaN template used for the $\text{Cd}_x\text{Zn}_{1-x}\text{O}$ epitaxial growth. The GaN layer exhibits an RMS roughness of 1.5 nm. The surface of the $\text{Cd}_{0.02}\text{Zn}_{0.98}\text{O}$ epilayer has an RMS roughness of only 2.8 nm, and is highly uniform (Figure 58b). A moderate density (10^8 cm^{-2}) of surface features with a base width of 200 nm and a height of 10–20 nm occur sporadically on the surface. As the cadmium concentration is increased to 10% and 30%, the RMS roughness increases to 4.2 nm and 9.2 nm, respectively. For increasing concentrations of Cd, the density of surface features increases as do their respective aspect ratios [119].

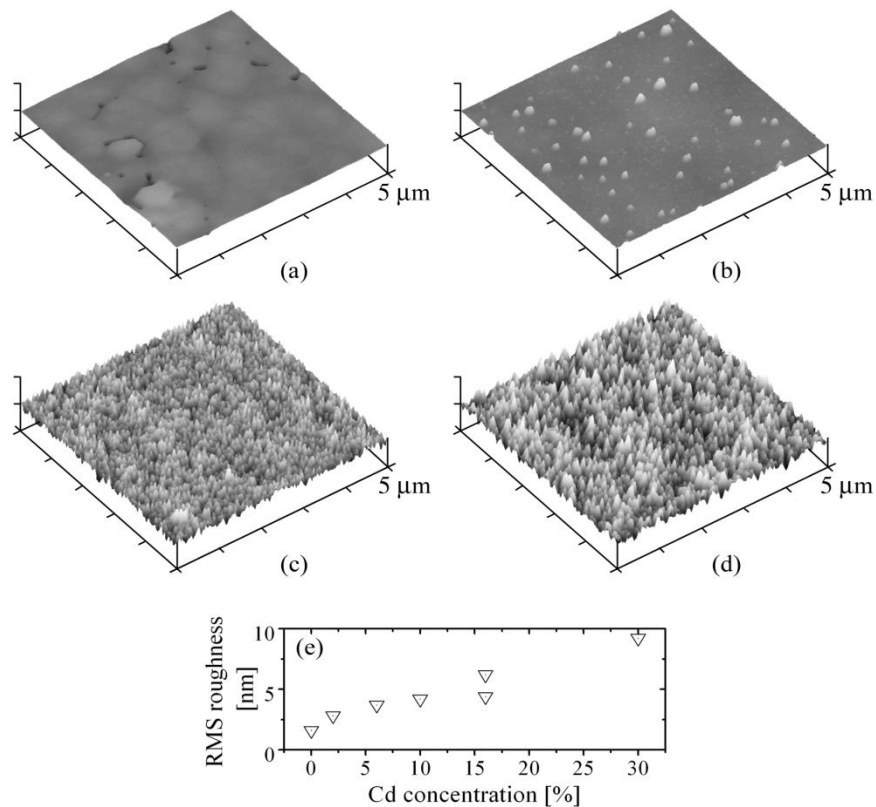


Figure 58. AFM scans of GaN nucleation layer (a), and 2, 10 and 30% cadmium samples (b-d), shown with roughness versus cadmium concentration for 7 samples (e).

Optical Characterization

Optical properties of the material system under study are of paramount interest in the characterization of the oxide films. The effects of alloying ZnO with Cd or Mg have been discussed with regards to the material band gap. The investigation conducted by the author focused on the optical properties of $\text{Cd}_x\text{Zn}_{1-x}\text{O}$ specifically. The first, cursory research sought to characterize the alloy in terms of its luminescence properties. The second work then characterized the films' refractive indices as a function of cadmium concentration.

The first study made on the optical properties of $\text{Cd}_x\text{Zn}_{1-x}\text{O}$ included photoluminescence and spectrophotometry. The aim of these studies can equally be considered as interrogations of the electronic band structure. In the case of photoluminescence, the samples are pumped with photon energies greater than the band gap. Electrons are excited to higher energy states and the subsequent relaxation to lower states (termed recombination, if it involves an electron-hole pair) results in the radiation of photons with energies less than or equal to that of the excitation source. Analyzing these radiated spectra then allows valuable inferences to be made about the material electronic structure. In the case of spectrophotometry, related though not identical information is obtained by pumping the sample with a beam of specific photon energy and measuring the light transmitted or reflected by the sample *at that energy*. Scanning this incident beam through a range of wavelengths results in a transmission or reflection spectra is useful in determining not only band gap characteristics but also refractive index.

The photoluminescence was carried out with a krypton ion (Kr^+) gas laser as the pump source, tuned to 350.7 nm (3.535 eV). The output power ranged from 120 to 140 mW, providing

intensities at the sample surface ranging from 0.01 to 4.2 W/cm². PL from the epilayers was collected with high numerical aperture lens and directed into a monochromator and detected using a thermoelectrically cooled CCD array. Figure 59 shows the measured PL and absorption for three samples of different cadmium concentrations [119]. The short-wavelength edge of the emission spectra correlates with the absorption edge. The absorption edge, and therefore the band gap, is shown to shift to lower energies with increased cadmium concentration. As the cadmium content increases, there is also a increase in the full-width half maximum (FWHM) of the dominant PL line. In every case, a red luminescence line appears between 675 and 750 nm. This red line is attributed to defects (largely compositional) and is analogous to the so-called yellow band in GaN. From the photoluminescence spectra, the peak values are measured and are shown in Figure 60 along with the FWHM as a function of cadmium concentration [119].

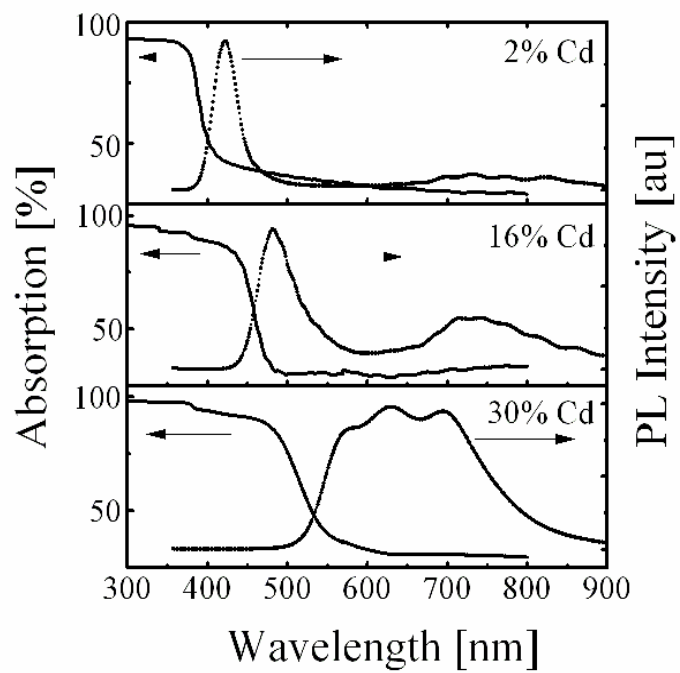


Figure 59. Photoluminescence and absorption for 2, 16 and 30% cadmium concentration samples.

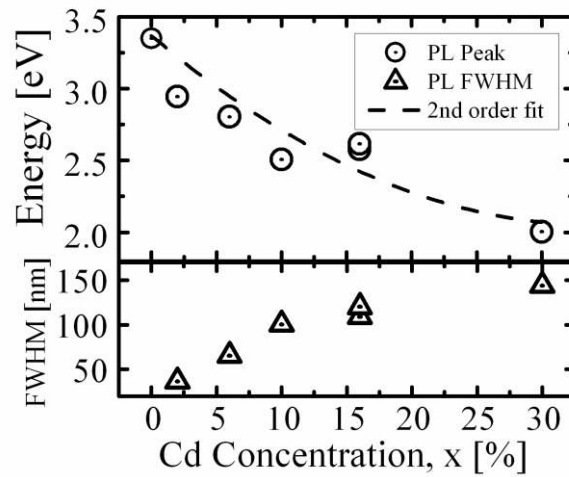


Figure 60. Band gap energy and PL FWHM as a function of cadmium concentration.

Complex Refractive Indices

Perhaps one of the significant contributions to $\text{Cd}_x\text{Zn}_{1-x}\text{O}$ studies made by the author is that of determining the complex refractive indices of these films as a function of cadmium concentration. The complex index of refraction of a semiconductor is important in order to characterize the material's ability to guide or transmit light in various devices. If the refractive index can be precisely tuned by varying material composition (and loss in the material is sufficiently low), the material can exploit passive wave-guiding in devices such as lasers.

In the investigation of $\text{Cd}_x\text{Zn}_{1-x}\text{O}$ thin films, transmission data was collected using spectrophotometry (transmission mode) and a genetic algorithm was used to fit known dispersion relations to the collected data. In this data fitting, a matrix formalism is employed which allows convenient representation of the optical properties of the multi-layer samples.

The fitting algorithm functions as a standard evolutionary algorithm often used in such multi-variable model-fitting and optimization problems [122, 123]. The algorithm initiates by posing a set of solutions consisting of dispersion relation parameters in a predefined parameter space. The solutions are then evaluated by calculating the point-by-point least-squares difference, χ^2 between the measured spectrum, and the spectrum predicted by the solution,

$$\chi^2 = \frac{\sum_j (T_T(\lambda_j) - T_E(\lambda_j))^2}{N} . \quad (1)$$

N is the number of points, and T_T and T_E are the theoretically predicted and experimentally measured values of transmission, respectively. A transmission stacked-matrix formulation method is used to model the transmission of the multilayer structure. Figure 61 shows the mathematical assignments for transmission matrices.

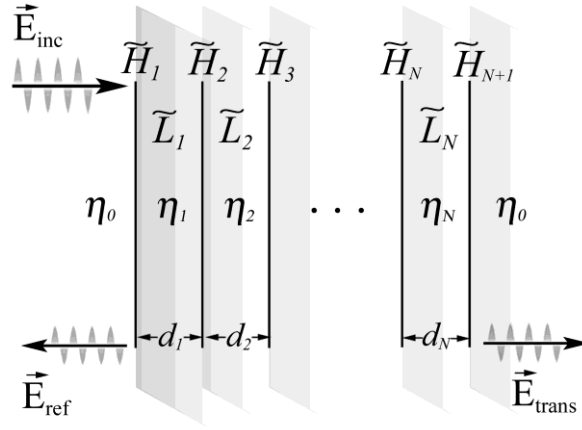


Figure 61. Variable assignments for spectrophotometric measurement of thin films.

Interfaces are represented by reflection matrices \tilde{H}_i , and film layers by propagation matrices \tilde{L}_i :

$$\tilde{H}_i = \frac{1}{\tau_i} \begin{bmatrix} 1 & r_i \\ r_i & 1 \end{bmatrix} \quad (2)$$

$$\tilde{L}_i = \begin{bmatrix} e^{i\beta_i} & 0 \\ 0 & e^{-i\beta_i} \end{bmatrix} \quad (3)$$

Here, τ_i and r_i are the wavelength dependent Fresnel transmission and reflection coefficients at the interface. Variables η_i are the complex indices of refraction of the layers and d_i are layer thicknesses. Propagation constants for the layers, β_i , are given at normal incidence as

$$\beta_i(\lambda) = \frac{2\pi}{\lambda_0} \eta_i(\lambda) d_i \quad (4)$$

By concatenating matrices, a thin film structure with an arbitrary number of layers can be represented as

$$\tilde{M}_{system} = \tilde{H}_{N+1} \tilde{L}_N \dots \tilde{H}_2 \tilde{L}_1 \tilde{H}_1 \quad (5)$$

$$\tilde{M}_{system} = \begin{bmatrix} s_{11} & s_{12} \\ s_{21} & s_{22} \end{bmatrix} \quad (6)$$

From the system matrix, transmission coefficients T are determined by the equation

$$T = t^2 = \left(\frac{1}{s_{22}} \right)^2 \quad (7)$$

solutions are ranked in order of decreasing error and are procedurally altered through a pseudo-random parameter perturbation function known as Gaussian mutation. This process is repeated until a minimum error is achieved and a solution is converged upon.

Two optical dispersion models were chosen for their simplicity and applicability. For the transparent regime where the loss is considered negligible ($\kappa \approx 0$) the Sellmeier model is given by

$$n^2(\lambda) = A + \frac{B\lambda^2}{\lambda^2 - C^2} \quad (8)$$

Where A , B , and C are fitting parameters. In the absorbing region at shorter wavelengths the multiple oscillator Forouhi-Bloomer (FB) model is used:

$$n(E) = n(\infty) + \sum_{i=1}^q \frac{B_{0i}E + C_{0i}}{E^2 - B_iE + C_i} \quad (9)$$

$$k(E) = \sum \frac{A_i(E - E_g)^2}{E^2 - B_iE + C_i} \quad (10)$$

in which $n(\infty)$, A_i , B_i , C_i and E_g are the five fitting parameters, and B_{0i} , C_{0i} and Q_i are given by

$$B_{0i} = \frac{A_i}{Q_i} \left(-\frac{B_i^2}{2} + E_g B_i - E_g^2 + C_i \right) \quad (11)$$

$$C_{0i} = \frac{A_i}{Q_i} \left[(E_g^2 + C_i) \frac{B_i}{2} - 2E_g C_i \right] \quad (12)$$

$$Q_i = \frac{1}{2} (4C_i - B_i^2)^{1/2} \quad (13)$$

This model is consistent with the Kramers-Kronig relation and has been used to model the refractive indices of many optical materials including both dielectrics and semiconductors.

An advantageous property of the FB model is that the imaginary component of index of refraction, and therefore the absorption coefficient, is identically zero at the wavelength value of the band gap parameter. The first step in fitting the transmission spectra, therefore, consisted of extending the FB domain (absorptive region) until the zero-absorption point was determined. The data for each sample is then divided at its respective approximate band gap parameter. The transmission spectra above this energy parameter are treated with the FB model, and the spectra below it are treated with the Sellmeier dispersion model. It is important to note that while E_g is referred to as the band gap parameter, this value *does not* accurately represent the true semiconductor band gap. This is because absorption occurs at energies below the band gap due to excitonic absorption and band tailing effects. The model nonetheless remains functional when the band gap parameters are less than the material band gap, and the various absorption phenomena are represented by oscillator terms [124-126].

The resulting refractive indices in the visible region for six different cadmium concentrations are shown in Figure 62. The real refractive index was shown to increase with increasing cadmium content. In addition, the absorption edge was shown to shift to lower energies with increasing cadmium as seen in Figure 63 (right). In general, there was a shift in the peak of the real refractive indices. The behavior for the two highest cadmium concentration samples was distinct from the other four. This is discussed fully in the pertinent reference but, in summary, it is attributed to changes in crystal quality due to the higher cadmium incorporation [120].

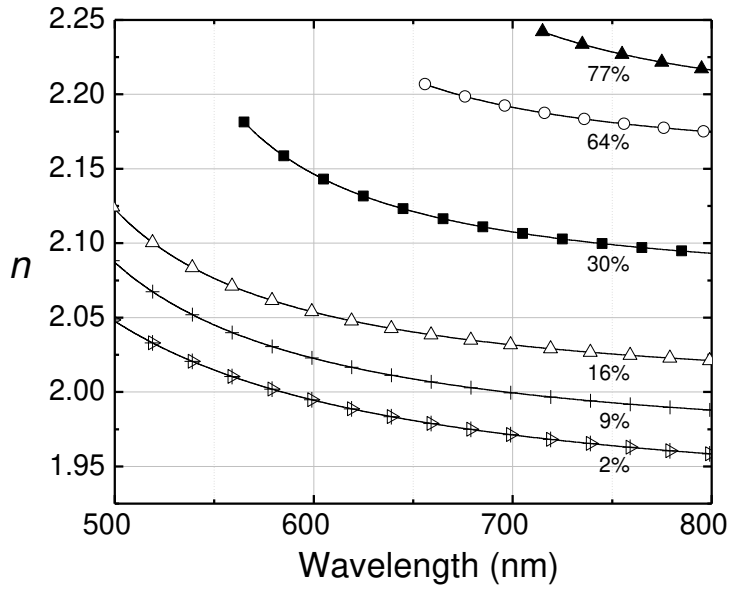


Figure 62. The refractive indices of $\text{Cd}_x\text{Zn}_{1-x}\text{O}$ thin films for six different Cd percentages, as fit to the Sellmeier dispersion relation.

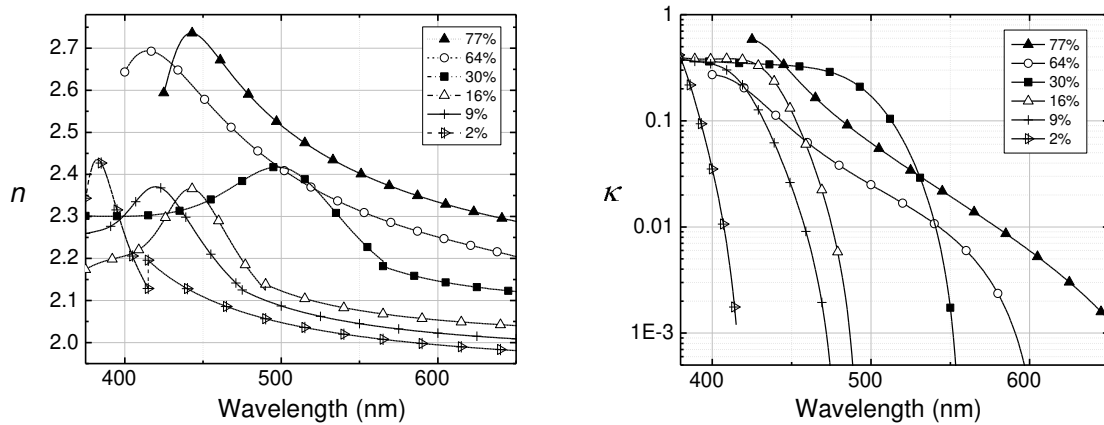


Figure 63. The real (left) and imaginary (right) refractive indices for six samples of $\text{Cd}_x\text{Zn}_{1-x}\text{O}$ thin films.

Table 2. Coefficients for dispersion model fits for Cd_xZn_{1-x}O samples.

Cd (%)	Forouhi-Bloomer						Sellmeier			
	$n(\infty)$	E_g	A_i	B_i	C_i	λ	A	B	C	λ
2	1.530	2.949	0.097	6.596	10.902	375-420	3.118	0.592	0.335	420-800
			0.00004	8.575	23.922					
			0.064	10.105	26.928					
			0.076	13.062	44.02					
9	1.601	2.612	0.099	5.957	8.93	375-474	3.498	0.349	0.385	474-800
			0.016	6.742	11.419					
			0.019	8.687	18.884					
			0.017	11.39	34.521					
16	1.605	2.514	0.086	5.650	8.017	375-493	3.724	0.268	0.405	493-800
			0.095	6.463	10.703					
			0.079	7.880	17.077					
			0.081	12.170	41.687					
30	1.711	2.224	0.186	4.872	6.005	375-557	4.090	0.187	0.480	557-800
			0.080	6.056	9.947					
			0.007	6.972	63.718					
			0.037	11.649	34.141					
64	1.726	1.887	0.010	3.731	3.489	400-657	4.489	0.136	0.525	657-800
			0.052	6.332	10.156					
			0.067	8.116	20.672					
			0.096	10.065	27.203					
77	1.707	1.733	0.007	5.794	8.418	425-715	4.587	0.160	0.571	715-800
			0.074	6.580	11.186					
			0.225	15.240	84.594					
			0.015	12.933	44.936					

Hybrid and Fully-Oxide Devices

Another significant and relevant investigation conducted by the author was on the fabrication and characterization of ZnO-based quantum well active region light emitting devices. The structures for this work were again grown by the research division at SVT Associates. Two types of structures were grown, fabricated and characterized. Both of the structures are novel in their design and represent the current forefront of oxide light emitting devices.

The two types of devices may be distinguished as hybrid ZnO-based and fully ZnO-based quantum well light emitting diodes (LEDs). The former category of LED is a *p-i-n* structure device in which the p-type region consists of Mg-doped GaN while the n-type region is Ga-doped ZnO. The use of a GaN p-region circumvents the difficulties in p-doping of ZnO [74, 66]. Fully ZnO-based, on the contrary, rely upon N-doped ZnO as the p-type materials. Nitrogen has been used successfully as a p-type dopant, but has a high activation energy (170 – 200 meV) and therefore results in relatively low carrier concentrations. Both of these structures, however, did weakly emit light and were therefore functional. Figure 64 shows the structures of both types of LEDs. The hybrid LED exemplified in this work was a single quantum well device while the fully ZnO one is a multiple quantum well structure, though variations of these were also fabricated. This section will describe the fabrication and testing of both kinds of LEDs.

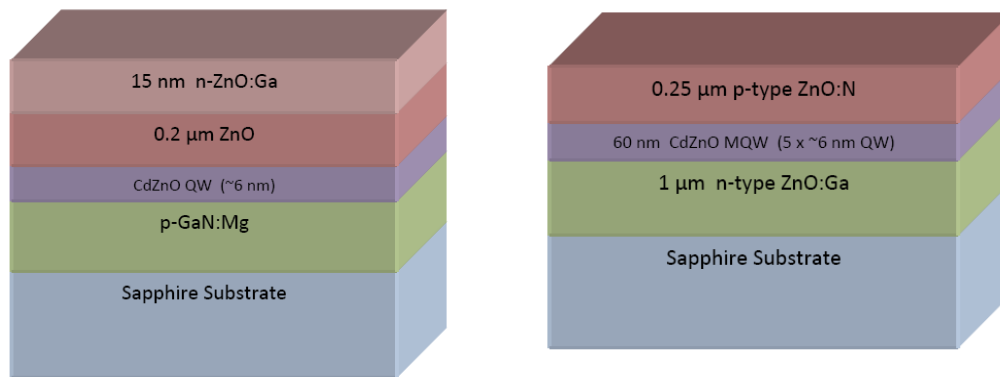


Figure 64. (Left) Hybrid ZnO-based single quantum well LED and (right) fully ZnO-based multiple quantum well LED

Hybrid

Prior to fabrication, the CdZnO/GaN LED structures were cleaned by heating in acetone at 80 °C for 4 minutes, then rinsed with acetone, isopropyl alcohol and deionized water to remove potential contaminants from the sample surface. Samples were then heated on a hot plate at 100 °C to ensure that the surface was free of all solvents prior to applying photoresist.

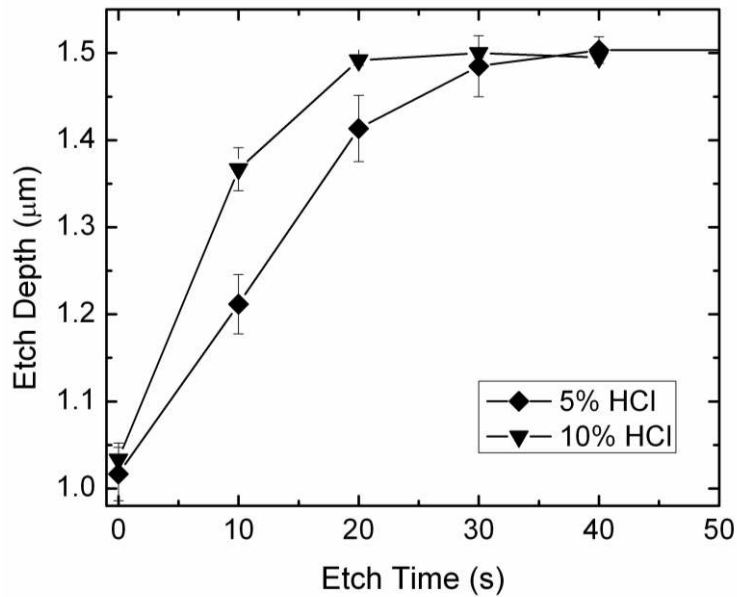


Figure 65. The etch depth as a function of time for the CdZnO/GaN hybrid LED. Note that the nonlinearity in the etch rate is due to saturation of the etchant volume used.

Standard lithographic processes were carried out using positive photoresist (Shipley S1813) and a Karl Suss MJB3 mask aligner. The first pattern exposed and developed was that for the LED device mesa. In order to etch the isolation mesa patterns down to the p-type GaN region, HCl/H₂O solution was used. It should be noted that the ability to preferentially remove the upper n-type ZnO material while leaving the underlying p-type GaN layer in tact represents a unique advantage of such hybrid light emitting devices. Initial characterization of the etch rates was carried out using profilometry after successive 10 s emersions in solution. Figure 65 illustrates the etch rate of the hybrid structure for 5 and 10% HCl acid solutions.

After removing the resist, the etched mesa patterns were then examined using a Veeco Dimension atomic force microscope (AFM). Figure 66 shows the quality of a corner of one of the device mesas. The AFM scan illustrates the positive sidewalls of the mesa due to lateral etching of the ZnO, which undercuts the photoresist pattern. The slopes of the mesa reveal that lateral etching occurs faster than vertical etching by a factor of two, as seen in the cross-sectional AFM image; however, the 90° corner angle of the mesa pattern is preserved.

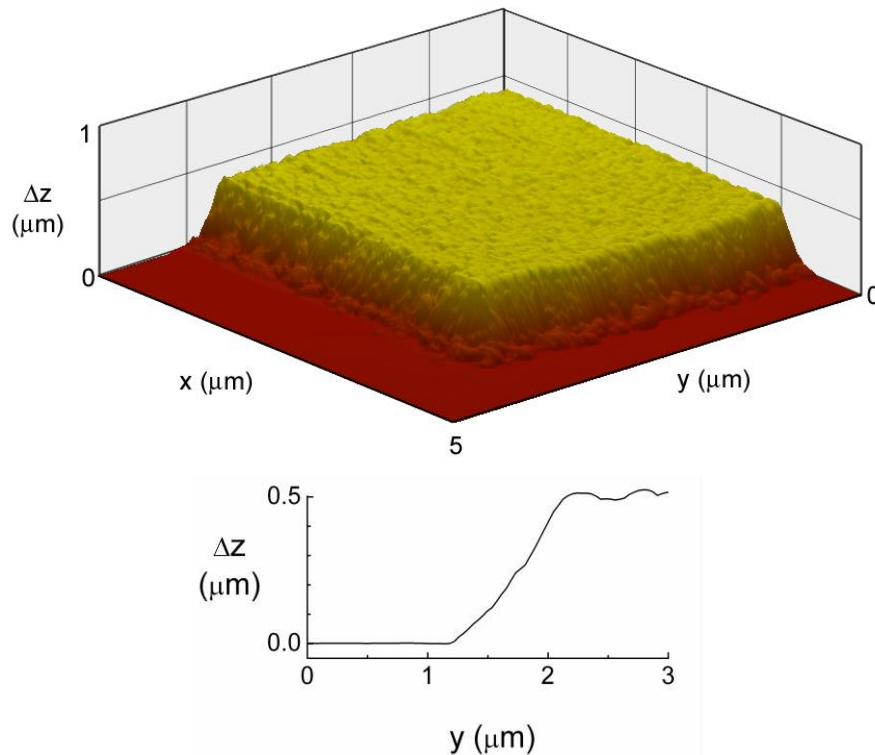


Figure 66. (Top) AFM image of a mesa corner. Sidewalls observed are due to lateral etching of ZnO by HCl/H₂O (Bottom) AFM cross-section revealing sidewall with a slope of $\Delta z/\Delta y = 1/2$.



Figure 67. An array of fabricated CdZnO/GaN LEDs.

Samples were then patterned for metal deposition of the device contacts. Contact metals were deposited by electron beam evaporation using a Temescal e-beam evaporator. Ni/Au (100 Å/2000 Å) metals were used for the p-GaN contacts and Ti/Au (200 Å/2000 Å) were used for the n-ZnO contacts. In both cases, metal removal in lift-off was accomplished by soaking the sample in acetone to remove photoresist. Figure 67 shows an array of completed LEDs.

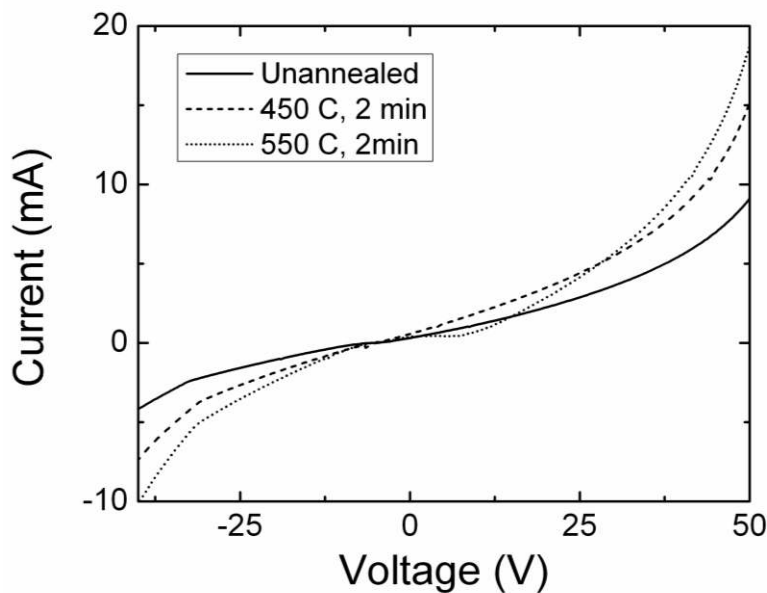


Figure 68. IV curves shown for a device prior to annealing, after 2 minutes of annealing at 450 °C and after 2 additional minutes of annealing at 550 °C.

Devices were initially characterized with current-voltage (IV) characteristics to verify diode-like electrical behavior. Devices were found to have forward voltages in the range 35 - 50 V and corresponding forward currents of 8 – 10 mA. In order to decrease the forward voltage for the devices, thermal annealing was carried out to promote diffusion of the contact metals into the doped regions of the structures. Reduction in the forward voltage was seen for those devices annealed. Figure 68 illustrates the change in IV characteristics for a device annealed at 450 °C for 2 minutes, then again at 550 °C for an additional 2 minutes.

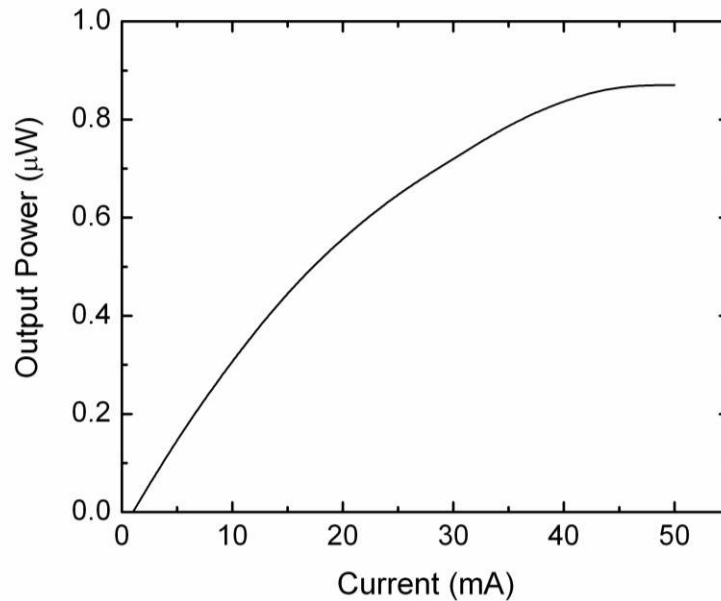


Figure 69. Light output versus current for a typical CdZnO/GaN LED.

Devices were also characterized with optical power output versus current (LI) measurements. To allow for ease of setup, devices were mounted on TO-56 headers and ultrasonically wire bonded with 1 mil (25 μm) gold wire using a Kulicke & Soffa 4524AD wire bonder. Light output was measured using an integrating sphere and a Newport 1835C optical power meter. Figure 69 shows the LI curve for one device. In addition, optical images of functional LEDs were taken. Figure 70 shows a functioning CdZnO/GaN LED.

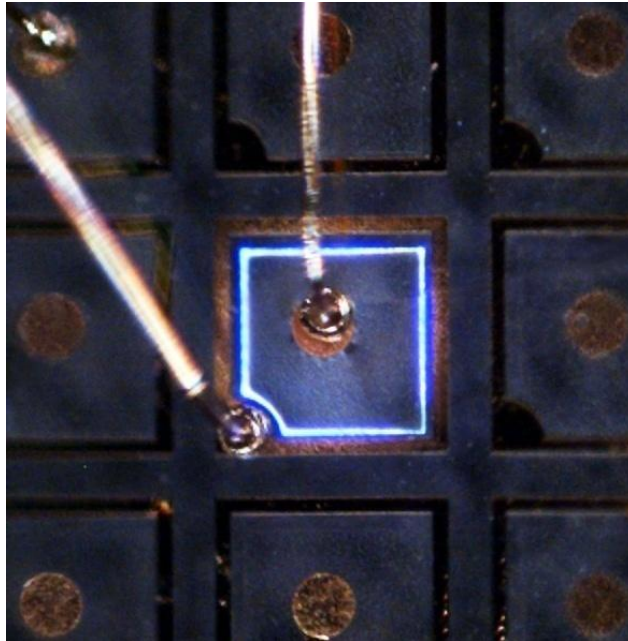


Figure 70. A functioning CdZnO/GaN LED emitting blue light.

Fully II-Oxide QW LED

In addition to the hybrid structures fabricated, fully ZnO-based devices were also researched by the student. These devices exploit the limited doping of ZnO with Nitrogen. In these structures, the n-type ZnO (gallium doped) is grown directly on a sapphire substrate with a thickness of approximately 1 μm . This is followed by multiple quantum wells (5 wells of 6 nm each) consisting of unintentionally doped $\text{Cd}_{0.12}\text{Zn}_{0.88}\text{O}$. The p-type, nitrogen doped ZnO is then grown to a thickness of 0.25 μm as the top (final) layer. Devices were fabricated from this structure and, to the student's knowledge, these devices represent the first ZnO/CdZnO, multiple quantum well LEDs.

Fabrication of the fully ZnO LEDs followed very much the same method as that described above for the hybrid structures with a few important distinctions. First, in the case of the fully ZnO structures, self-limiting wet etch could not be exploited because the buried n-type region is also ZnO. Therefore, the etching had to be appropriately timed to reach the correct depth for n-metal deposition without etching too deeply and reaching the highly insulating sapphire substrate. This presented a challenge in the fabrication process. Exacerbating this difficulty was the fact that the ZnO material in these structures etched much more quickly than it did in the hybrid structures. Furthermore, the resulting etched surface was extremely rough (~100 nm RMS roughness) and therefore it was difficult to assign an accurate etch depth for etch rate assessment. Figure 71 shows an AFM image of the etched mesa; note the trench nearest to the mesa is deeper than the surrounding etched region.

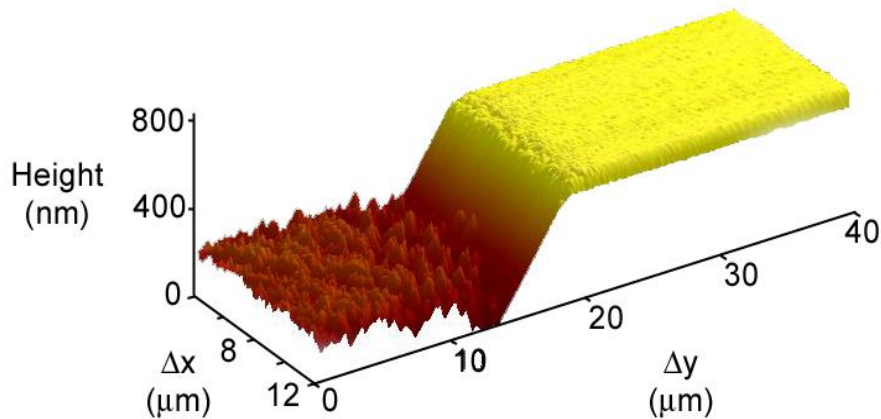


Figure 71. AFM of a wet-etched ZnO LED mesa.

In order to find an appropriate etch depth and time, therefore, a creative approach was taken. A variable-time wet etch procedure was developed and implemented in which the sample is slowly lowered in to the etching solution ($< 1\%$ HCl) at a constant speed and is then slowly removed. In this manner, the etch depth is varied across the sample surface; the regions that are exposed the longest are etched the deepest. The resulting fabricated samples are shown in Figure 72. After completion of the device fabrication the properties of the devices could be studied as a function of etch depth and time.

Figure 72 also illustrates the other difference between the fully ZnO devices and the hybrid ones. In the case of the fully ZnO LEDs, the device resistances were initially found to be extremely high. In order to inject a reasonable current (10s of mA), therefore, a very high voltage was necessary and the heat dissipation of the devices led to rapid device degradation. To reduced the device resistance use of a transparent contact was investigated. Transparent contacts are used in devices not only to improve electrical characteristic but also to promote better light extraction (or gathering, in the case of detectors). Dramatic improvement in the current-voltage (IV) characteristics is seen with the implementation of a 15 nm Ni transparent contact as shown in Figure 73.

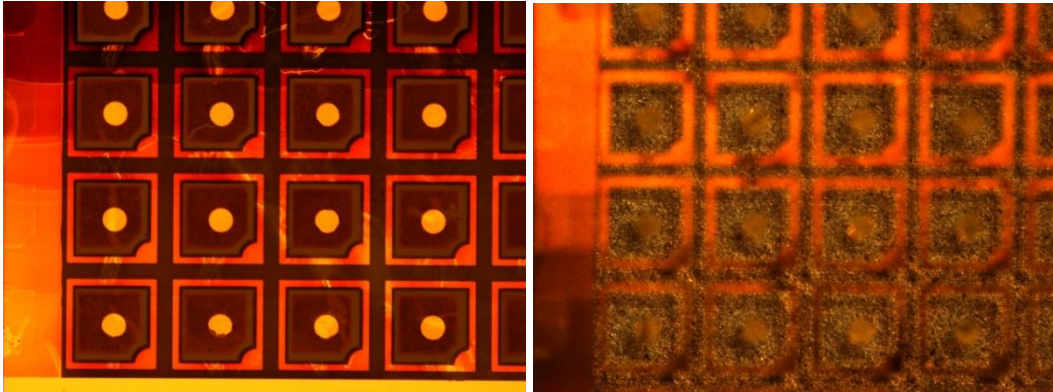


Figure 72. Fabricated fully ZnO MQW LEDs. The left image clearly illustrates the results of the variable-time etch rate procedure. The right image was taken of the same devices, but focused on the back surface of the substrate through the transparent contact layers which cover the mesas.

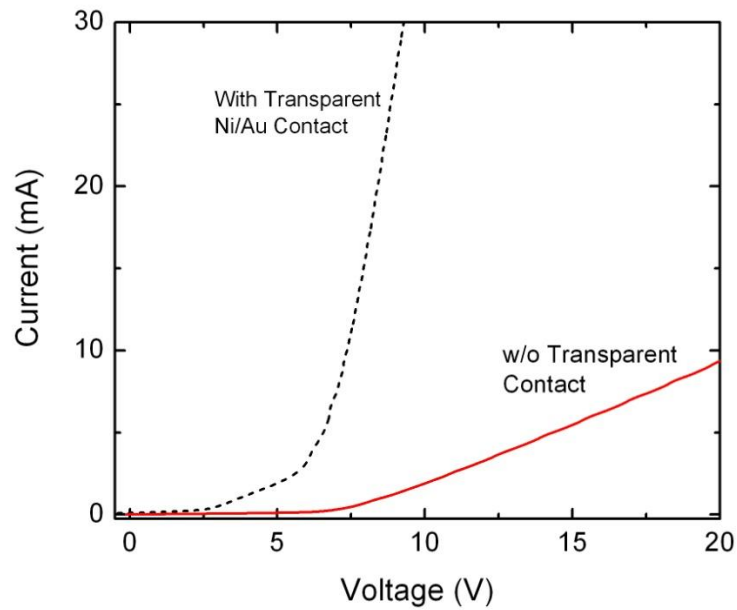


Figure 73. IV characteristics of fully ZnO LEDs with and without transparent contacts.

Successful proof-of-concept devices were realized both with and without transparent contacts. While the latter category exhibit superior IV characteristics, there was an impact on the

spectral properties of the light. The devices without a transparent emitted a clearly blue light, though they had to be driven at very high currents to observe it. The devices with transparent contacts produced visible light at lower currents, but the light appeared yellowish. This change is not yet understood in a strictly fundamental sense, but it is attributed to the presence of the Ni contact. In addition to the spectral change, the light emitted by the devices with transparent contacts was more uniform across the LED mesa while that produced by devices without the transparent contact was more isolated to the perimeters of the mesas indicating a current-spreading deficiency. Figure 74 shows these device features for the two categories. Unfortunately, the device brightness was so low and temporal (dying off quickly due to heat) that reliable spectral measurements could not be made.

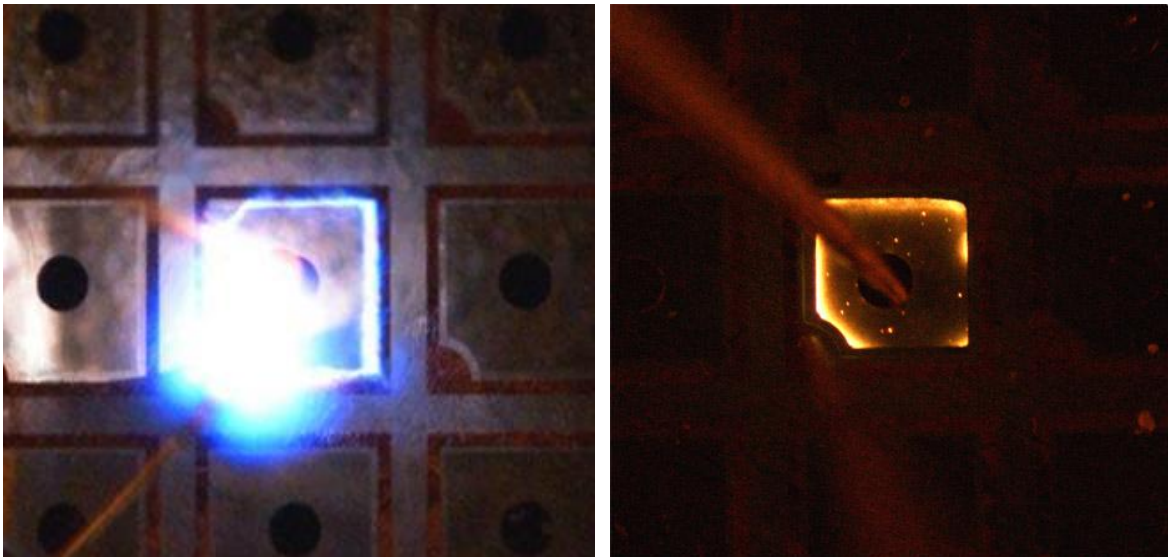


Figure 74. An operating fully ZnO LED without transparent contact (left, $I=65$ mA) and an analogous device with a 15 nm transparent contact (right, $I=35$ mA).

4. CONCLUSIONS

In this document, the growth, characterization and exploitation of wide bandgap oxide semiconductors has been presented. The predominant focus was upon the two relatively novel cubic oxides, NiMgO and ZnMgO. In both cases, films were grown by oxygen plasma-assisted molecular beam epitaxy on lattice matched substrates, among others. The evolution of growth parameters and techniques applied by the author eventually engendered high quality films sufficient for device fabrication. The films were characterized by various techniques including Rutherford Backscattering, X-Ray diffraction, atomic force microscopy and spectrophotometry. Metal-semiconductor-metal devices were fabricated from both ternaries and both showed to exhibit ultraviolet photoconductivity, as desired. The responsivities of the devices were characterized and methods of improvement of growth quality were pursued with success. Critically important, is the conclusion that both the two ternary compounds under study showed applicability as deep-UV optoelectronic materials – an assertion which was the function hypothesis of the whole endeavor.

Additionally, the characterization and exploitation of CdZnO was carried out with significant findings. First, a thorough study of the refractive indices of the ternary compound was carried out. In a collaborative effort, fully-ZnO based devices and hybrid structures were grown by MBE, fabricated into devices and characterized electrically and optically. The first instance of a n-ZnO/i-CdZnO/p-GaN MQW LED was demonstrated and functional novel fully-ZnO p-i-n devices were also demonstrated.

In summary, a body of research is presented which provides strong evidence, in various ways, the unique applicability of oxide compounds to wide bandgap optoelectronics.

5. REFERENCES

- [1] T. Kaufmann, G. Fuchs, M. Weibert, S. Frieske and M. Gäckle: MOCVD layer growth of ZnO using adducts of dimethyl- and diethylzinc. *Crystal Research and Technology* 24, 269 (1989).
- [2] S. Yadavalli, M. H. Yang and C. P. Flynn: Low-temperature growth of MgO by molecular-beam epitaxy. *Physical Review B* 41, 7961 (1990).
- [3] G. Chern, S. D. Berry, D. M. Lind, H. Mathias and L. R. Testardi: Modulated Electric-Conductivity in $\text{Fe}_3\text{O}_4/\text{NiO}$ Superlattices. *Applied Physics Letters* 58, 2512 (1991).
- [4] D. K. Fork, F. A. Ponce, J. C. Tramontana and T. H. Geballe: Epitaxial MgO on Si(001) for Y-Ba-Cu-O Thin-Film Growth by Pulsed Laser Deposition. *Applied Physics Letters* 58, 2294 (1991).
- [5] N. J. Ianno, L. McConville, N. Shaikh, S. Pittal and P. G. Snyder: Characterization of pulsed laser deposited zinc oxide. *Thin Solid Films* 220, 92 (1992).
- [6] E. Fujii, A. Tomozawa, S. Fujii, H. Torii, M. Hattori and R. Takayama: NaCl-Type oxide-films prepared by plasma-enhanced metalorganic chemical-vapor-deposition. *Japanese Journal of Applied Physics Part 2-Letters* 32, L1448 (1993).
- [7] R. Hiskes, S. A. DiCarolis, R. D. Jacowitz, Z. Lu, R. S. Feigelson, R. K. Route and J. L. Young: Single source MOCVD of epitaxial oxide thin films. *Journal of Crystal Growth* 128, 781 (1993).
- [8] R. Naidoo, R. Pretorius and C. M. Comrie: Formation of $\text{Y}_1\text{Ba}_2\text{Cu}_3\text{O}_{7-x}$ thin films by pulsed ruby laser ablation. *Superconductor Science and Technology* 7, 57 (1994).
- [9] M. Johnson, S. Fujita, W. Rowland, W. Hughes, J. Cook and J. Schetzina: MBE growth and properties of ZnO on sapphire and SiC substrates. *Journal of Electronic Materials* 25, 855 (1996).
- [10] Y. Tasaka, H. Kuroda, M. Tanaka and S. Usami: Velocity analysis of ablated particles in pulsed laser deposition of NiO film. *Thin Solid Films* 281-282, 441 (1996).
- [11] D. Dijkkamp, T. Venkatesan, X. D. Wu, S. A. Shaheen, N. Jisrawi, Y. H. Min-Lee, W. L. McLean and M. Croft: Preparation of Y-Ba-Cu oxide superconductor thin films using pulsed laser evaporation from high T_c bulk material. *Applied Physics Letters* 51, 619 (1987).

- [12] J. Kwo, T. C. Hsieh, R. M. Fleming, M. Hong, S. H. Liou, B. A. Davidson and L. C. Feldman: Structural and superconducting properties of orientation-ordered $Y_1Ba_2Cu_3O_{7-x}$ films prepared by molecular-beam epitaxy. *Physical Review B* 36, 4039 (1987).
- [13] N. Missert, R. Hammond, J. E. Mooij, V. Matijasevic, P. Rosenthal, T. H. Geballe, A. Kapitulnik, M. R. Beasley, S. S. Laderman, C. Lu, E. Garwin and R. Barton: In situ growth of superconducting YBaCuO using reactive electron-beam coevaporation. *Magnetics, IEEE Transactions on* 25, 2418 (1989).
- [14] D. M. Lind, S. D. Berry, G. Chern, H. Mathias and L. R. Testardi, Characterization of the structural and magnetic ordering of Fe_3O_4/NiO superlattices grown by oxygen-plasma-assisted molecular-beam epitaxy, in: *The 5th Joint MMMIntermag Conference*, vol 70, AIP, Pittsburgh, Pennsylvania (USA), 1991, pp. 6218.
- [15] M. E. Lin, B. N. Sverdlov, S. Strite, H. Morkov and A. E. Drakin: Refractive indices of wurtzite and zinblende GaN. *Electronics Letters* 29, 1759 (1993).
- [16] Y. Chen, D. M. Bagnall, Z. Zhu, T. Sekiechi, K. Park, K. Hiraga, T. Yao, S. Koyama, M. Y. Shen and T. Goto: Growth of ZnO single crystal thin films on c-plane (0001) sapphire by plasma enhanced molecular beam epitaxy. *Journal of Crystal Growth* 181, 165 (1997).
- [17] S. K. Hong, H. J. Ko, Y. Chen, T. Hanada and T. Yao, ZnO/GaN heterointerfaces and ZnO films grown by plasma-assisted molecular beam epitaxy on (0001) GaN/ Al_2O_3 , in: vol 18, *AVS*, 2000, pp. 2313.
- [18] S. K. Hong, H. J. Ko, Y. Chen, T. Hanada and T. Yao: ZnO/GaN heterointerfaces and ZnO films grown by plasma-assisted molecular beam epitaxy on (0001) GaN/ Al_2O_3 . *Journal of Vacuum Science and Technology B* 18, 2313 (2000).
- [19] Y. Chen, N. T. Tuan, Y. Segawa, H.-j. Ko, S.-k. Hong and T. Yao: Stimulated emission and optical gain in ZnO epilayers grown by plasma-assisted molecular-beam epitaxy with buffers. *Applied Physics Letters* 78, 1469 (2001).
- [20] A. Nakamura, J. Ishihara, S. Shigemori, K. Yamamoto, T. Aoki, H. Gotoh and J. Temmyo: Characterization of wurtzite $Zn_{1-x}Cd_xO$ films using remote plasma-enhanced metalorganic chemical vapor deposition. *Japanese Journal of Applied Physics Part 2-Letters & Express Letters* 43, L1452 (2004).

- [21] S. Shigemori, A. Nakamura, J. Ishihara, T. Aoki and J. Temmyo: Zn_{1-x}Cd_xO film growth using remote plasma-enhanced metalorganic chemical vapor deposition. *Japanese Journal of Applied Physics Part 2-Letters & Express Letters* 43, L1088 (2004).
- [22] J. Dong, A. Osinsky, B. Hertog, A. Dabiran, P. Chow, Y. Heo, D. Norton and S. Pearton: Development of MgZnO-ZnO-AlGaIn heterostructures for ultraviolet light emitting applications. *Journal of Electronic Materials* 34, 416 (2005).
- [23] J. Hopwood: Review of inductively coupled plasmas for plasma processing. *Plasma Sources Sci. Technol.* 1, 109 (1992).
- [24] U. Cvelbar, M. Mozetic and A. Ricard: Characterization of oxygen plasma with a fiber optic catalytic probe and determination of recombination coefficients. *Plasma Science, IEEE Transactions on* 33, 834 (2005).
- [25] A. Vesel, M. Mozetic and M. Balat-Pichelin: Oxygen atom density in microwave oxygen plasma. *Vacuum* 81, 1088 (2007).
- [26] X. W. Sun and H. S. Kwok: Optical properties of epitaxially grown zinc oxide films on sapphire by pulsed laser deposition. *Journal of Applied Physics* 86, 408 (1999).
- [27] T. Makino, Y. Segawa, M. Kawasaki, A. Ohtomo, R. Shiroki, K. Tamura, T. Yasuda and H. Koinuma: Band gap engineering based on Mg_xZn_{1-x}O and Cd_yZn_{1-y}O ternary alloy films. *Applied Physics Letters* 78, 1237 (2001).
- [28] Y. Kakehi, S. Nakao, K. Satoh and T. Kusaka: Room-temperature epitaxial growth of NiO(1 1 1) thin films by pulsed laser deposition. *Journal of Crystal Growth* 237-239, 591 (2002).
- [29] H. Ohta, M. Hirano, K. Nakahara, H. Maruta, T. Tanabe, M. Kamiya, T. Kamiya and H. Hosono: Fabrication and photoresponse of a pn-heterojunction diode composed of transparent oxide semiconductors, p-NiO and n-ZnO. *Applied Physics Letters* 83, 1029 (2003).
- [30] R. Schmidt, B. Rheinlander, M. Schubert, D. Spemann, T. Butz, J. Lenzner, E. M. Kaidashev, M. Lorenz, A. Rahm, H. C. Semmelhack and M. Grundmann: Dielectric functions (1 to 5 eV) of wurtzite Mg_xZn_{1-x}O ($x \leq 0.29$) thin films. *Applied Physics Letters* 82, 2260 (2003).

- [31] D. Franta, B. Negulescu, L. Thomas, P. R. Dahoo, M. Guyot, I. Ohlídal, J. Mistrík and T. Yamaguchi: Optical properties of NiO thin films prepared by pulsed laser deposition technique. *Applied Surface Science* 244, 426 (2005).
- [32] C. Bundesmann, A. Rahm, M. Lorenz, M. Grundmann and M. Schubert: Infrared optical properties of $\text{Mg}_x\text{Zn}_{1-x}\text{O}$ thin films ($0 \leq x \leq 1$): Long-wavelength optical phonons and dielectric constants. *Journal of Applied Physics* 99, 113504 (2006).
- [33] K. Oka, T. Yanagida, K. Nagashima, H. Tanaka and T. Kawai: Growth atmosphere dependence of transport properties of NiO epitaxial thin films. *Journal of Applied Physics* 104, 013711 (2008).
- [34] A. Y. Polyakov, N. B. Smirnov, A. V. Govorkov, E. A. Kozhukhova, A. I. Belogorokhov, H. S. Kim, D. P. Norton and S. J. Pearton: Annealing effects on electrical properties of MgZnO films grown by pulsed laser deposition. *Journal of Applied Physics* 103, 083704 (2008).
- [35] B. A. Everitt, D. Wang and J. M. Daughton, Spin valves with NiO pinning layer, in: *Ieee-Inst Electrical Electronics Engineers Inc*, 1996, pp. 4657.
- [36] Y. Hamakawa, H. Hoshiya, T. Kawabe, Y. Suzuki, R. Arai, K. Nakamoto, M. Fuyama and Y. Sugita: Spin-valve heads utilizing antiferromagnetic NiO layers. *Magnetics, IEEE Transactions on* 32, 149 (1996).
- [37] M. D. Stiles and R. D. McMichael: Model for exchange bias in polycrystalline ferromagnet-antiferromagnet bilayers. *Physical Review B* 59, 3722 (1999).
- [38] D.-W. Kim, B. H. Park, R. Jung and S. Seo: Reversible Resistance Switching Behaviors of Pt/NiO/Pt Structures. *Japanese Journal of Applied Physics* 46, 5205
- [39] S. Seo, M. J. Lee, D. H. Seo, E. J. Jeoung, D. S. Suh, Y. S. Joung, I. K. Yoo, I. R. Hwang, S. H. Kim, I. S. Byun, J. S. Kim, J. S. Choi and B. H. Park: Reproducible resistance switching in polycrystalline NiO films. *Applied Physics Letters* 85, 5655 (2004).
- [40] D. C. Kim, S. Seo, S. E. Ahn, D. S. Suh, M. J. Lee, B. H. Park, I. K. Yoo, I. G. Baek, H. J. Kim, E. K. Yim, J. E. Lee, S. O. Park, H. S. Kim, U. I. Chung, J. T. Moon and B. I. Ryu: Electrical observations of filamentary conduction for the resistive memory switching in NiO films. *Applied Physics Letters* 88, 202102 (2006).

- [41] Y.-H. You, B.-S. So, J.-H. Hwang, W. Cho, S. S. Lee, T.-M. Chung, C. G. Kim and K.-S. An: Impedance spectroscopy characterization of resistance switching NiO thin films prepared through atomic layer deposition. *Applied Physics Letters* 89, 222105 (2006).
- [42] S. K. S. S. M.-J. L. D.-C. K. S.-E. A. Y. P. J. K. H. S. Jung-Bin Yun: Random and localized resistive switching observation in Pt/NiO/Pt. *physica status solidi (RRL) - Rapid Research Letters* 1, 280 (2007).
- [43] M. D. Lee, C. H. Ho, C. K. Lo, T. Y. Peng and Y. D. Yao: Effect of Oxygen Concentration on Characteristics of NiO_x-Based Resistance Random Access Memory. *Magnetics, IEEE Transactions on* 43, 939 (2007).
- [44] L. Courtade, C. Turquat, C. Muller, J. G. Lisoni, L. Goux, D. J. Wouters, D. Goguenheim, P. Roussel and L. Ortega: Oxidation kinetics of Ni metallic films: Formation of NiO-based resistive switching structures. *Thin Solid Films* 516, 4083 (2008).
- [45] R. J. Powell and W. E. Spicer: Optical Properties of NiO and CoO. *Physical Review B* 2, 2182 (1970).
- [46] A. Fujimori and F. Minami: Valence-band photoemission and optical absorption in nickel compounds. *Physical Review B* 30, 957 (1984).
- [47] G. J. M. Janssen and W. C. Nieuwpoort: Band gap in NiO: A cluster study. *Physical Review B* 38, 3449 (1988).
- [48] M. Atanasov and D. Reinen: Non-local electronic effects in core-level photoemission, UV and optical electronic absorption spectra of nickel oxides. *Journal of Electron Spectroscopy and Related Phenomena* 86, 185 (1997).
- [49] S. L. Dudarev, G. A. Botton, S. Y. Savrasov, C. J. Humphreys and A. P. Sutton: Electron-energy-loss spectra and the structural stability of nickel oxide: An LSDA+U study. *Physical Review B* 57, 1505 (1998).
- [50] O. Bengone, M. Alouani, J. Hugel and P. Blochl: LDA+U calculated electronic and structural properties of NiO(001) and NiO(111) p(2x2) surfaces. *Computational Materials Science* 24, 192 (2002).

- [51] H. Kamal, E. K. Elmaghraby, S. A. Ali and K. Abdel-Hady: Characterization of nickel oxide films deposited at different substrate temperatures using spray pyrolysis. *Journal of Crystal Growth* 262, 424 (2004).
- [52] P. Luches, E. Groppo, S. D'Addato, C. Lamberti, C. Prestipino, S. Valeri and F. Boscherini: NiO and MgO ultrathin films by polarization dependent XAS. *Surface Science* 566-568, 84 (2004).
- [53] A. M. Ferrari, C. Pisani, F. Cinquini, L. Giordano and G. Pacchioni: Cationic and anionic vacancies on the NiO(100) surface: DFT + U and hybrid functional density functional theory calculations. *The Journal of Chemical Physics* 127, 174711 (2007).
- [54] W. Zhang, N. Yu, W. Yu and B. Tang: Stability and magnetism of vacancy in NiO: A GGA+U study. *The European Physical Journal B - Condensed Matter and Complex Systems* 64, 153 (2008).
- [55] N. F. Mott: The Basis of the Electron Theory of Metals, with Special Reference to the Transition Metals. *Proceedings of the Physical Society. Section A* 62, 416 (1949).
- [56] J. Zaanen, G. A. Sawatzky and J. W. Allen: Band gaps and electronic structure of transition-metal compounds. *Physical Review Letters* 55, 418 (1985).
- [57] G. Wakefield, P. J. Dobson, Y. Y. Foo, A. Loni, A. Simons and J. L. Hutchison: The fabrication and characterization of nickel oxide films and their application as contacts to polymer/porous silicon electroluminescent devices. *Semiconductor Science and Technology* 12, 1304 (1997).
- [58] Y. Ohya, H. Koyama, T. Ban and Y. Takahashi: Electrical properties of p-n contact with oxide semiconductor thin films fabricated by liquid phase method. *Materials Science and Engineering: B* 54, 55 (1998).
- [59] J.-M. Choi and S. Im: Ultraviolet enhanced Si-photodetector using p-NiO films. *Applied Surface Science* 244, 435 (2005).
- [60] Y. Vygranenko, K. Wang and A. Nathan: Low leakage p-NiO/i-ZnO/n-ITO heterostructure ultraviolet sensor. *Applied Physics Letters* 89, 172105 (2006).

- [61] S. Lany, J. Osorio-Guillen and A. Zunger: Origins of the doping asymmetry in oxides: Hole doping in NiO versus electron doping in ZnO. *Physical Review B (Condensed Matter and Materials Physics)* 75, 241203 (2007).
- [62] X. Chen, K. Ruan, G. Wu and D. Bao: Tuning electrical properties of transparent p-NiO/n-MgZnO heterojunctions with band gap engineering of MgZnO. *Applied Physics Letters* 93, 112112 (2008).
- [63] K. Kobayashi, M. Yamaguchi, Y. Tomita and Y. Maeda: Fabrication and characterization of In-Ga-Zn-O/NiO structures. *Thin Solid Films* 516, 5903 (2008).
- [64] Y. S. Park, C. W. Litton, T. C. Collins and D. C. Reynolds: Exciton Spectrum of ZnO. *Physical Review* 143, 512 (1966).
- [65] D. C. Reynolds and T. C. Collins: Excited Terminal States of a Bound Exciton-Donor Complex in ZnO. *Physical Review* 185, 1099 (1969).
- [66] U. Ozgur, Y. I. Alivov, C. Liu, A. Teke, M. A. Reshchikov, S. Dogan, V. Avrutin, S. J. Cho and H. Morkoc: A comprehensive review of ZnO materials and devices. *Journal of Applied Physics* 98, 1 (2005).
- [67] H. D. Li, S. F. Yu, S. P. Lau, E. S. P. Leong, H. Y. Yang, T. P. Chen, A. P. Abiyasa and C. Y. Ng: High-Temperature Lasing Characteristics of ZnO Epilayers. *Advanced Materials* 18, 771 (2006).
- [68] K. Ellmer and G. Vollweiler: Electrical transport parameters of heavily-doped zinc oxide and zinc magnesium oxide single and multilayer films heteroepitaxially grown on oxide single crystals. *Thin Solid Films* 496, 104 (2006).
- [69] D. C. Look: Recent advances in ZnO materials and devices. *Materials Science and Engineering: B* 80, 383 (2001).
- [70] N. Izyumskaya, V. Avrutin, U. Ozgur, Y. I. Alivov and H. Morkoc: Preparation and properties of ZnO and Devices. *physica status solidi (b)* 244, 1439 (2007).
- [71] T. Shiosaki and A. Kawabata: Low-frequency piezoelectric-transducer applications of ZnO film. *Applied Physics Letters* 25, 10 (1974).
- [72] H. Sasaki, K. Tsubouchi, N. Chubachi and N. Mikoshiba: Photoelastic effect in piezoelectric semiconductor - ZnO. *Journal of Applied Physics* 47, 2046 (1976).

- [73] G. Carlotti, G. Socino and E. Verona, Photoelastic characterization of ZnO films, in: IEEE Ultrasonics Symposium, vol 1, Chicago, IL, 1988, pp. 427.
- [74] D. C. Look, D. C. Reynolds, J. R. Sizelove, R. L. Jones, C. W. Litton, G. Cantwell and W. C. Harsch: Electrical properties of bulk ZnO. Solid State Communications 105, 399 (1998).
- [75] C. W. Teng, J. F. Muth, U. Ozgur, M. J. Bergmann, H. O. Everitt, A. K. Sharma, C. Jin and J. Narayan: Refractive indices and absorption coefficients of $Mg_xZn_{1-x}O$ alloys. Applied Physics Letters 76, 979 (2000).
- [76] S. Choopun, R. D. Vispute, W. Yang, R. P. Sharma, T. Venkatesan and H. Shen: Realization of band gap above 5.0 eV in metastable cubic-phase $Mg_xZn_{1-x}O$ alloy films. Appl. Phys. Lett. 80, 1529 (2002).
- [77] N. B. Chen, H. Z. Wu and T. N. Xu: Refractive indices of cubic-phase $Mg_xZn_{1-x}O$ thin-film alloys. Journal of Applied Physics 97, 023515 (2005).
- [78] R. Schmidt-Grund, A. Carstens, B. Rheinlander, D. Spemann, H. Hochmut, G. Zimmermann, M. Lorenz, M. Grundmann, C. M. Herzinger and M. Schubert: Refractive indices and band-gap properties of rocksalt $Mg_xZn_{1-x}O$ ($0.68 < x < 1$). Journal of Applied Physics 99, 123701 (2006).
- [79] S. M. Lee, D. G. Cahill and T. H. Allen: Thermal conductivity of sputtered oxide films. Physical Review B 52, 253 (1995).
- [80] A. J. Slifka, B. J. Filla and J. M. Phelps: Thermal conductivity of magnesium oxide from absolute, steady-state measurements. J. Res. Natl. Inst. Stand. and Technol. 103, 357 (1998).
- [81] Q. Guo, C. Xu and D. W. Goodman: Ultrathin Films of NiO on MgO(100): Studies of the Oxide-Oxide Interface. Langmuir 14, 1371 (1998).
- [82] M. A. James and T. Hibma: Thickness-dependent relaxation of NiO(001) overlayers on MgO(001) studied by X-ray diffraction. Surface Science 433-435, 718 (1999).
- [83] J. Ropcke, T. Zimdahl, D. Schlott and H. Glaefeke: Initiation of Gas-Discharges in Plasma Displays Assisted by Electron-Emission of Thin Insulators. Contributions to Plasma Physics 30, 679 (1990).

- [84] K. Yoshida, H. Uchiike and M. Sawa: Fundamental characteristics of MgO film and their influence on the operation of plasma displays. *IEEE Transactions on Electronics E82C*, 1798 (1999).
- [85] Y. W. Choi and J. Kim: Reactive sputtering of magnesium oxide thin film for plasma display panel applications. *Thin Solid Films* 460, 295 (2004).
- [86] H. W. Choi, Y. J. Kim and S. J. Kwon: Dependence of the material properties and PDP discharging characteristics on the MgO evaporation rate. *Journal of the Korean Physical Society* 49, 1465 (2006).
- [87] A. Kuzmin and N. Mironova: Composition dependence of the lattice parameter in $\text{Ni}_c\text{Mg}_{1-c}\text{O}$ solid solutions. *Journal of Physics: Condensed Matter* 10, 7937 (1998).
- [88] A. M. Salem, M. Mokhtar and G. A. El-Shobaky: Electrical properties of pure and Li₂O-doped NiO/MgO system. *Solid State Ionics* 170, 33 (2004).
- [89] Z. G. Ji, Z. P. He, K. Liu, S. C. Zhao and Z. J. He: Synthesis of $\text{Mg}_x\text{Ni}_{1-x}\text{O}$ thin films with a band-gap in the solar-blind region. *Journal of Crystal Growth* 273, 446 (2005).
- [90] C. E. Rossi and W. Paul: The preparation of NiO thin films and their use in optical measurements in the visible and ultraviolet. *Journal of Physics and Chemistry of Solids* 30, 2295 (1969).
- [91] B. Lalevic, B. Leung and Fuschill.N: Transport and optical properties of NiO and NiO(Li) thin-films. *Bulletin of the American Physical Society* 17, 246 (1972).
- [92] D. M. Lind, S. D. Berry, G. Chern, H. Mathias and L. R. Testardi: Growth and structural characterization of Fe_3O_4 and NiO thin-films and superlattices grown by oxygen-plasma-assisted molecular beam epitaxy. *Physical Review B* 45, 1838 (1992).
- [93] Z. Feng, V. S. Babu, J. Zhao and M. S. Seehra, Effect of magnetic dilution on magnetic ordering in $\text{Ni}_p\text{Mg}_{1-p}\text{O}$, in: *The 5th Joint MMMIntermag Conference*, vol 70, AIP, Pittsburgh, Pennsylvania (USA), 1991, pp. 6161.
- [94] A. Kuzmin, N. Mironova, J. Purans and A. Rodionov: X-ray absorption spectroscopy study of $\text{Ni}_c\text{Mg}_{1-c}\text{O}$ solid solutions on the Ni K edge. *Journal of Physics: Condensed Matter* 7, 9357 (1995).

- [95] J. S. Choi, H. Y. Lee and K. H. Kim: Electrical conductivity of nickel oxide-magnesium oxide single crystals. *The Journal of Physical Chemistry* 77, 2430 (1973).
- [96] T. Gruber, C. Kirchner, R. Kling, F. Reuss and A. Waag: ZnMgO epilayers and ZnO--ZnMgO quantum wells for optoelectronic applications in the blue and UV spectral region. *Applied Physics Letters* 84, 5359 (2004).
- [97] R. Schmidt-Grund, M. Schubert, B. Rheinländer, D. Fritsch, H. Schmidt, E. M. Kaidashev, M. Lorenz, C. M. Herzinger and M. Grundmann: UV-VUV spectroscopic ellipsometry of ternary $\text{Mg}_x\text{Zn}_{1-x}\text{O}$ ($0 \leq x \leq 0.53$) thin films. *Thin Solid Films* 455-456, 500 (2004).
- [98] K. Koike, K. Hama, I. Nakashima, S. Sasa, M. Inoue and M. Yano: Molecular beam epitaxial growth of Al-doped ZnMgO alloy films for modulation-doped ZnO/ZnMgO heterostructures. *Japanese Journal of Applied Physics Part 1-Regular Papers Short Notes & Review Papers* 44, 3822 (2005).
- [99] N. B. Chen and C. H. Sui: Recent progress in research on $\text{Mg}_x\text{Zn}_{1-x}\text{O}$ alloys. *Materials Science and Engineering: B* 126, 16 (2006).
- [100] P. Yu, H. Wu, N. Chen, T. Xu, Y. Lao and J. Liang: Cubic $\text{Mg}_x\text{Zn}_{1-x}\text{O}$ films grown on SiO_2 substrates. *Optical Materials* 28, 271 (2006).
- [101] S. K. Hong, Y. Chen, H. J. Ko, H. Wenisch, T. Hanada and T. Yao: ZnO and Related Materials: Plasma-Assisted Molecular Beam Epitaxial Growth, Characterization, and Application. *Journal of Electronic Materials* 30, 647 (2001).
- [102] K. W. Liu, J. Y. Zhang, J. G. Ma, D. Y. Jiang, Y. M. Lu, B. Yao, B. H. Li, D. X. Zhao, Z. Z. Zhang and D. Z. Shen: $\text{Zn}_{0.8}\text{Mg}_{0.2}\text{O}$ -based metal-semiconductor-metal photodiodes on quartz for visible-blind ultraviolet detection. *Journal of Physics D: Applied Physics* 40, 2765 (2007).
- [103] J. Kobayashi, H. Sekiwa, M. Miyamoto, N. Ohashi, I. Sakaguchi, Y. Wada, Y. Adachi and H. Haneda: Growth of Thick Zinc Magnesium Oxide by Liquid Phase Epitaxy. *Applied Physics Express* 1, 071201 (2008).
- [104] J. C. Phillips: Ionicity of chemical bond in crystals. *Rev. Mod. Phys.* 42, 317 (1970).
- [105] Y. Chen, J. L. Kolopus and W. A. Sibley: Luminescence of the F^+ Center in MgO . *Physical Review* 186, 865 (1969).

- [106] G. P. Summers, T. M. Wilson, B. T. Jeffries, H. T. Tohver, Y. Chen and M. M. Abraham: Luminescence from oxygen vacancies in MgO crystals thermochemically reduced at high temperatures. *Phys. Rev. B: Condens. Matter* 27, 1283 (1983).
- [107] J. Narayan, A. K. Sharma, A. Kvit, C. Jin, J. F. Muth and O. W. Holland: Novel cubic $Zn_xMg_{1-x}O$ epitaxial heterostructures on Si(100) substrates. *Solid State Commun.* 121, 9 (2002).
- [108] Z. Vashaei, T. Minegishi, H. Suzuki, T. Hanada, M. W. Cho and T. Yao: Structural variation of cubic and hexagonal $Mg_xZn_{1-x}O$ layers grown on MgO(111)/c-sapphire. *J. Appl. Phys.* 2005, 054911 (2005).
- [109] S. S. Hullavarad, N. V. Hullavarad, D. E. Pugel, S. Dhar, I. Takeuchi, T. Venkatesan and R. D. Vispute: Homo- and hetero-epitaxial growth of hexagonal and cubic $Mg_xZn_{1-x}O$ alloy thin films by pulsed laser deposition technique. *J. Phys. D: Appl. Phys.* 40, 4887 (2007).
- [110] X. Chen and J. Kang: The structural properties of wurtzite and rocksalt $Mg_xZn_{1-x}O$. *Semicond. Sci. Technol.* 23, 025008 (2008).
- [111] J. M. Qin, B. Yao, X. P. Jia, C. X. Shan, J. Y. Zhang, H. A. Ma and D. Z. Shen: Characterizations of single-phased cubic $Mg_{0.5}Zn_{0.5}O$ prepared at high pressure and high temperature. *J. Phys. D: Appl. Phys.* 41, 155408 (2008).
- [112] A. Gibson, R. Haydock and J. P. LaFemina: Stability vacancy defects in MgO: the role of charge neutrality. *Physical Review B* 50, 2582 (1994).
- [113] E. A. Kotomin and A. I. Popov: Radiation-induced point defects in simple oxides. *Nuclear Instruments and Methods in Physics Research* 141, 1 (1998).
- [114] J. Chen, W. Z. Shen, N. B. Chen, D. J. Qiu and H. Z. Wu: The study of composition non-uniformity in ternary $Mg_xZn_{1-x}O$ thin films. *J. Phys. Condens. Matter* 15, L475 (2003).
- [115] J.-J. Chen, F. Ren, D. P. Norton, S. J. Pearton, A. Osinsky, J. W. Dong and S. N. G. Chu: Diffusion-controlled selective wet etching of ZnCdO over ZnO. *Electrochemical and Solid-State Letters* 8, G359 (2005).
- [116] A. Osinsky, J. Dong, J. Q. Xie, B. Hertog, A. Dabiran, P. P. Chow, S. J. Pearton, D. P. Norton, D. C. Look, W. V. Schoenfeld, O. Lopatiuk, L. Chernyak, M. Cheung, A. N.

- Cartwright and M. Gerhold: ZnCdO/ZnMgO and ZnO/AlGaN heterostructures for UV and visible light emitters. *Materials Research Society Symposium Proceeding 892*, (2006).
- [117] X. J. Wang, I. A. Buyanova, W. M. Chen, M. Izadifard, S. Rawal, D. P. Norton, S. J. Pearton, A. Osinsky, J. W. Dong and A. Dabiran: Band gap properties of Zn_{1-x}Cd_xO alloys grown by molecular-beam epitaxy. *Applied Physics Letters* 89, 151909 (2006).
- [118] I. A. Buyanova, J. P. Bergman, G. Pozina, W. M. Chen, S. Rawal, D. P. Norton, S. J. Pearton, A. Osinsky and J. W. Dong: Mechanism for radiative recombination in ZnCdO alloys. *Applied Physics Letters* 90, 261907 (2007).
- [119] J. W. Mares, F. R. Ruhge, A. V. Thompson, P. G. Kik, A. Osinsky, B. Hertog, A. M. Dabiran, P. P. Chow and W. V. Schoenfeld: Optical and morphological properties of MBE grown wurtzite Cd_xZn_{1-x}O thin films. *Optical Materials* 30, 346 (2007).
- [120] J. W. Mares, M. Falanga, W. R. Folks, G. Boreman, A. Osinsky, B. Hertog, J. Q. Xie and W. V. Schoenfeld: Complex refractive indices of Cd_xZn_{1-x}O thin films grown by molecular beam epitaxy. submitted to the *Journal of Electronic Materials*, under review (2008).
- [121] J. W. Mares, M. Falanga, A. V. Thompson, A. Osinsky, J. Q. Xie, B. Hertog, A. Dabiran, P. Chow and W. V. Schoenfeld: Hybrid CdZnO/GaN quantum well light emitting diodes. *Journal of Applied Physics* 104, 093107 (2008).
- [122] A. B. Djurisić: Elite genetic algorithms with adaptive mutations for solving continuous optimization problems - application to modeling of the optical constants of solids. *Optics Communications* 151, 147 (1998).
- [123] S. Jurecka, M. Jurechova and J. Mullerova: Genetic algorithm approach to thin film optical parameter determination. *Acta Physica Slovaca* 53, 215 (2003).
- [124] A. R. Forouhi and I. Bloomer: Optical dispersion relations for amorphous semiconductors and amorphous dielectrics. *Physical Review B* 34, 7018 (1986).
- [125] A. R. Forouhi and I. Bloomer: Optical properties of crystalline semiconductors and dielectrics. *Physical Review B* 38, 1865 (1988).
- [126] D. Poelman and P. F. Smet: Methods for the determination of the optical constants of thin films from single transmission measurements: a critical review. *Journal of Physics D: Applied Physics* 36, 1850 (2003).

